INVESTIGATION OF DELAMINATION SUPPRESSION IN HIGHLY TAPERED COMPOSITE LAMINATES

A THESIS SUBMITTED TO
THE GRADUATE SCHOOL OF NATURAL AND APPLIED SCIENCES
OF
MIDDLE EAST TECHNICAL UNIVERSITY

BY

FIRAT ERGİN

IN PARTIAL FULFILLMENT OF THE REQUIREMENTS
FOR
THE DEGREE OF MASTER OF SCIENCE
IN
AEROSPACE ENGINEERING

DECEMBER 2023

Approval of the thesis:

INVESTIGATION OF DELAMINATION SUPPRESSION IN HIGHLY TAPERED COMPOSITE LAMINATES

submitted by **FIRAT ERGİN** in partial fulfillment of the requirements for the degree of **Master of Science** i**n Aerospace Engineering, Middle East Technical University** by,

Prof. Dr. Halil Kalıpçılar
Dean, Graduate School of **Natural and Applied Sciences** _____

Prof. Dr. Serkan Özgen
Head of the Department, **Aerospace Engineering** _____

Prof. Dr. Altan Kayran
Supervisor, **Aerospace Engineering, METU** _____

Examining Committee Members:

Prof. Dr. Demirkan Çöker
Aerospace Engineering, METU _____

Prof. Dr. Altan Kayran
Aerospace Engineering, METU _____

Assoc. Prof. Dr. Ercan Gürses
Aerospace Engineering, METU _____

Assoc. Prof. Dr. Barış Sabuncuoğlu
Mechanical Engineering, Hacettepe University _____

Assist. Prof. Dr. Görkem Eğemen Güloğlu
Aerospace Engineering, METU _____

Date: 07.12.2023

I hereby declare that all information in this document has been obtained and presented in accordance with academic rules and ethical conduct. I also declare that, as required by these rules and conduct, I have fully cited and referenced all material and results that are not original to this work.

Name, Surname : Fırat Ergin

Signature :

ABSTRACT

INVESTIGATION OF DELAMINATION SUPPRESSION IN HIGHLY TAPERED COMPOSITE LAMINATES

Ergin, Fırat
Master of Science, Aerospace Engineering
Supervisor : Prof. Dr. Altan Kayran

December 2023,118 pages

The presence of ply termination locations makes tapered composite laminates susceptible to delamination, thereby reducing the overall structural performance. The primary objective of this study is to propose a novel design alternative for highly tapered laminates with the aim of suppressing delamination onset. In situ experiments on dropped ply specimens are conducted to identify the failure mechanisms within ply drop-off regions. Different delamination modes and their dynamic progression in dropped ply specimens are effectively captured through experimental procedures. Material characterization tests for a Glass Fiber Reinforced Polymer (GFRP) and epoxy resin system are conducted to obtain the mechanical properties essential for the development of finite element models. Cohesive zone modeling technique is employed in FE models to predict delamination. Effects of through-thickness compression enhancement of shear properties and modeling details around the resin pocket are also investigated numerically. The finite element models for single-stage ply drop-off region effectively replicated the delamination onset loads and locations observed in the experimental studies. A parametric taper angle study on a single-stage ply drop-off region revealed that an increase in the taper angle significantly decreases the delamination onset load at the beginning of the thin section of the tapered laminate. Building on this finding, the study introduces

the variable taper angle design concept. This design aims to delay the thin section delamination in highly tapered laminates by providing a gradual transition in the taper region. The finite element results of the proposed design concept demonstrated that a substantial improvement of nearly 80% on delamination onset load can be achieved through the proper selection of the taper geometry.

Keywords: Tapered Laminates, Delamination Suppression, Cohesive Zone Method, Finite Element Method

ÖZ

YÜKSEK KONIK KOMPOZİT YAPILARDA KATMAN AYRILMASI ENGELLENMESİNİN İNCELENMESİ

Ergin, Fırat
Yüksek Lisans, Havacılık ve Uzay Mühendisliği
Tez Yöneticisi: Prof. Dr. Altan Kayran

Aralık 2023, 118 sayfa

Katman sonlandırma konumlarının varlığı, konik kompozit laminatları katman ayrılması hasarına duyarlı hale getirir ve böylece genel yapısal performansı azaltır. Bu çalışmanın temel amacı, katman ayrılmasının başlangıcını bastırmak amacıyla yüksek derecede konik laminatlar için yeni bir tasarım alternatifi önermektir. Katman azaltma bölgelerindeki hasar mekanizmalarını tanımlamak için katman azaltma numuneleri üzerinde deneysel incelemeler gerçekleştirildi. Farklı hasar modları ve bunların katman azaltılmış numunelerdeki dinamik ilerlemesi, deneysel prosedürler aracılığıyla etkili bir şekilde yakalandı. Sonlu eleman modellerinin geliştirilmesi için gerekli mekanik özellikleri elde etmek amacıyla bir cam elyaf takviyeli polimer (GFRP) malzeme ve epoksi reçine sistemi için malzeme karakterizasyon testleri yapıldı. Sonlu elemanlar modellerinde katman ayrılmasını tahmin etmek için kohesiv bölge modelleme (CZM) tekniği kullanıldı. Kalınlık boyunca sıkıştırmanın kayma özelliklerini arttırma etkileri ve reçine cebi etrafındaki modelleme detayları da sayısal olarak incelendi. Tek aşamalı katman azaltma bölgesi için sonlu eleman modelleri, deneysel çalışmalarda gözlemlenen katman ayrılması başlangıç yüklerini ve konumlarını etkili bir şekilde tahmin edebildi. Tek kademeli katman düşürme bölgesi üzerinde yapılan parametrik konik açısı çalışması, konik açısındaki artışın konik laminatın ince bölümünün başlangıcında meydana gelen

katman ayrılması başlangıç yükünü önemli ölçüde azalttığını ortaya çıkardı. Bu bulguya dayanarak, çalışma değişken konik açılı tasarım konseptini tanıtmaktadır. Bu tasarım, konik bölgede kademeli bir geçiş sağlayarak yüksek derecede konik laminatlarda ince kesit katman ayrılmasını geciktirmeyi amaçlamaktadır. Önerilen tasarım konseptinin sonlu elemanlar sonuçları, konik geometrinin doğru seçilmesiyle katman ayrılması başlangıç yükünde yaklaşık %80'lik önemli bir iyileşmenin elde edilebileceğini göstermiştir.

Anahtar Kelimeler: Konik Laminatlar, Katman Ayrılması Engellenmesi, Kohesiv Bölge Yöntemi, Sonlu Elemanlar Yöntemi

To my family and friends,
who always encourage me
to strive the best version of myself

ACKNOWLEDGMENTS

I would like to express my profound gratitude to my advisor, Prof. Dr. Altan Kayran, for his guidance and endless support. He motivated me to pursue the direction that excited me the most, which has led me to consistently cherish my research. His contribution to this study and my academic career is invaluable.

I also would like to thank Prof. Dr. Demirkan Çöker for not only his valuable comments and contributions to my study but also for offering me such a peaceful working environment that I have not experienced a single day where I approached my work with anything less than wholehearted enthusiasm.

I would like to thank Assoc. Prof. Dr. Ercan Gürses, Assoc. Prof. Dr. Barış Sabuncuoğlu, and Assist. Prof. Dr. Görkem Eğemen Güloğlu for attending my thesis defense presentation and improving my work with their valuable comments. I would also like to thank Özgün Şener for his companionship and support during the numerous challenges encountered throughout this study.

I would like to thank my colleagues Ahmet Çevik, Ali Ata Adam, Onur Ali Batmaz, Serhat Onur Çakmak, Tutku Ilgın Özcan, and Umut Altuntaş for their friendships that made this challenging time delightful. I would like to especially thank Onur Ali for his friendship, precious support, and discussions regarding not only the milestones of this study but also those of my life.

Last but not least, I express my deepest gratitude to my family, Melda Ergin, Murat Ergin, and Didem Ergin for their endless love and support. They always advised me to have positive relationships with others and pursue my dreams, thereby facilitating my ability to lead a contented life and engage in meaningful work that I love.

TABLE OF CONTENTS

LIST OF TABLES

LIST OF FIGURES

LIST OF ABBREVIATIONS

ASTM	American Society for Testing and Materials
C.V.	Coefficient of variation
CZM	Cohesive Zone Method
DCB	Double Cantilever Beam
DIC	Digital Image Correlation
ENF	End Notched Flexure
FE	Finite Element
GFRP	Glass Fiber Reinforced Polymer
ILSS	Interlaminar Shear Strength
SENB	Single Edge Notched Bend
TTCE	Through-Thickness Compression Enhancement

LIST OF SYMBOLS

E_1, E_2, E_3	Modulus of elasticity in material axis
E_{resin}	Elastic modulus of resin
G_{12}, G_{13}, G_{23}	Shear modulus in material axis
$\nu_{12}, \nu_{13}, \nu_{23}$	Poisson's ratios
ν_{resin}	Poisson's ratio of resin
X_T	Tensile strength in fiber direction
Y_T	Tensile strength in transverse direction
S_{12}	In-plane shear strength
$\tau_n, \tau_s, \tau_{st}$	Traction in normal, first, and second shear directions, respectively
τ_n^0	Interlaminar normal strength
τ_s^0	Interlaminar strength in the first shear direction
τ_{st}^0	Interlaminar strength in the second shear direction
$(\tau_n^0)_{resin}$	Normal strength of resin
G_{Ic}	Mode I fracture toughness of laminate
G_{IIc}	Mode II fracture toughness of laminate
G_{IIIc}	Mode III fracture toughness of laminate
$(G_c)_{resin}$	Fracture toughness of resin
$\delta_n, \delta_s, \delta_{st}$	Separation in normal, first, and second shear directions, respectively
ϕ	Taper angle of a single-stage ply drop-off region
ϕ_G	Global taper angle of a multi-single stage ply drop-off region
$\Delta\phi$	Taper angle increment
$\mu\varepsilon$	Micro strain

CHAPTER 1

INTRODUCTION

Lightweight structures have always been a vital requirement in the aerospace industry, as excessive weight in a structure adversely affects fuel consumption and vehicle performance. Therefore, designers consistently aim to optimize structures to achieve the lowest possible structural weight while preserving component integrity. One approach to achieving this type of structure involves using varying material thicknesses within the component, thus avoiding the unnecessary use of excessive material in lightly loaded regions. However, it is important to note that locations, where material thickness is reduced, can be susceptible to early failure initiation in the structure due to stress concentrations resulting from abrupt cross-sectional changes. Consequently, it is crucial to design load-carrying structures with a smooth thickness variation.

Advanced machining techniques enable designers to manufacture parts with smooth thickness transitions in metallic materials. However, when dealing with laminated composite materials—manufactured by laying plies on top of each other—the achievement of thickness transition involves terminating appropriate plies. This termination process leads to abrupt material and geometrical discontinuities within the structure. A schematic depiction of an asymmetric single-ply termination location, also referred to as ply drop-off, is provided in Figure 1.1. Ply termination locations elevate the interlaminar stresses within the composite structure in localized areas. The combination of weak interlaminar bonding inherent in laminated composite materials with high interlaminar stresses due to ply terminations contributes to the early failure of the structure near ply drop-off regions in the form of delamination. That is why designing a thickness reduction in composite materials is a challenging problem.

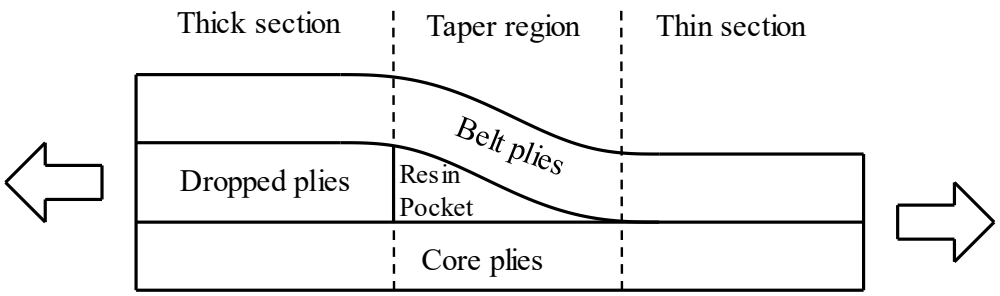

Figure 1.1. Schematic of a single-stage asymmetrical ply drop-off region.

To attain the desired thickness reduction in laminated composite materials, multiple consecutive ply terminations are performed, resulting in tapered laminates, which are illustrated in Figure 1.2(a). The purpose of the thickness reduction is not only to reduce the component weight but also to satisfy different stiffness requirements in composite structures depending on the loading conditions. For instance, scenarios wherein high stiffness requirement on one side and high flexibility requirement on the other side of the composite parts may necessitate many ply terminations in a short distance resulting in a laminate with a high taper angle. A notable example of such highly tapered composite laminates can be found in flex-beam of helicopter rotors [1]. An image of a highly tapered composite laminate investigated in Ref. [2] is shown in Figure 1.2(b).

This study centers around the failure mechanisms in ply drop-off regions and investigates the techniques to suppress delamination in highly tapered laminates. Therefore, it is important to understand the parameters affecting the delamination onset in such tapered laminates. Hence, the studies in the literature investigating the failure mechanism in tapered laminates and the effect of different parameters on delamination characteristics are summarized in the following section.

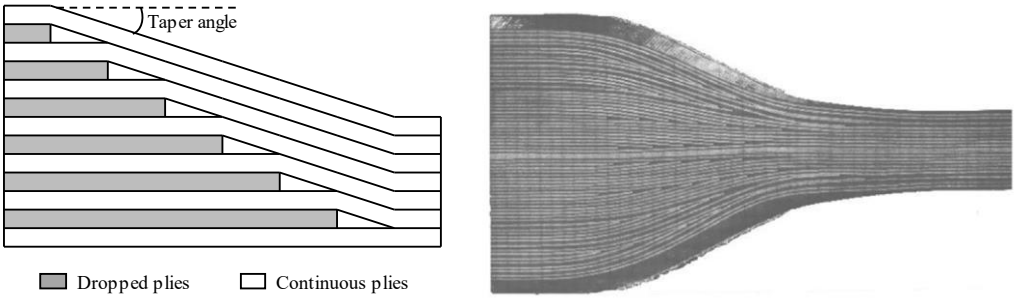

(a) (b)

Figure 1.2. (a) An illustration of a tapered laminate and (b) a cross-section of a highly tapered laminate investigated in Ref. [2].

1.1 Failure Mechanisms in Ply Drop-Off Regions

Designing an efficient tapered structure requires one to comprehensively grasp the failure modes and parameters triggering the damage initiation in ply drop-off regions. Therefore, three fracture modes are shown in Figure 1.3. Mode I fracture is the opening of the crack surface while Mode II and Mode III arise due to shearing of the crack surfaces. The primary factor contributing to delamination in ply termination locations is the interlaminar stress concentrations associated with the material and geometrical discontinuities observed in these regions. Depending on the stress state in the interface, different fracture modes or their combination might be observed. For example, pure opening and pure shear stresses result in Mode I and Mode II fracture modes, respectively, but if the opening and shear stresses coexist within the interface, Mode I and Mode II failures are observed concurrently called mixed mode failure. The combination of shear and compression stresses on the fracture surface is also considered pure Mode II failure because the opening of the crack tip is prevented due to the presence of compressive stresses and only shear stresses drive the failure.

It is important to know the interlaminar stresses around a ply drop-off region to gain insight into the failure mechanics in tapered composite structures. Figure 1.4 shows the distribution of interlaminar normal stresses and schematics of stress components

around a ply drop-off region under tensile loading. Dropped ply–covering ply and dropped ply–core ply interfaces in the thick section experience combined compression and shear stresses while covering ply–core ply interface in the thin section primarily encounters normal opening stresses. Furthermore, preliminary finite element analysis revealed the existence of interlaminar shear stresses at the beginning of the thin section of asymmetrically tapered specimens [3].

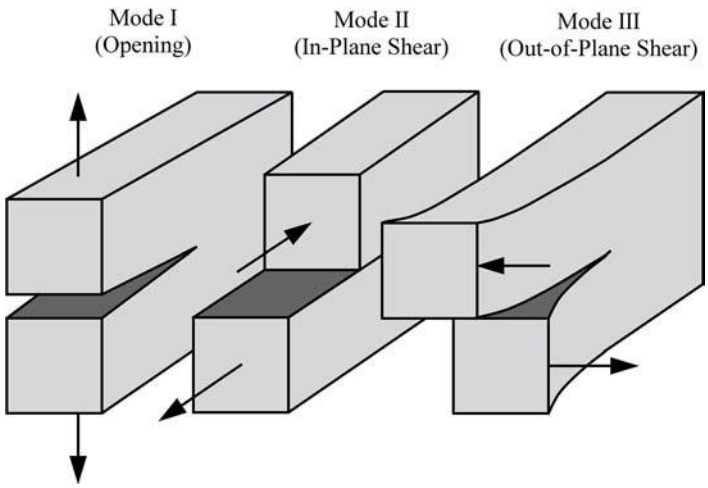

Figure 1.3. Fracture modes [4].

Depending on the configuration and geometry of the tapered laminate, two different delamination modes can be observed in these types of structures: thin-section delamination and thick-section delamination, as illustrated in Figure 1.5. In the thick section delamination, a pair of cracks initiate between belt ply–dropped ply and core ply–dropped ply interfaces due to substantial interlaminar shear stresses arising from the load transferred from dropped plies to the belt and core plies, and these cracks propagate towards the thick section of the specimen. When it comes to the thin section, the curved belt plies tend to straighten out under tensile loading causing the belt ply–core ply interface to open at the beginning of the thin section, and the crack initiated in this interface advances towards the thin section of the specimen.

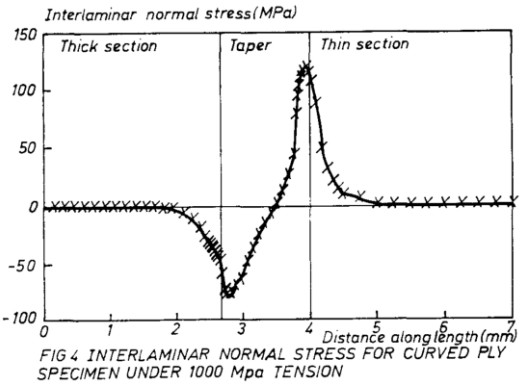

a)

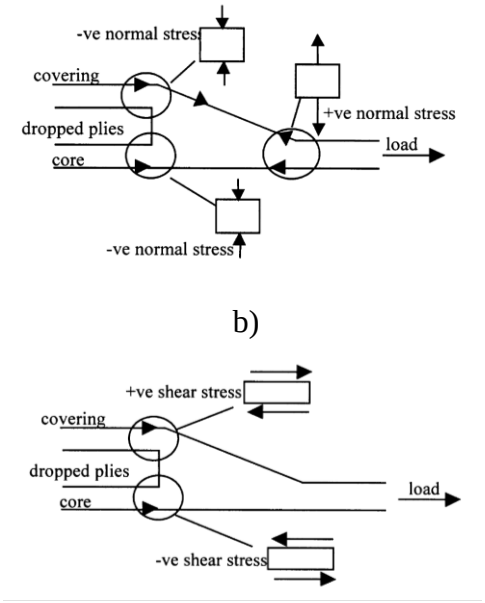

b)

c)

Figure 1.4. (a) Interlaminar normal stress distribution around a ply drop off under tensile loading [5], a schematic of interlaminar (b) normal and (c) shear stresses around a ply drop off region under tensile loading [6].

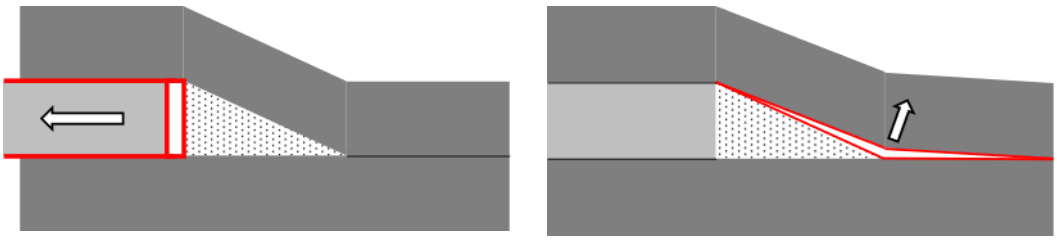

(a) Thick section delamination

(b) Thin section delamination

Figure 1.5. (a) Thick section delamination and (b) thin section delamination observed in a tapered laminate.

In the literature, numerous numerical and experimental studies, that investigate the effect of design parameters on failure initiation loads and location in ply drop-off regions, are documented. These crucial design parameters are the number of plies dropped at a station, stiffness of the dropped plies, and step spacing distance between consecutive ply termination locations.

The number of dropped plies as well as their stiffness in tapered laminates have a substantial influence on the load-carrying capacity of the composite structure. Therefore, the effects of these parameters are investigated in many studies in the literature. Wisnom et al. showed in their experimental study that if the stiffness of the dropped ply surpasses that of other plies within the laminate, it is likely to observe delamination propagating towards the thick section of the dropped ply specimen under tensile loading [3]. In another study, the effects of the number of plies dropped at a station and the stiffness of the dropped plies are explored [7]. The findings indicated that increasing the number of 0° plies and their proportion within the dropped sub-laminate led to a notable reduction in the load-carrying capacity of the composite structure. The observations from both studies converged on one conclusion: as the stiffness of the dropped ply increases, the delamination initiation load in the tapered laminate decreases. Further numerical and experimental studies substantiating these findings can be encountered in the literature [6,8,9].

Step spacing, also referred to as the stagger distance, corresponds to the gap between successive ply termination locations. The stagger distance is related to the taper angle of the laminate: low step spacing corresponds to a high taper angle, whereas greater step spacing results in a lower taper angle. Since this study focuses on highly tapered laminates and the effect of taper angle on delamination onset loads, it becomes imperative to investigate the studies examining the effects of step spacing on the load-carrying capacity of tapered laminates.

Cui et al. [10] performed both numerical and experimental studies with ply drop-off specimens under tensile loading with different stagger distances, and they concluded that if the step spacing between two consecutive ply drop-offs falls below a specific critical value, the delamination initiation load starts to decrease. Similar outcomes are obtained in another parametric study performed with finite element models, wherein the gradual reduction in the spacing between two-ply drop-offs is investigated. The findings revealed a significant reduction in the load-carrying

capacity of the laminate when the step spacing is less than three times the thickness of the dropped plies [6]. A recent experimental study performed under tensile loading with two different tapered laminates having 8.1° and 11.3° taper angles demonstrated slightly earlier delamination onset on the specimens with higher taper angles, 11.3° [2]. Furthermore, Gan et al. conducted a parametric numerical study with different single-stage ply drop-off configurations and observed a substantial reduction in the delamination onset loads as the taper angle increased [11].

As a result, increasing the taper angle of a tapered composite laminate or reducing the step spacing between ply drop-offs makes the composite structure more vulnerable to delamination and loss of load-carrying capacity. Despite numerous optimization studies performed to obtain the best performance from the tapered laminates, considering the failure mechanics and stacking sequences [12–14], it seems inevitable to observe delamination in highly tapered laminates that are designed and manufactured by conventional techniques. This underlines the importance of exploring unconventional strategies to improve the load-carrying capacity of highly tapered laminates by suppressing or delaying delamination.

1.2 Delamination Suppression Techniques in Tapered Laminates

When changing the ply-dropping order or sequence of the sub-laminate is not a viable or sufficient option, it becomes necessary to use alternative techniques to enhance the load-carrying capacity of the tapered structures. The main reason for delamination in ply drop-off regions is the combination of weak interlaminar bonding of composite materials with the high interlaminar stresses associated with the material discontinuity and taper geometry. Hence, delamination suppression methods can be categorized into two groups: one is focused on enhancing the interface, while the other aims to mitigate stress concentrations due to ply termination.

Many researchers work on novel techniques to enhance the interface properties of laminated composite materials. For instance, the advantage of the inclusion of a thin adhesive layer around the drop-off interface is reported in [15]. An improvement in the interlaminar fracture toughness of the composite material is obtained by placing vertically aligned carbon nanotube (VACNT) interleaves to the interface; therefore, the delamination initiation load in tapered laminates is increased [16]. The study of Gouldstone et al. [17] showed that VACNT forest placed in the tapered region not only enhances the load-carrying capacity of the structure but also changes the failure mode from delamination to fiber fracture. Another technique to improve the interlaminar properties of composite materials is to impregnate the resin matrix system with nanoparticles. In one study, even though the inclusion of nano clays in the resin matrix system only slightly improved the static strength of glass fiber-reinforced tapered specimens, a significant enhancement in fatigue performance was achieved [18].

Enhancing the interface properties of composite parts with nanoparticles and additional reinforcing materials poses challenges such as the need for additional material characterization studies in the design process. Therefore, improving the load-carrying capacity of tapered laminates by reducing the stress concentrations due to ply termination is also investigated in the literature. It is explained previously that an increase in the stiffness of the dropped plies leads to a reduction in the failure onset load. Therefore, Minakuchi and Takeda investigated the ply curving termination method in which 0° dropped plies are curved to 45° angle near the ply drop-off, effectively reducing the stiffness of the dropped ply. This technique improved both the load-carrying capacity and fatigue performance of the tapered structure under tensile loading [19]. In addition to lowering the stress singularities by reducing the stiffness of the dropped plies, shear stress concentrations in the thick section can be eliminated by dropping the ply gradually since the shear stress singularity arises owing to the sudden termination of the ply material [20]. Considering this, researchers at The University of Bristol introduced the state-of-the-

art tape scarfing technique to eliminate interlaminar shear stress singularities at the end of the dropped plies. This technique not only increased the delamination initiation load but also completely suppressed the delamination in laminates with low taper ratios [21,22]. Both the ply-curving termination method and the tape scarfing technique have a common objective: the reduction of shear stress concentrations due to material discontinuity at the end of the dropped plies. Consequently, their primary function is to suppress the delamination that initiates at the thick section of a laminate with a ply drop-off. However, considering the studies performed in Ref. [2,11], it becomes evident that delamination initiates at the thin section of the laminates with a high taper angle. Therefore, it is necessary to develop a technique capable of reducing the stress concentrations triggering the thin section delamination in highly tapered laminates.

In the literature, the effect of variable stagger distance on the failure characteristics of tapered laminates has been rarely investigated; because changing every stagger distance independently introduces more free parameters to the problem, which amplifies the complexity of the design of tapered structures. However, gradually increasing the taper angle from the thin section to the thick section may yield a smoother load transition and reduce the interlaminar stress concentrations due to abrupt geometry change. Therefore, variable taper angle design to suppress delamination initiation in highly tapered laminates is investigated in this study. Conventional constant taper angle design, widely adopted in the industry, and variable taper angle design, proposed in this study, are illustrated in Figure 1.6.

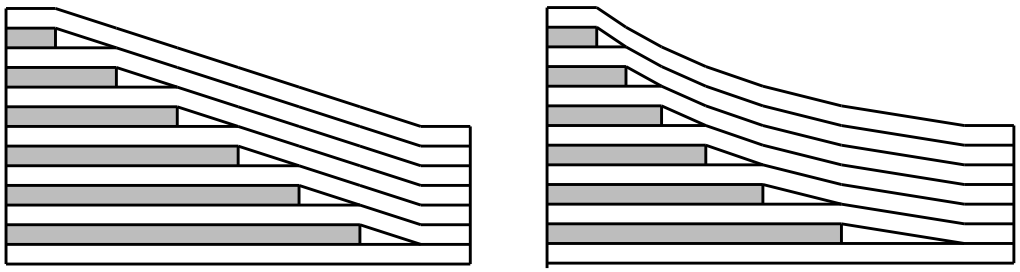

Figure 1.6. Illustration of (a) conventional constant taper angle design and (b) variable taper angle design proposed in this study.

Investigation of variable taper angle design necessitates numerous parametric studies to see the effect of different parameters affecting the load-carrying capacity of the laminate. Considering the high financial burden of conducting several experiments, it is necessary to use numerical tools to predict delamination onset loads of different tapered configurations. Hence, it becomes crucial to identify the effective and applicable delamination prediction method available in the existing literature in order to comprehensively examine the delamination phenomenon within tapered laminates.

1.3 Delamination Prediction Methods

There are several studies in the literature concerning the strength assessment of composite laminates with ply drop-offs. These studies can be categorized as strength-based and fracture mechanics-based approaches. In strength-based methods, the stress distributions around the ply drop-offs are evaluated using analytical or numerical techniques, and delamination initiation is predicted with initiation criteria. For example, Armanios and Parnas developed a simple model considering the extensional deformations in a tapered structure to capture the interlaminar stresses around ply drop-off regions, and their model is in good agreement with the finite element model in a qualitative basis [23]. In a study performed by Vizzini, a shear lag model is developed in which the resin layer between the plies is assumed to carry only shear stresses whereas only extensional deformations are allowed in the plies. This model exhibited a favorable correlation with the finite element model when only extensional load is applied to a tapered laminate [24]. He et al. [25] refined the accuracy and applicability to a wider range of problems of the shear lag model by enabling the transfer of normal stresses together with shear stress and incorporating the effects of resin cracking in their models. There are also studies modifying the Tsai – Wu failure criteria [26] by only considering the out-of-plane components of the stresses to predict the delamination in ply drop-offs [1,6]. Fish and Lee utilized the average stress concept to handle the stress singularity around the ply drop-offs,

and even though delamination location prediction closely aligns with the experiments, the predicted load corresponding to the out-of-plane failure varies significantly depending on the selection of the stress averaging distance [1]. Curry et al. [7] also used strength-based failure criteria to predict interface failure in ply drop-off regions and compared their results with the experiment. The failure criteria they used, a modified version of the Hashin matrix failure criteria [27], underpredict the failure load by 33%.

Given that stress singularities arise near the ply drop-offs, it is more convenient to use fracture mechanics approaches to investigate delamination in tapered laminates. Salpekar et al. [20] used the virtual crack closure technique (VCCT) with a 2D finite element model to investigate the mode I and mode II strain energy release rate components of the cracks propagating towards the thin and thick section of the tapered laminate. Wisnom adopted strain energy release rate equations for cut ply specimens, and his analytical results exhibited a close alignment, with a deviation of around 15%, when compared to the experimental delamination initiation loads [5]. Wisnom also notes that while the finite element model indicates elevated interlaminar stresses, the delamination does not initiate until a certain load level is reached, which underlines the necessity of the fracture mechanics approach in ply termination analysis because there are stress singularities in the region. In another study, Petrossion and Wisnom developed an analytical solution for predicting the delamination in a ply drop-off region subjected to combined bending and tension loading, and they performed a parametric study to understand the factors affecting the performance of tapered laminates [8]. In the study of Allegri, Wisnom, and Hallet [28], a numerical model is developed to predict the delamination onset load in tapered laminates by using an analytical methodology in which the energy release rate of cracks propagating towards both thick and thin sections of a tapered laminate is computed. The tapered laminate is modeled with a combination of layered Euler-Bernoulli beams for computational efficiency. The model is validated with finite element models and experiments in the second part of the study in Ref. [29]. The model showed conservative results in terms of strain energy release rates and

delamination onset loads. The numerical model presented in Ref. [28,29] is improved by replacing Euler-Bernoulli beams with shear deformable Timoshenko beams and the model is also compared with finite element models [11]. Results indicated that while the analytical model with Timoshenko beams might underpredict the delamination initiation loads, it still proves sufficient for conducting a comparative study of the load-carrying capacity of various ply-dropping alternatives in the preliminary design stage.

Even though strength-based and fracture-based numerical tools can be practical in simple comparative studies, they lack the capability to predict the load-carrying capacity of the complex tapered laminates accurately. Therefore, it is necessary to use high-fidelity finite element models, as introduced in Ref. [30], to predict the load-carrying capacity of tapered laminates accurately. In this work, researchers constructed the detailed finite element model of the actual specimen based on its microscopic image and placed cohesive elements in all interfaces to predict delamination. The results showed that load load-carrying capacity of tapered laminates with internal ply terminations can be predicted accurately with high-fidelity modeling techniques. Zhang et al. [2] applied the high-fidelity modeling technique in modestly and severely tapered laminates and observed that it is necessary to use the correct interface strength properties in highly tapered laminates to capture the failure load and location in the structure correctly. Therefore, it is concluded that detailed finite element models incorporating cohesive elements within the interfaces are necessary for accurately predicting both the delamination onset load and location in ply drop-offs.

1.4 Enhancement of Interface Properties

Despite its effectiveness and accuracy, built-in cohesive elements in commercial finite element software do possess limitations, considering the effect of through-thickness compression on mode II fracture energy and shear strength. This limitation

becomes critical in the analysis of ply drop-offs due to combined shear and compressive stresses at the end of the dropped plies.

Wisnom conducted an experimental investigation using cut-ply specimens of varying thicknesses and compared delamination propagation loads with the energy release rate calculation [5]. His observations indicated that as the specimen thickness increases, the energy release rate calculations tend to underpredict the delamination propagation load. Conversely, in the case of thin specimens, the experimental load is overpredicted with the calculations. Following these findings, Wisnom postulated that the fracture energy of the material might not be constant but rather vary with the laminate's thickness. Subsequent investigations revealed that the primary factor in the variation of the fracture energy is the enhancement of the interface properties due to the presence of compression, a phenomenon that has been reported in numerous experimental studies. For instance, DeTeresa et al. [31] conducted combined shear and compression tests on hollow composite specimens, and significant shear strength enhancement was observed with the presence of compression. Cartie et al. [32] performed Mode I and Mode II fracture energy tests on a composite/epoxy laminate under varying hydrostatic pressure conditions. Their observations indicated that the mode II fracture toughness of the material is enhanced as the pressure is increased. Gan, Hallet, and Wisnom [33] performed biaxial testing on a symmetric version of double-notch carbon/epoxy specimens under tensile loading while simultaneously applying a transverse compressive load. The shear strength of the material exhibited an improvement as the compressive load was increased. The same test setup is employed with cut-ply specimens, and the enhancement of Mode II fracture toughness with the presence of through-the-thickness compression is also demonstrated [34]. Additionally, in another study [35], tensile load is applied to transverse crack specimens, and through the thickness compressive stress is applied with the clamping of the specimens with a custom-designed fixture. The test results with varying values of transverse compressive stress showed that the Mode II fracture toughness of the material increases as the compressive stress is increased. In conclusion, numerous experimental studies demonstrated that the presence of

through-thickness compression in a composite laminate leads to an enhancement in the shear strength and mode II fracture toughness of the laminate.

To overcome the conservativeness of numerical studies when predicting shear crack behavior under compressive stresses, many studies are performed to take the enhancement into account. Cui et al. proposed a new method to calculate the fracture toughness of the composite material by defining fracture energy by a function of normal stresses [36]. Li et al. [37] developed interface elements with bilinear traction separation response, taking the enhancement of the shear strength and Mode II fracture toughness under compressive stress into account. Their study demonstrated that the model can be applicable to various specimen types to capture the enhancement effect. The same interface elements are used in experimental studies for calculating the enhancement factor for the shear strength [33] and mode II fracture energy [34]. Zou and Lee developed a new cohesive zone model taking the effect of compressive stresses on shear strength and fracture energy [38]. They also included the frictional effects on the fracture surface due to microcracks formation.

The development of custom interface elements is necessary to take the compression into account in delamination analysis because built-in cohesive elements in commercial finite element software do not take the compression effect on shear strength and fracture toughness into account. However, it can be impractical to develop custom interface elements from scratch due to time limitations and lack of experience. Therefore, some studies are performed to take the enhancement of the interface properties with compression into account in a more practical way by using user-defined field variable subroutines [35,39]. User-defined field variables subroutine allows users to change the material properties of the built-in elements depending on the field variables such as compressive stress experienced by the element. Therefore, enhancement of the shear strength and mode II fracture toughness can be incorporated without developing custom cohesive elements. Therefore, a simple user-defined field variable subroutine in ABAQUS is developed in this study to consider the enhancement of interface properties under through-thickness compressive stresses.

1.5 Scope of the Thesis

The main objective of the study is to gain an understanding of failure mechanisms in laminates with a ply drop-off and suppress delamination in highly tapered laminates. To verify the finite element model and investigate the necessary parameters in the delamination analysis of a laminate with a ply drop-off, a series of material characterization tests and ply drop-off experiments are conducted. To predict delamination in tapered laminates, the cohesive zone modeling technique is adopted, and a practical user-defined subroutine (USDFLD) is developed for built-in cohesive elements in ABAQUS to take into account the enhancement of the shear strength and mode II fracture toughness due to compression. The effect of fracture toughness around the resin pocket and voids on delamination onset loads is investigated numerically. A parametric taper angle study is performed to see the effect of taper angle on delamination onset load and location. A method to define the variable taper geometry with a single parameter is also proposed so as not to introduce excessive design parameters to the problem. A significant advantage of variable taper angle design compared to constant taper angle design is demonstrated through finite element analysis.

This study is structured into five chapters. Chapter 1 provides a literature review on tapered laminates and outlines the study's objectives. Chapter 2 encompasses composite material characterization tests and experiments involving single-stage dropped ply specimens. It also includes manufacturing details for pure epoxy specimens using the resin casting technique and information on the controlled pre-cracking method developed in this study for the preparation of toughness specimens. Chapter 3 introduces the numerical tools employed for predicting delamination in the analysis of ply drop-off. Details of the USDFLD subroutine for taking the shear enhancement effect due to compression with a built-in subroutine are presented. Finite element model details such as mesh size, cohesive element properties, and boundary conditions are given. It also includes the comparison of the simulation of

dropped ply specimen results with the experimentally observed failure sequences and corresponding load levels. Chapter 4 introduces and investigates the variable taper angle design concept, aiming to suppress delamination in highly tapered laminates. Chapter 4 also includes a discussion about a method to define the taper curvature with a single parameter to reduce the number of design options. In Chapter 5, the general outcomes of the study and possible future works are listed.

CHAPTER 2

GFRP MATERIAL CHARACTERIZATION TESTS AND PLY DROP-OFF EXPERIMENTS

2.1 Introduction

The prediction of delamination in ply drop of regions through finite element analyses necessitates the knowledge of the mechanical properties of the material. In this study, CR80/CH80-6 epoxy/hardener resin system and Interglass 92145/CR80 glass fiber composite material are used. Technical specifications of Interglass 92145 glass fabric and CR80 resin systems are given in Ref. [40] and Ref. [41], respectively. Figure 2.1 illustrates the essential material properties and their required locations crucial for the prediction of delamination within a ply drop-off region using finite element models.

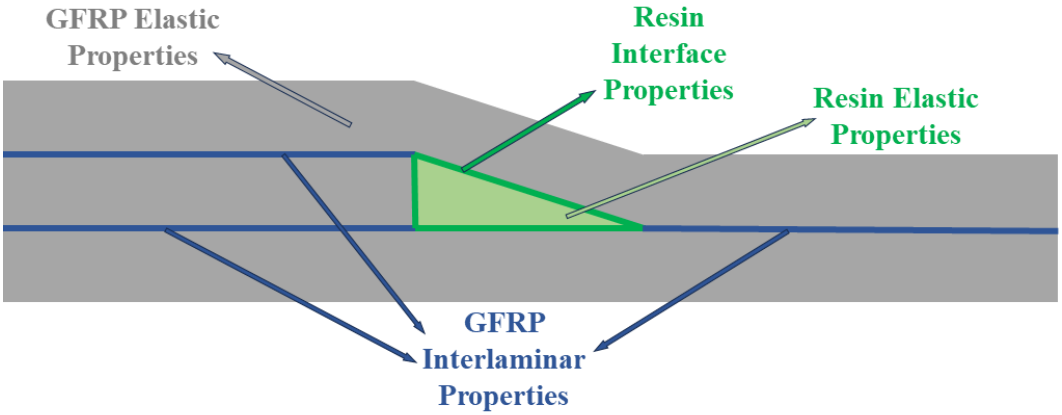

Figure 2.1. Illustration of a ply drop off region with necessary material properties and their locations for a finite element model.

In this chapter, a systematic experimental campaign is conducted to acquire the mechanical properties of the materials employed in the present study. Specimen types and corresponding material properties are listed in Table 2.1. The obtained material properties are used in Chapter 3 for the numerical prediction of delamination

within ply drop-off regions. Additionally, in this chapter, a tapered specimen with a single-stage ply drop-off region is investigated under tensile loading, and the failure sequence is recorded with a high-speed camera to identify the failure mechanism in ply drop-off regions.

Table 2.1. The list of material properties and corresponding standards used in material characterization tests performed for Interglass 92145/CR80 glass fiber composite material and CR80/CH80-6 epoxy/hardener system.

	Specimen	Standard	Parameter
GFRP Elastic and Strength Properties	0° Tension	ASTM D3039	E_1, v_{12}, X_T
	90° Tension	ASTM D3039	E_2, Y_T
	$\pm$45° Tension	DIN EN 6031	G_{12}, S_{12}
GFRP Interlaminar Properties	ILSS	ASTM D2344	τ_s^0
	DCB	DIN EN 6033	G_{Ic}
	ENF	DIN EN 6034	G_{IIc}
Resin Elastic and Interface Properties	Tension	ASTM D638	$E_{resin}, v_{resin}, (\tau_n^0)_{resin}$
	SENB	ASTM D5045	$(G_c)_{resin}$

2.2 GFRP Elastic and Strength Properties

In order to define the elastic response of GFRP used in this study, elastic properties must be obtained. Even though fiber fracture is not considered in numerical studies, the strength properties of the composite material are also obtained and reported in this section. The related material properties of composite material are obtained through a series of tension experiments with fiber orientations in 0°, 90° $\pm$45°.

2.2.1 Specimen preparation

The specimens are manufactured by Odak Composite Technologies [42]. Glass fiber plies are placed on top of each other, and the impregnation of the fibers with the

CR80/CH_6 resin system is performed through vacuum pressure. 12, 12, and 8 layers of plies are used for 0° tension, 90° tension, and ±45° tension specimens, respectively. Following a 24-hour curing period at the room temperature, the composite plates undergo an additional post-curing phase for 8 hours at a temperature of 80 °C. The specimens are then cut from the plates into rectangular parts with dimensions of 250 mm x 25 mm with a water jet, and glass fiber tabs are glued to the specimens to reduce the stress concentrations due to the gripping of the test machine. After the manufacturing process, stochastic paint is applied to the specimens for DIC measurement. Specimens before testing are shown in Figure 2.2.

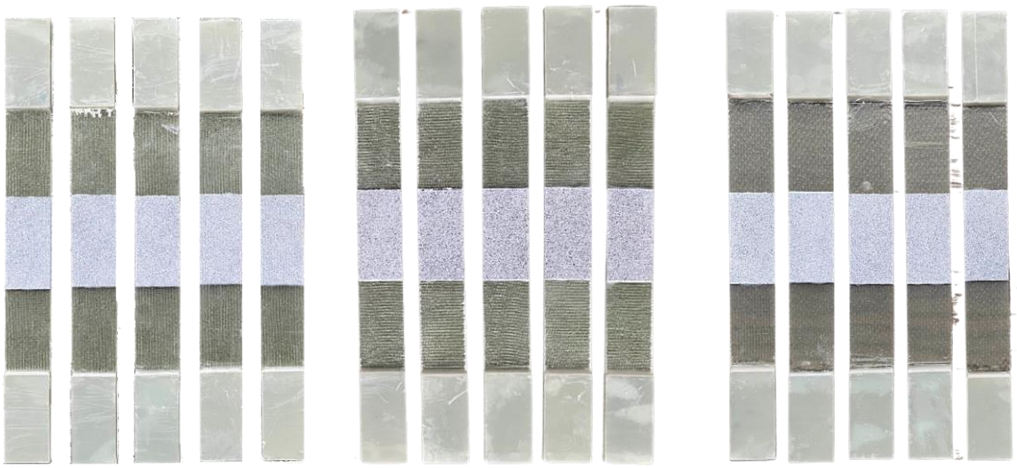

Figure 2.2. GFRP tensile test specimens.

2.2.2 Experimental Method

The test setup used for tension experiments of GFRP specimens is shown in Figure 2.3. The servo-hydrolic testing machine of MTS with 100kN load cell capacity is used. Specimens are gripped from the tabs with 12 MPa of pressure. The lower crosshead of the testing machine is moved with displacement control at a speed of 2mm/min for 90° and 0° tension specimens, and 1mm/min for ±45° tension specimens. Strain measurements are conducted by using the Digital Image Correlation (DIC) system. The region with stochastic paint is recorded at a rate of 4

Hz with GOM 4 MP DIC camera. ARAMIS DIC postprocessing program [43] is used for strain calculations.

Figure 2.3. Test setup for the tension tests.

2.2.3 Results

Five specimens for each group are tested and fractured specimens are shown in Figure 2.4. No sign of sliding is observed in the grip sections of the specimens. Strength and elastic properties are calculated according to the related standards, and they are listed in Table 2.2. C.V. given in the table stands for the coefficient of variation, and its calculation is given in Equation (2.1). Test results for all individual specimens are provided in Appendix A.

$$\text{Coefficient of Variation} = \frac{\text{Standard Deviation}}{\text{Average}} \text{ x } 100 \qquad (2.1)$$

Figure 2.4. GFRP specimens after tensile testing.

Table 2.2: In-plane properties of Interglass 92145/CR-80 composite material.

Property	Value	C.V. (%)
E_1	38.88 GPa	2.41
E_2	12.16 GPa	10.34
v_{12}	0.266	3.96
G_{12}	4.60 GPa	3.02
X_T	710.59 MPa	4.99
Y_T	44.22 MPa	3.21
S_{12}	105.19 MPa	3.71

2.3 GFRP Interlaminar Properties

Prediction of delamination onset and propagation in composites laminates requires the knowledge of the interlaminar strength and fracture toughness of the material. Therefore, characterization tests aimed at obtaining the interlaminar properties of GFRP material used in this study are performed in this section.

2.3.1 Interlaminar Shear Strength (ILSS) Test

The interlaminar shear strength of Interglass 92145/CR80 is determined through the execution of a short beam strength test, conducted in accordance with the ASTM D2344 standard.

2.3.1.1 Specimen preparation

The specimens are manufactured by Odak Composite Technologies. Forty layers of glass fiber plies are sequentially stacked, and the impregnation of the fibers with the CR80/CH80_6 resin system is performed through vacuum pressure. Following a 24-hour curing period at room temperature, the composite plates undergo an additional post-curing phase for 8 hours at a temperature of 80 °C. The specimens are precision-cut from the composite plates by employing a water jet cutter, resulting in rectangular components having dimensions of 40 mm in length, 12 mm in width, and an average thickness of 6.57 mm. The dimensions of the specimens are measured with a caliper.

2.3.1.2 Experimental Method

Three-point bending fixture suitable to the standard is attached to the MTS servo-hydraulic uniaxial testing machine with 250kN load cell capacity. The test setup is shown in Figure 2.5. The spacing between the supports is set at 26 mm, approximately four times the thickness of the specimen as stated in the standard. The specimens are positioned onto the testing fixture, and tests are conducted under displacement control at a rate of 1mm/min.

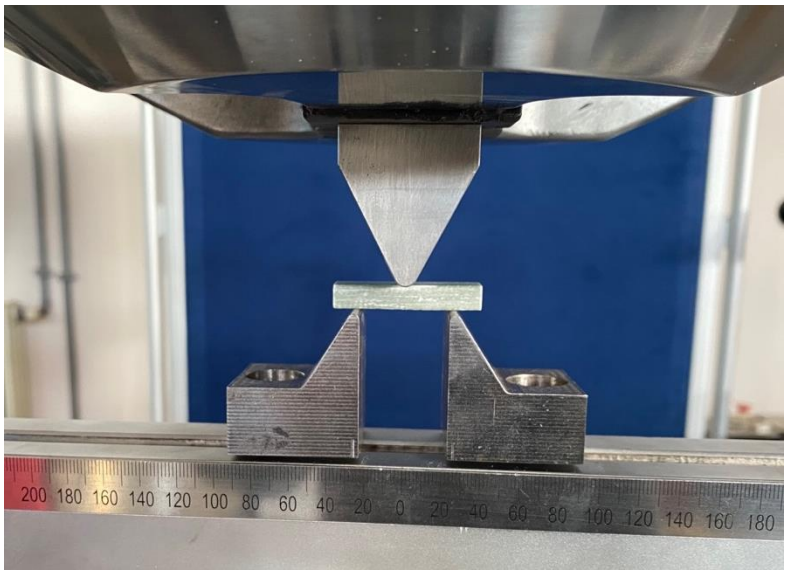

Figure 2.5. Three-point bending test setup for ILSS tests.

2.3.1.3 Results

Six specimens underwent testing, and in each case, interlaminar shear failure is observed. One of the specimens after the interlaminar shear failure is shown in Figure 2.6. After the first failure in one interface, multiple failures occurred at the other interfaces. The load corresponding to the first interlaminar shear failure is selected as the failure load. The average shear strength of the specimens is calculated as 45.80 MPa with a coefficient of variation of 6.09%. Test results for all individual specimens are provided in Appendix A.

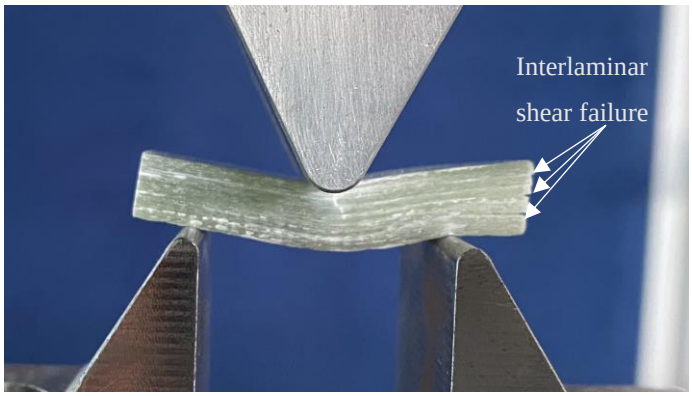

Figure 2.6. Interlaminar shear failure of an ILSS specimen.

2.3.2 Mode I Fracture Toughness Test (DCB)

To determine the interlaminar Mode I fracture toughness of the laminate, double cantilever beam (DCB) tests are carried out following the guidelines outlined in the DIN EN 6033 standard.

2.3.2.1 Specimen preparation

Specimens are manufactured by Odak Kompozit. 16 layers of Interglass 92145 unidirectional glass fiber plies are combined with the CR80/CH_6 resin system by using the vacuum infusion technique. Teflon release film is placed at the midplane of the laminate in order to create an initial crack length of 25 mm as stated in the standard. The dimensions of the specimen from the standard are given in Figure 2.7(a). Following the resin infusion, the laminate is allowed to cure at the room temperature for a duration of 24 hours. Subsequently, the laminate is post-cured at 80 $°C$ for 8 hours. The final laminate is cut into rectangular pieces having dimensions of 250mm x 25 mm with a water jet cutter. The sides of the specimens are coated with a brittle white paint to increase the visibility of the crack tip during the tests. The hinges are attached to the specimens with Pattex Super Glue. The DCB specimens before and after paint application and hinge attachment are shown in Figure 2.7.

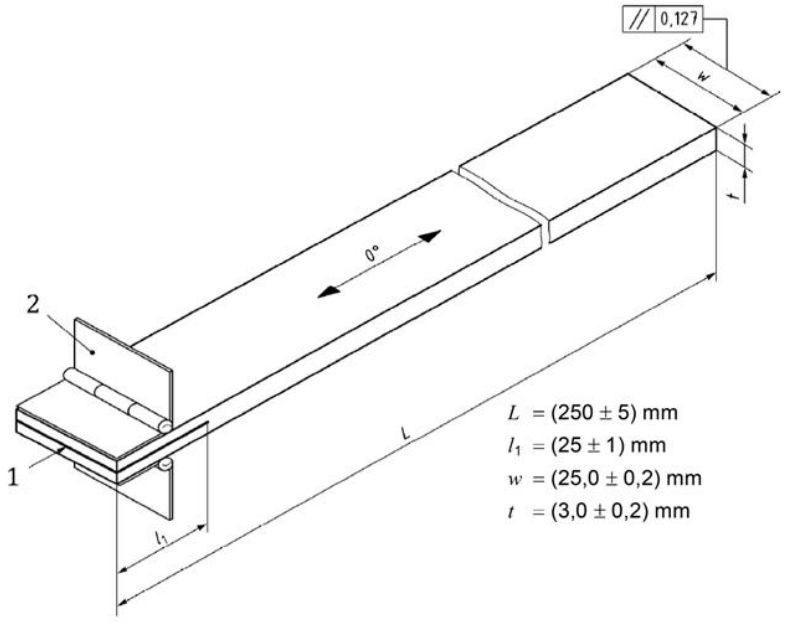

(a)

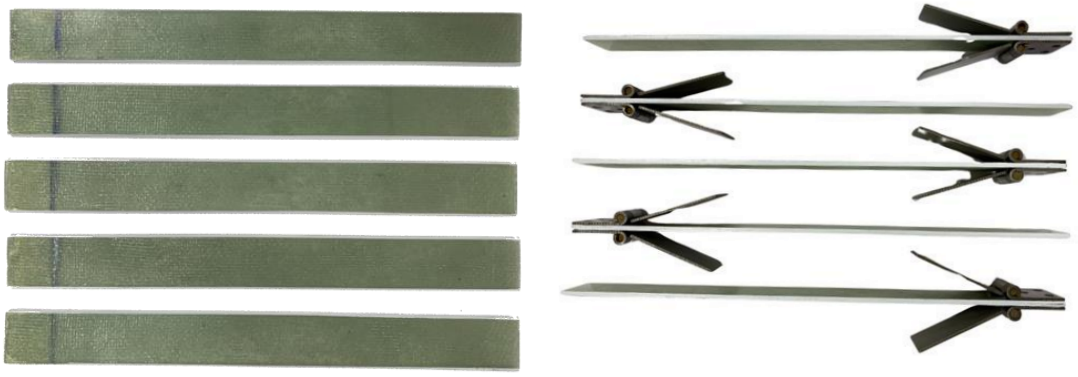

(b) (c)

Figure 2.7. (a) Dimension of DCB specimens given in DIN EN 6033 standard, (b) DCB specimens after the water jet cutting process, (c) DCB specimens with hinges attached and white paint is applied.

2.3.2.2 Experimental Method

Tests are conducted with SHIMADZU AGS-J servomechanical testing device, equipped with a 10 kN load cell, as shown in Figure 2.8(a). Tension grips are employed to grasp the DCB specimens from the hinges. The tension grips in operation as they pull a DCB specimen during the experiment are shown in Figure 2.8(b).

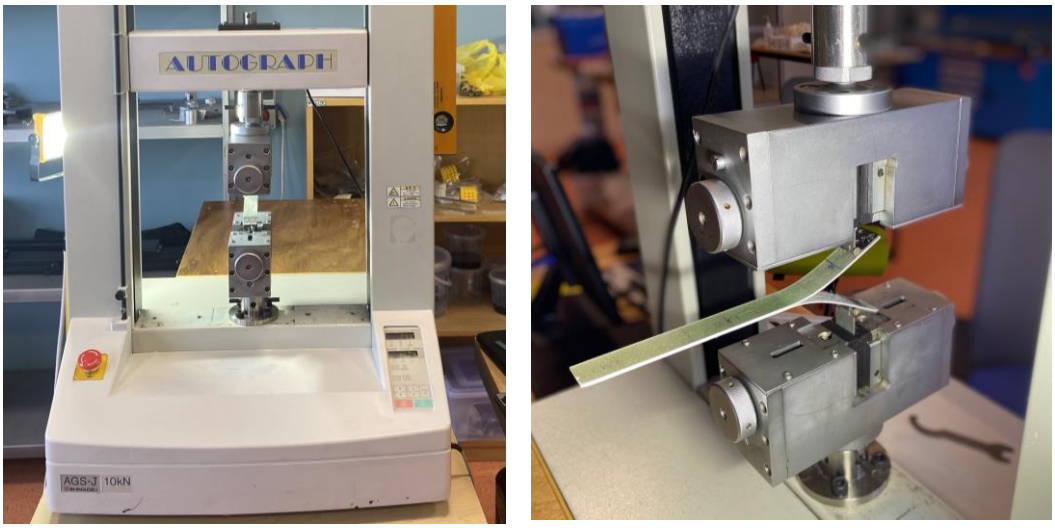

(a) (b)

Figure 2.8. Test setup for DCB tests.

The tests are conducted under displacement control at a rate of 10mm/min as stated in DIN EN 6033. To ensure the introduction of a natural crack in the specimens, they undergo an initial loading phase until the the crack propagates a range of 10 to 15 mm. Subsequently, unloading is performed. Due to the transparency of the GFRP specimens, the location of the crack tip can be visually observed from either the top or the bottom of the specimens, as shown in Figure 2.9. After creating the natural crack, the position of the crack tip is marked with a pen before the actual test. The specimens undergo a subsequent loading phase under displacement control, with a test rate set at 10 mm/min, continuing until the crack tip propagates a distance of 100 mm. Finally, the specimens are unloaded, and the total propagated crack length is measured with a caliper.

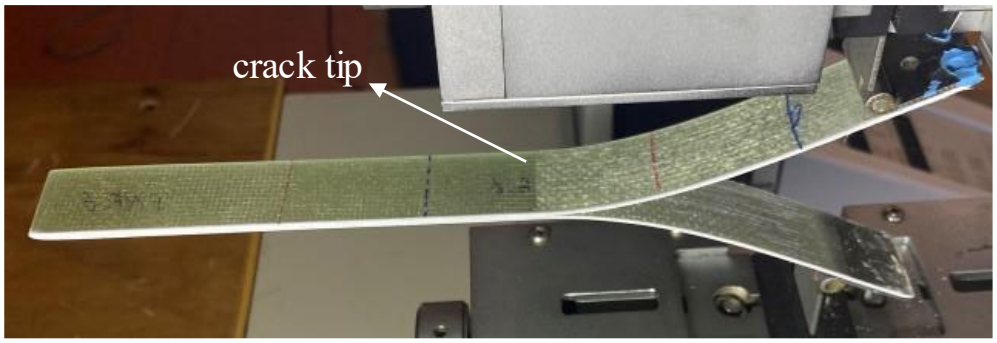

Figure 2.9. The crack tip which can be observed at the top of a GFRP DCB specimen

2.3.2.3 Results

A typical load-displacement curve for a DCB specimen is shown in Figure 2.10. The Mode I energy release rate of the DCB specimens can be calculated by using Equation (2.1) as stated in the standard.

$$G_{IC} = \frac{A}{a \text{ x } w} \tag{2.1}$$

In Equation (2.1), A is the released energy during the crack propagation, which is the area between the loading and unloading curves as shown in Figure 2.10. a and w are the total propagated crack length and width of the specimen, respectively. Five specimens were tested, and Mode I fracture toughness of the laminate is obtained as 0.886 N/mm with a coefficient of variation of 20.3%. Test results for individual specimens are given in Appendix A.

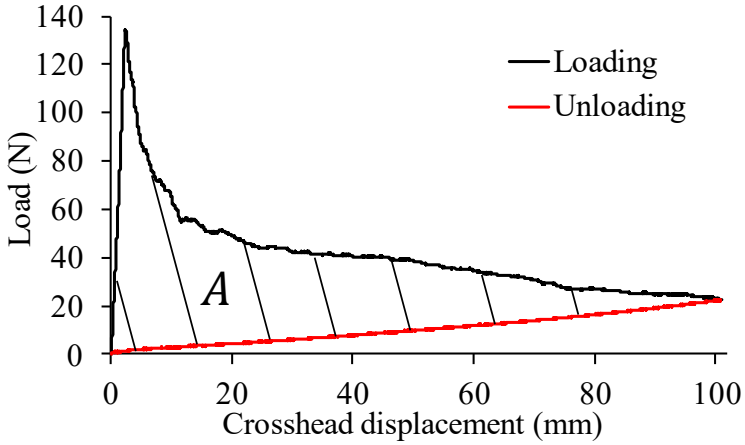

Figure 2.10. A typical load-displacement curve for a DCB specimen.

2.3.3 Mode II Fracture Toughness Test (ENF)

To ascertain the interlaminar shear toughness of the laminate, an end-notched flexure (ENF) test is conducted following the guidelines outlined in DIN EN 6034. The ENF specimens are prepared by cutting the DCB specimens as specified in the standard.

2.3.3.1 Specimen preparation

The specimens tested in DCB experiments, shown in Figure 2.11(a), are cut into length of 180 mm lengths for ENF tests using Presi Mecatome T260 cutter equipped with a diamond saw blade. The position corresponding to the bottom left support of the three-point bending fixture on the side of ENF specimens is marked with a pen. The final ENF specimens are shown in Figure 2.11(b).

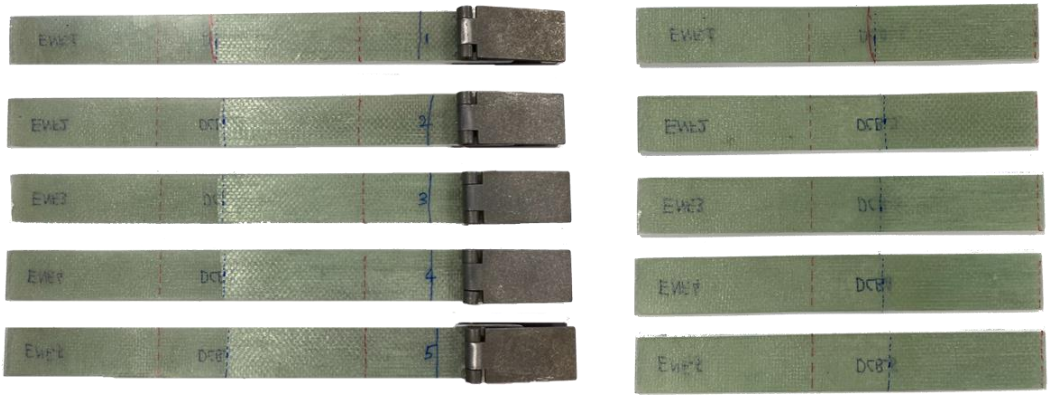

(a) (b)

Figure 2.11. (a) Toughness specimens after the Mode I fracture toughness tests, (b) Mode II toughness specimens after the cutting process for ENF tests.

2.3.3.2 Experimental Method

SHIMADZU AGS-J servomechanical testing machine with a 10 kN load cell capacity is utilized in this experiment. Three-point bending fixture is attached to the machine and the distance between the bottom supports is adjusted to 100 mm. The specimen is placed into the fixture such that the distance between the crack tip and the nearest support is 35 mm. The specimens are loaded under a displacement control at a rate of 1mm/min. The ENF test setup used in this study is shown in Figure 2.12.

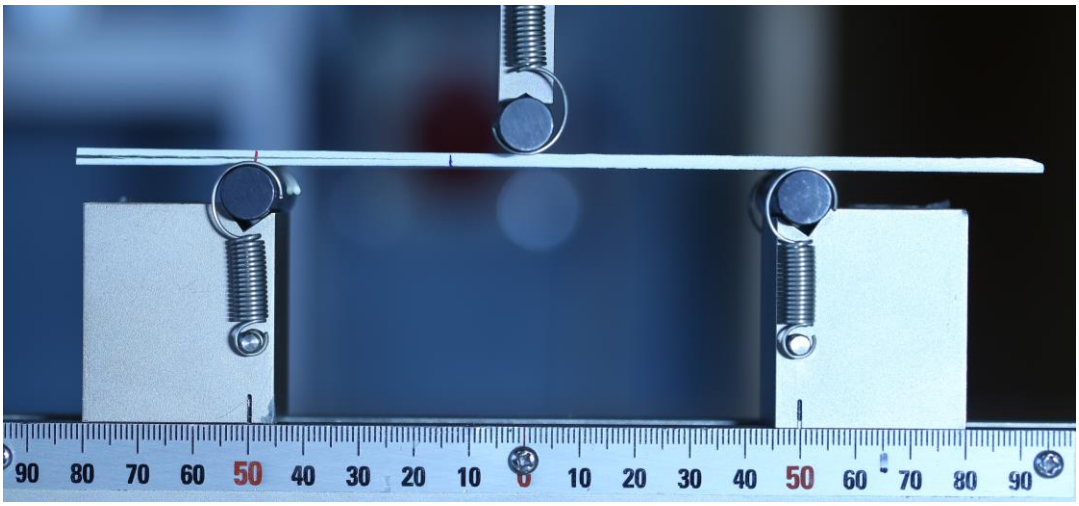

Figure 2.12. ENF test setup.

2.3.3.3 Results

Five specimens underwent testing to calculate the interlaminar fracture toughness in the shear direction, and a representative load-displacement response for an ENF specimen is illustrated in Figure 2.13. The first softening load is the delamination propagation load, P , and it is used in fracture toughness calculations. Mode II critical energy release rate of the laminate is calculated by using Equation (2.2) according to DIN EN 6034.

$$G_{IIC} = \frac{9Pa^2d}{2w(1/4L^3 + 3a^3)} \tag{2.2}$$

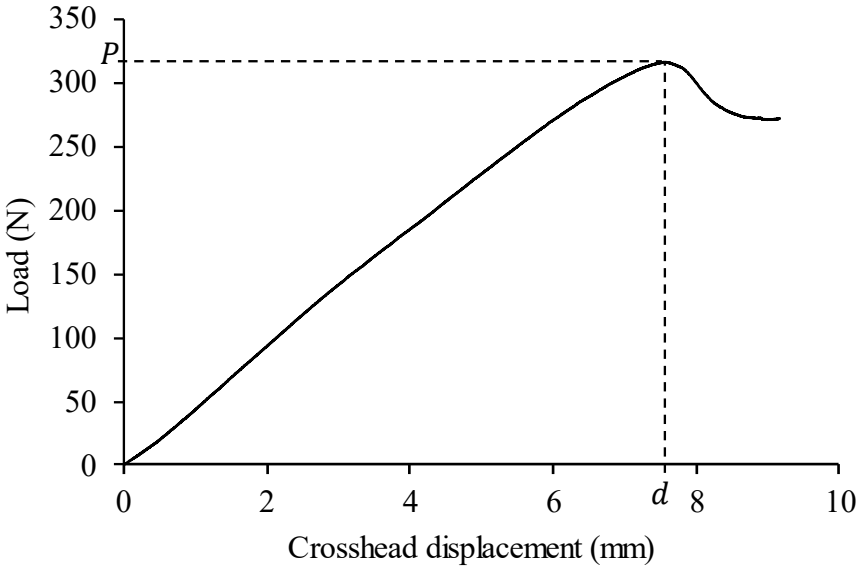

Figure 2.13. A typical load-displacement response for an ENF specimen.

In Equation (2.2), P is the critical load to start the crack, a is the initial crack length between the nearest bottom support and the crack tip, d is the crosshead displacement corresponding to delamination onset, w is the width of the specimen, and L is the distance between roller supports. After the calculations, the interlaminar shear toughness of the laminate is obtained as 1.207 N/mm with a coefficient of variation of 10.8%. Test results for individual specimens are provided in Appendix A.

2.4 Resin Elastic and Interface Properties

In the study, CR80/CH80-6 epoxy/hardener system is used. The low viscosity of the system makes it suitable for manufacturing composite specimens with the vacuum infusion technique. Given the presence of a resin-rich region in the ply termination locations, it is necessary to obtain the mechanical properties of the resin system to use in numerical studies.

2.4.1 Tension Experiment

In order to obtain the elastic properties of the resin system, tension tests are performed by following ASTM D638 standard. Dogbone specimen geometry is determined according to the standard, and the dimensions are given in Figure 2.14.

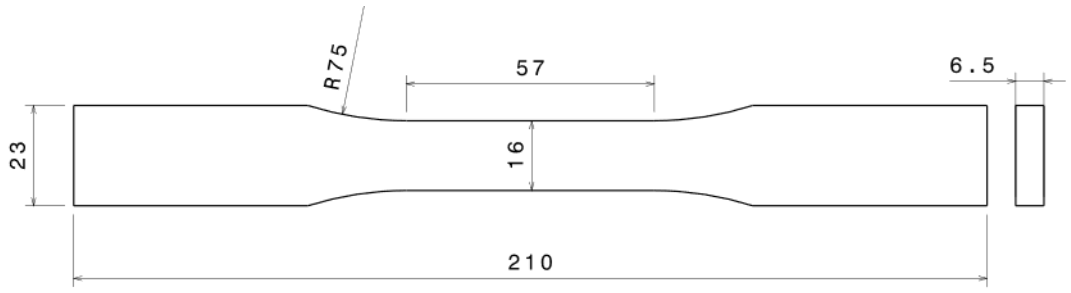

Figure 2.14. Dimensions of the dogbone specimen. All dimensions are in mm.

2.4.1.1 Specimen Manufacturing and Preparation

Pure epoxy dogbone specimens are manufactured by using the resin casting method. The manufacturing process is summarized in 3 different stages and illustrated in Figure 2.15. In the first stage, the required mold in the casting method is produced. The mold material should allow easy removal of the specimen. Therefore, RTV-2 mold silicon is selected due to its outstanding flexibility, which enables easy demolding of the specimen after solidification. However, to obtain the silicone mold for the resin casting, it is necessary to have a replica specimen model, which is produced by 3D printing. One of the most critical details while producing the silicone mold from an additively manufactured model is that indentations on the surface of the printed part are transferred to the mold, which causes bubble formation during the casting process even though all the bubbles during the resin stirring phase are evacuated before casting. Since the formation of air bubbles can reduce the strength of the resin, the rough surface of the additively manufactured model is polished before pouring RTV-2 silicone on it. After polishing, the replica model and 3D printed frame, which specifies the outer boundary of the mold, are glued to a table

and liquid silicone is poured on the model. After waiting at room temperature for 24 hours, solidified silicone is removed from the frame and the mold is obtained.

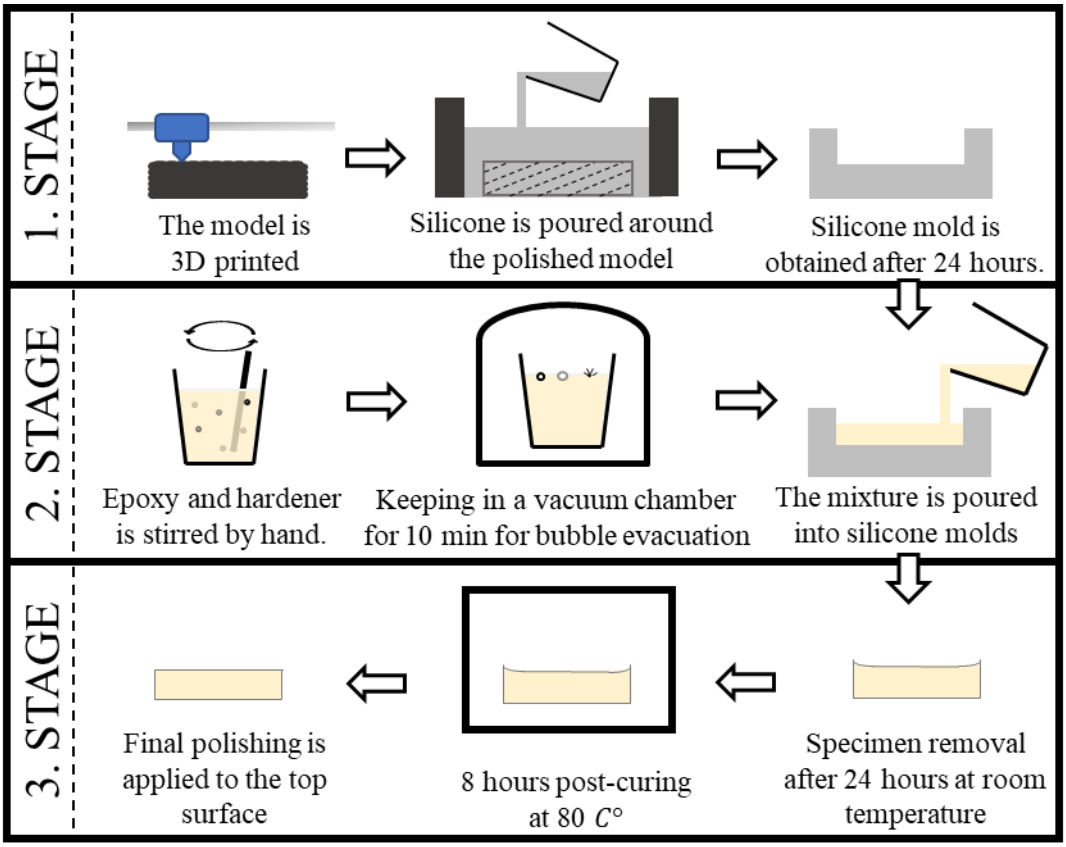

Figure 2.15. Summary of the manufacturing process of the pure epoxy specimens.

In the second stage, the resin casting is performed. The CR80 epoxy is mixed with the hardener and stirred by hand and placed in a vacuum chamber for 10 minutes to eliminate the bubbles which are formed during the mixing stage. Then, the epoxy is poured into the silicone molds and kept at room temperature for 24 hours before moving on to the third stage. Figure 2.16 illustrates the appearance of the silicone molds after the epoxy has been poured into them. Solidified resin parts are removed from the silicone molds in the third stage and placed in Nüve FN120 dry air sterilizer for post-curing at 80 $C°$ for 8 hours. Post-curing conditions are determined according to the manufacturer's suggestion, and the same post-curing condition is applied by the manufacturer to the GFRP specimens used in this study. At the end of the third

stage, the top layers of the resin parts are polished, and the manufacturing process is completed. The dogbone tension specimens at the end of the manufacturing process are shown in Figure 2.17.

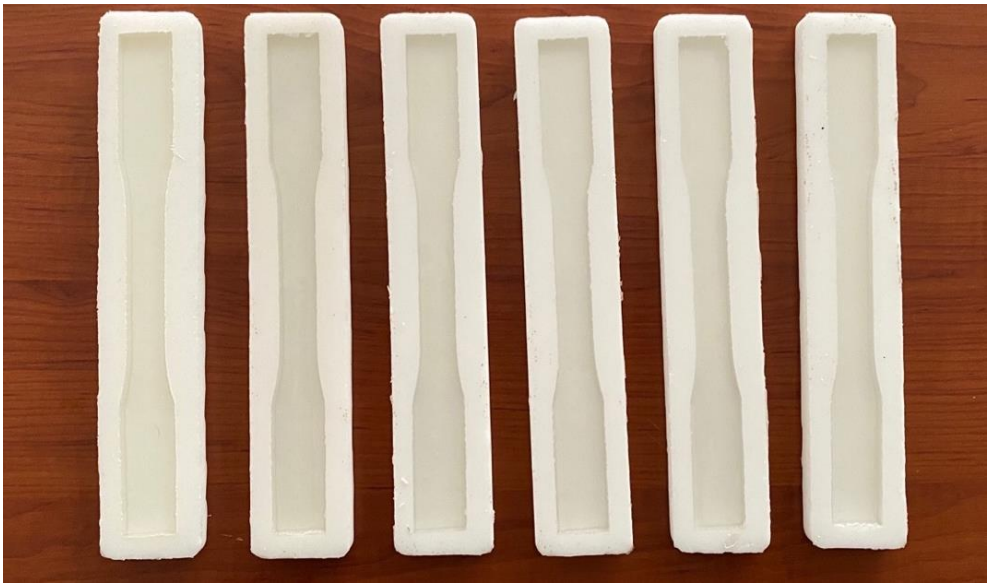

Figure 2.16. The view of the silicone molds after the epoxy is poured into them.

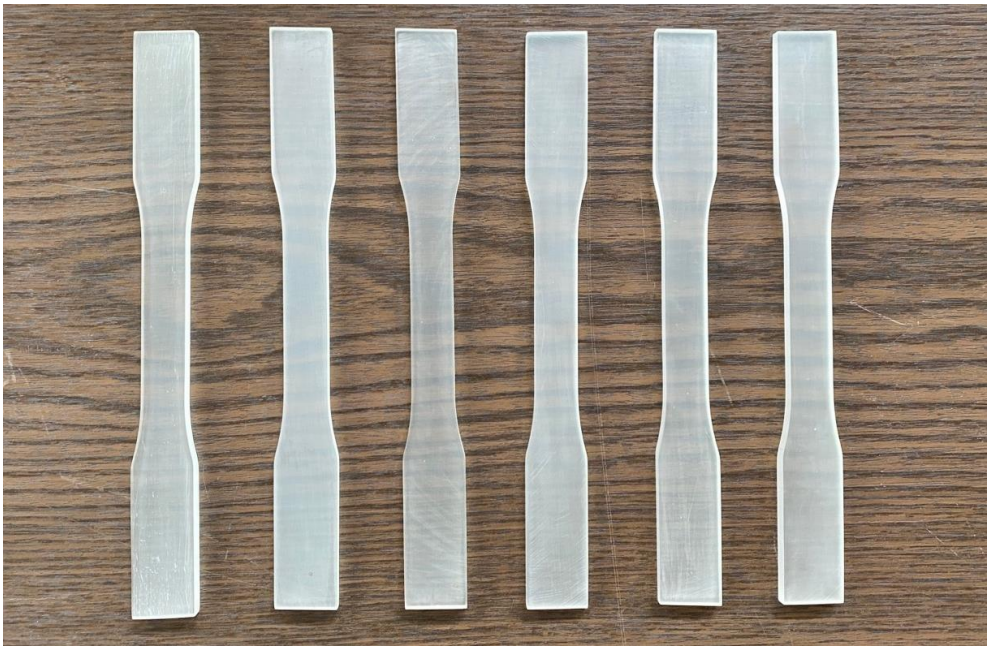

Figure 2.17. The dogbone tension specimens after the manufacturing process.

2.4.1.2 Experimental Method

The experimental setup used for the tensile test used in GFRP tension tests, shown in Figure 2.3, is also used for pure epoxy dogbone tension specimens. MTS servohydraulic testing machine with a 100 kN load cell capacity is used for the testing. Specimens are fixed with a grip pressure of 3.5 MPa. The lower crosshead of the testing machine is moved with displacement control at a rate of 5 mm/min as stated in the standard. Strain measurements are conducted by using the Digital Image Correlation (DIC) system. The region with stochastic paint is recorded at a rate of 4 Hz with GOM 4 MP DIC camera. ARAMIS DIC postprocessing program is used for strain calculations.

2.4.1.3 Results

All the specimens failed in the gage section and no sign of sliding is observed in the regions where the testing machine grips the specimens. Dogbone specimens after the tensile testing are shown in Figure 2.18.

Figure 2.18. Fractured CR80 resin system dogbone specimens after tensile testing.

The nonlinear stress-strain response of the CR80/CH80-6 epoxy/hardener system tested in the current study is shown in Figure 2.19. The tensile properties of the epoxy system were determined within the linear range of the experimental stress-strain

curves between 1000 $\mu\varepsilon$ and 4000 $\mu\varepsilon$, and results are listed in Table 2.3. The low value of the coefficient of variation, around 3%, for the material properties indicates the repeatability of the manufacturing process. Test results for individual specimens are given in Appendix A.

Table 2.3. Mechanical properties of CR80/CH80_6 resin system obtained from the tension tests.

	Tensile Strength (MPa)	Elastic Modulus (GPa)	Poisson's Ratio
Average	77.77	3.22	0.385
C.V. (%)	2.29	3.03	3.56

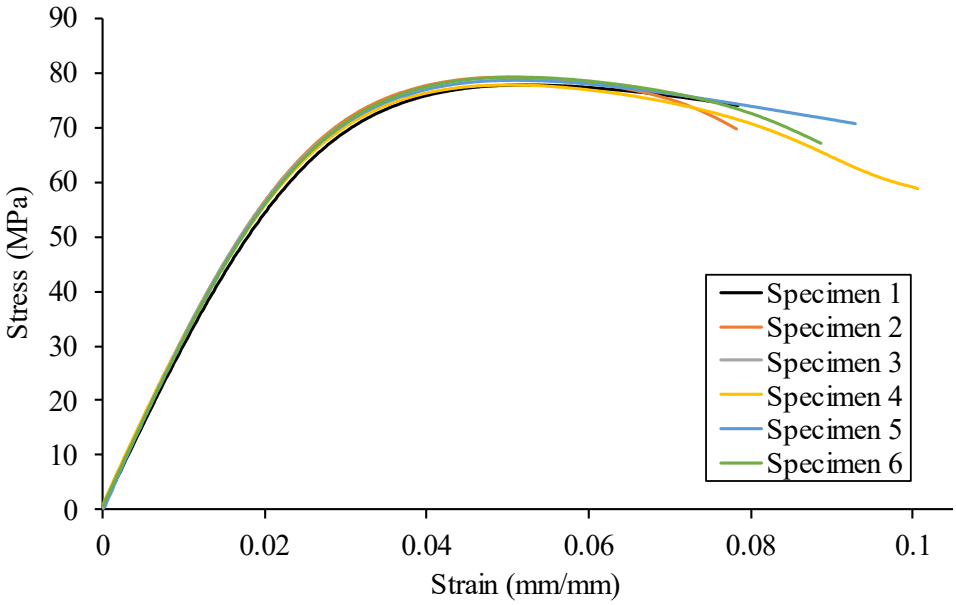

Figure 2.19. Stress-Strain response of dogbone specimens of CR80/CH80-6 epoxy/hardener system under tensile loading.

2.4.2 Fracture Toughness Experiment

To predict the crack propagation around the resin pocket, it is also necessary to obtain the fracture toughness of the resin material. Therefore, the required specimen preparation procedure and testing for the acquisition of the plain strain fracture toughness of the epoxy system are performed in this section.

2.4.2.1 Specimen preparation

Fracture-toughness specimens are also manufactured by using the resin casting method, which requires special silicone molds for these specimens. Therefore, the same manufacturing steps explained in the previous section for dogbone tension specimens, also summarized in Figure 2.15, are followed for the manufacturing of the fracture toughness specimens. The dimensions of the single-edge notched beam (SENB) specimen are determined in accordance with ASTM D5045 and shown in Figure 2.20.

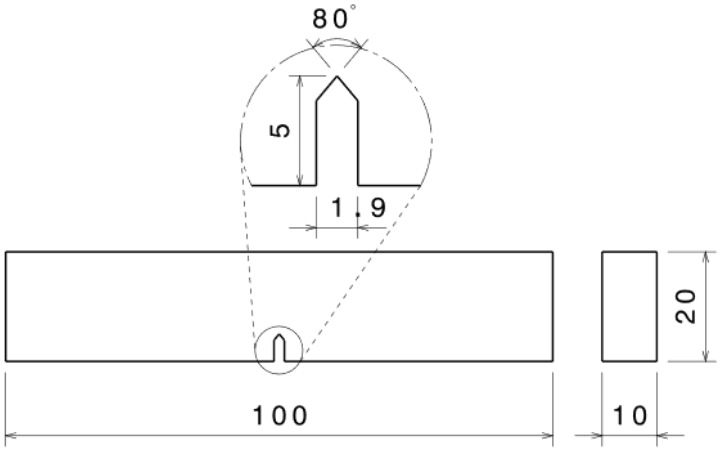

Figure 2.20. Dimensions, in mm, of fracture toughness specimens of the resin.

To measure the required energy to propagate the crack in the specimens during the experiment, there must be a natural crack tip generated before the tests. ASTM D5045 standard suggests that natural cracks can be induced by gently tapping on top of a razor blade positioned at the center of the notch section of the specimen. For valid tests, the total crack length, which is the summation of the notch length and the natural crack length, must be between 45-55% of the height of the specimen. However, the amount of natural crack propagation is proportional to the force applied to the razor blade, and it varies from person to person. Numerous specimens are sacrificed in this study during the razor tapping action to produce even a single specimen having a valid pre-crack length according to the ASTM standard. Therefore, it is very difficult to adjust the natural crack length in the specimens by

only applying tapping force to the razor blade. Tamura et al. have developed a pre-cracking technique in which they applied compressive stress in the transverse direction to compact tension specimens to prevent uncontrolled crack propagation while applying tensile load in the testing direction to initiate the cracking [44]. However, the circular contact area that they used for applying the transverse compressive stress resulted in a curved crack tip which is not suitable for toughness experiments. In a later study, compressive stress was applied with a rectangular contact area with the help of a toolmaker clamp, and they also examined the effect of the applied compressive load magnitude on the specimen [45]. Their study revealed that repeatable pre-cracking can be achieved in compact tension specimens for a certain transverse compressive load with an acceptable crack front shape. Based on these studies, a modified pre-cracking technique is developed in this study for creating the desired natural crack length in SENB specimens by applying transverse compressive load to the specimens before the razor tapping action. The compressive load is applied by a table mandrel, and to apply the load to the desired area without damaging the specimens, rectangular contact pads, with dimensions of 5mm x 5mm x 12mm, are manufactured through 3D printing from PLA. The pads are temporarily fixed to the sides of the SENB specimens by tape and their positions are determined such that the edge of the pad is within the allowed crack tip position specified by ASTM D5045. The pre-cracking setup is shown in Figure 2.21. After the pads are placed and the compressive load is applied by a table mandrel, the razor blade is placed at the center of the notch and a slight tapping force is applied at the top. Due to the applied load, a natural crack initiates and propagates suddenly until the edge of the contact pads where transverse compressive load constrains the further propagation of the crack tip. As a result, the desired initial crack length is obtained in a controlled manner without requiring high operator skill and sacrificing many specimens in the pre-cracking process.

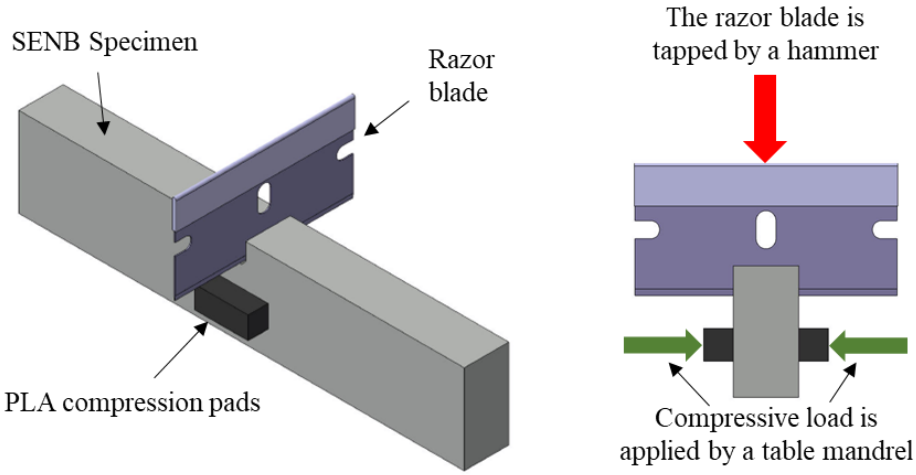

Figure 2.21. Pre-cracking setup proposed in this study for creating a desired natural crack length in SENB specimens.

2.4.2.2 Experimental Method

Tests are conducted following ASTM D5045 standard, and the setup is shown in Figure 2.22. SHIMADZU AGS-J servomechanical testing device with 10 kN load cell capacity is used. The diameter of the roller in the three-point bending fixture is 10mm, and the distance between the support rollers is set at 80 mm, which is four times the height of the specimens as stated in the standard. Tests are conducted under displacement control at a rate of 2.5mm/min. In addition to the pre-cracked specimens, one unnotched specimen is loaded above the maximum load observed in the tests of the pre-cracked specimens for calibration.

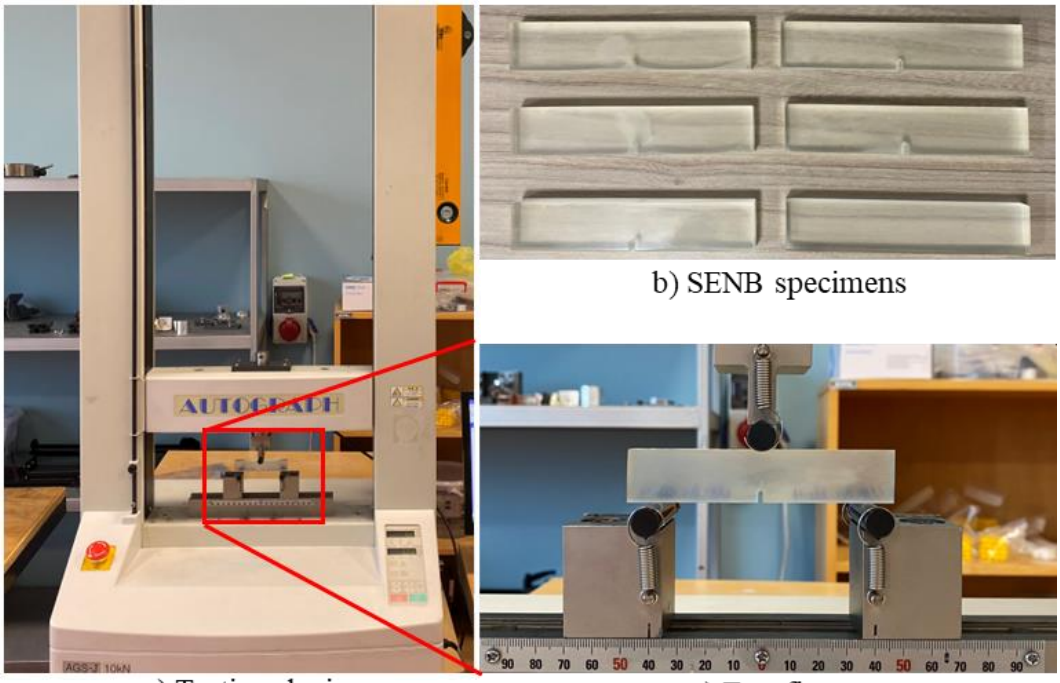

Figure 2.22. Experimental test setup used for obtaining the plane strain fracture toughness of the resin system with SENB specimens.

2.4.2.3 Results

Five pre-cracked and one unnotched specimens are tested. The unnotched specimen is used for the displacement correction to take the deformations of the specimen due to support contact regions into account. The load-displacement responses of the specimens are shown in Figure 2.23. For the SENB specimens, the reason for the initial stiffness difference is due to the variation in the initial crack length of the specimens, which directly affects the flexural stiffness. The plane strain fracture toughness of the CR80/CH80-6 resin system is calculated by using Equation (2.3).

$$(G_c)_{resin} = \frac{U}{BW\varphi} \tag{2.3}$$

where B and W is specimen thickness and depth, respectively. φ, energy calibration factor, depends on the crack length and its calculation is given in ASTM D5045. U in Equation (2.3) is the corrected energy and defined as:

$$U = U_Q - U_i \tag{2.4}$$

where U_Q is the area under load displacement curve of a SENB specimen, and U_i is the are under the load displacement curve of the unnotched beam. With these calculations for five specimens, plain strain fracture toughness of the resin system is obtained as $130.6\,J/m^2$ with the coefficient of variation 20.6%. Test results for individual specimens are provided in Appendix A. The variation in the results might be due to the crack opening procedure, where the suitable compressive stress is found by trial and error. Therefore, a more quantitative approach might be required while determining the amount of transverse compression in the pre-cracking process which may be investigated as a future study.

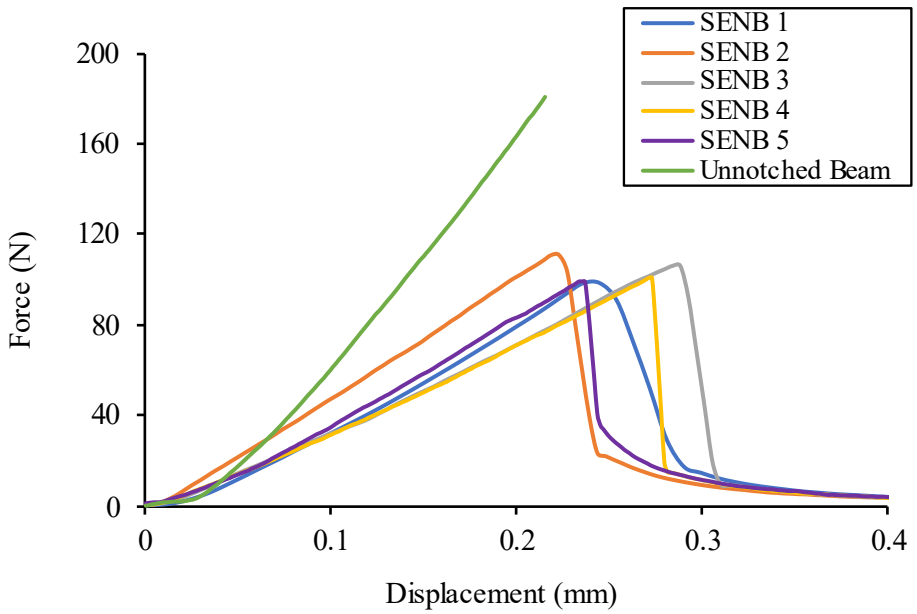

Figure 2.23. Load - displacement response of the unnotched beam and SENB specimens.

2.5 Dropped Ply Specimen Experiments

In this section, experimental procedure and results for single-stage ply drop-off specimen is reported. The main motivation of this study is to capture the delamination initiation and propagation in such structures.

2.5.1 Specimen preparation

Single-stage dropped ply specimens, illustrated in Figure 2.24, are manufactured by Odak Kompozit. Dropped, belt and core sub-laminates contain six 0° Interglass 92145 unidirectional glass fiber plies for each. The total specimen length and width are 250 mm and 25mm, respectively. In the manufacturing process, 6 core plies are laid on the flat tool surface. Then, dropped plies are glued to each other with a spray adhesive. Combined dropped plies are simultaneously cut using a ply cutter to ensure that the ply dropping locations for each dropped ply align precisely at the same point. Dropped sub-laminate is then placed on top of the core sub-laminate. This step is followed by the placement of the belt plies on top of dropped and core sub-laminates. The layup is covered with a vacuum bag, and the CR80/CH_6 resin system is combined with the glass fiber plies with the vacuum infusion technique. The composite layup is cured at room temperature for 24 hours, and then post-curing is performed at 80 $°C$ for 8 hours. The cured composite plate is sliced into specimens having dimensions of 250 mm x 25 mm with a water jet cutter. After the cutting process, grip tabs are attached to the specimens such that both ends have the same specimen thickness, and no additional bending is created on the specimens due to the gripping action.

After the manufacturing process, the side of the dropped ply specimens are polished with 400 to 2400 grit SiC sandpapers to be able to investigate the defects and voids created during the manufacturing process. Microscopic images of the specimens are taken with Huvitz HDS-5800 digital microscope, and evident voids are observed on

all specimens especially at the end of the dropped plies as shown in Figure 2.25. Therefore, the effect of void on delamination onset load and location must be investigated in numerical simulations. The dimensions of the specimens are measured with the digital microscope, and the average thickness of the thick section, the thin section, and the average taper angle are calculated as 2.96 mm, 1.99 mm, and 16.2°, respectively. After the measurement, the sides of the specimens are coated with a white paint to enhance the visibility of cracks during the testing.

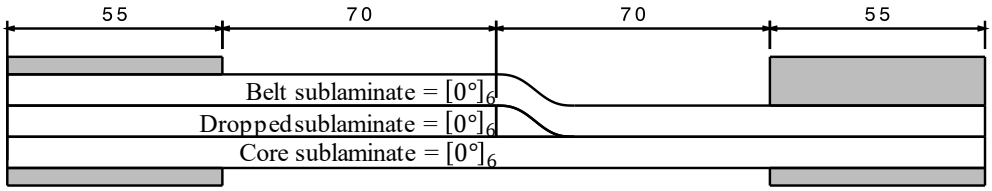

Figure 2.24. Illustration of the side view of dropped ply specimens investigated in this study.

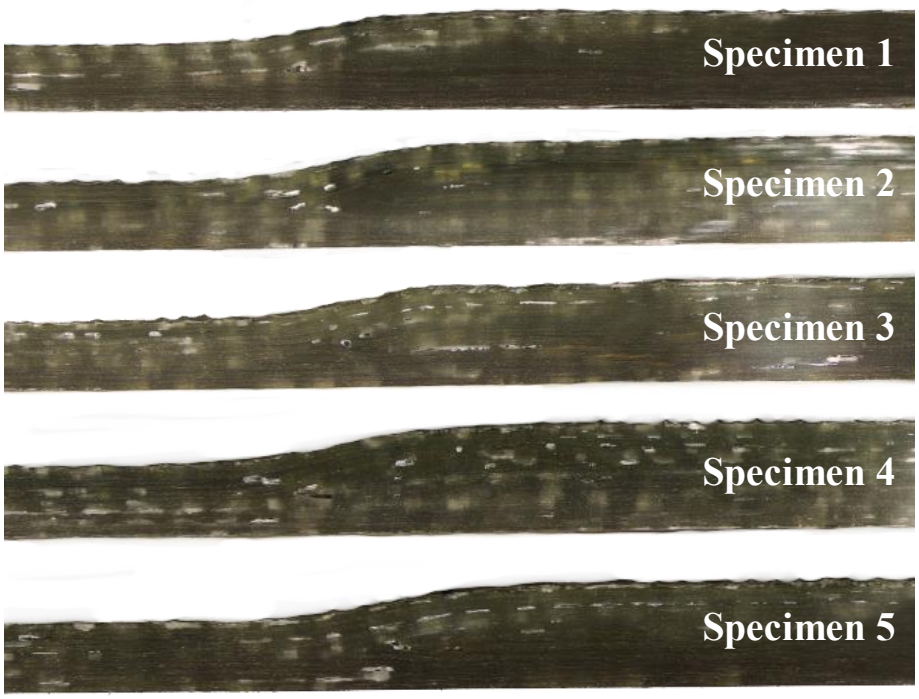

Figure 2.25. Microscopic images of dropped ply specimens.

2.5.2 Experimental Method

Single-stage dropped ply specimens are tested under tensile loading on a MTS servo-hydraulic testing machine with a 250 kN load cell capacity. The grip pressure of 12 MPa is used to hold the specimens. The dropped ply specimens are loaded with displacement control at a test rate of 0.5mm/min. The sides of the specimens are enlightened with two Dedocool COOLH lightening systems which are equipped with 250 W Osram HLX Tungsten lamps. Photron SA5 ultra high-speed camera is used in order to capture the failure event on one side of the drop-off regions. The recording speed of 50000 frames per second is found to be suitable for capturing the delamination initiation and propagation with a sufficiently large recording area. The high-speed camera is effective in capturing only sudden failure events since it is capable of recording the experiment for a couple of seconds when the trigger is activated. However, trial experiments with dropped ply specimens showed that slow crack propagation is observed before the sudden failure. Therefore, snapshots of the drop-off region with 5 seconds intervals during the test are also taken to match the slow delamination propagation time with load displacement data.

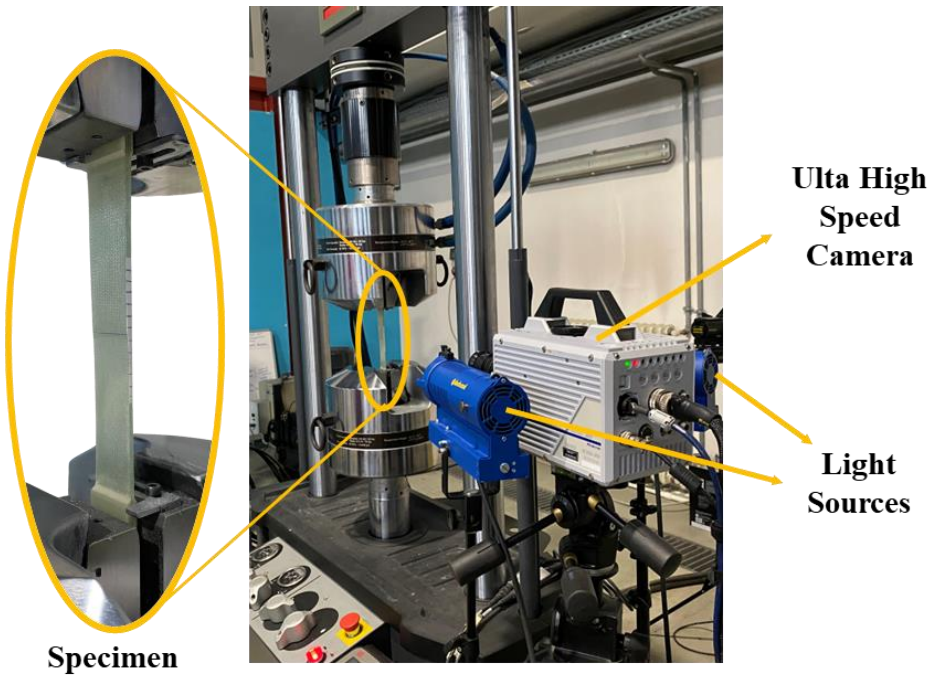

Figure 2.26. Test setup for dropped ply tension experiments.

2.5.3 Results and Discussion

A total of five dropped ply specimens underwent tensile loading, and high-speed photography captured the sides of all specimens during the testing process. No sign of sliding at the taps of the specimens is observed, indicating that enough grip pressure for this specimen configuration is achieved. As an example, the failure sequence for specimen 1 is given in Figure 2.27, and load-displacement response for the same specimen is given in Figure 2.28. As the specimen is loaded, initially curved belt plies start to straighten out under tensile loading. This leads to the thin section delamination, which is the separation of the belt and the core ply interface at the tip of the resin pocket as shown in Figure 2.27. The thin section crack initiates slowly; therefore, snapshots taken at 5 seconds intervals are sufficient to capture the delamination onset and propagation. The initiation of thin section delamination causes only a small amount of load drop in the load-displacement curve in Figure 2.28 because as the delamination propagates towards the thin section, both core and belt plies continue to carry the load. As there is no significant loss of stiffness observed in thin section delamination, a noticeable load drop is not observed in the load-displacement curve.

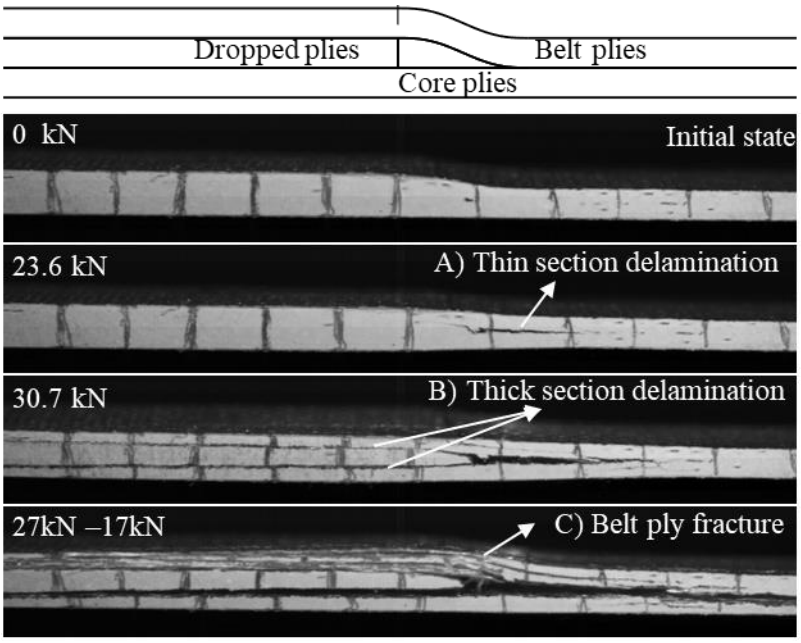

Figure 2.27. Failure sequence of the dropped ply specimen 1.

As the specimen is loaded further and the tensile load reaches 30.7 kN, two cracks initiate at the upper and lower interface of the dropped plies at the ply drop-off region, and these cracks suddenly propagate towards the thick section of the laminate, resulting in the thick section delamination as shown in Figure 2.27. Separation of the dropped sub-laminate from the core and the belt sub-laminates due to the thick section delamination causes a significant reduction of stiffness in the specimen. Therefore, a sudden load drop is observed in the load-displacement curve as shown in Figure 2.28 when the thick section delamination occurs.

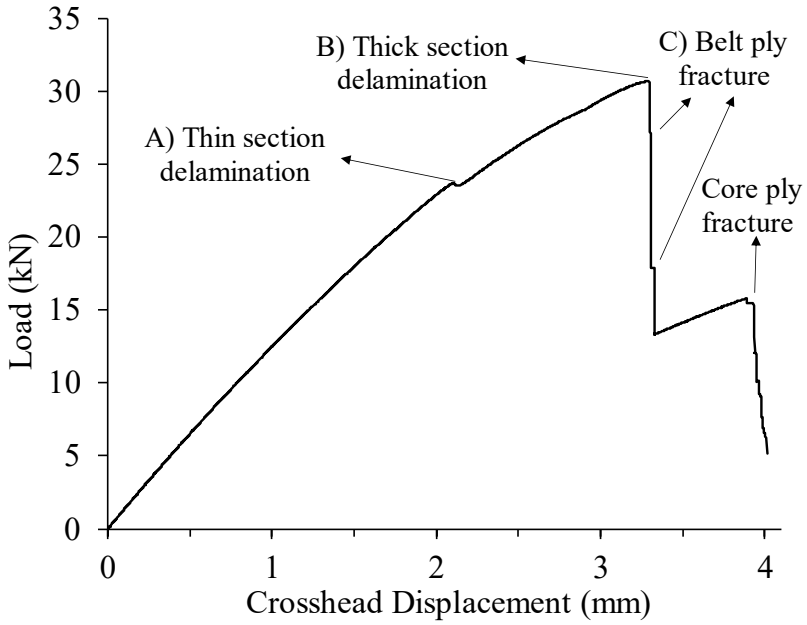

Figure 2.28. Load-displacement response of specimen 1 under tensile loading.

Since the thick section delamination initiates and propagates suddenly, it is only possible to capture the delamination evolution with a high-speed photography. Propagation stages of the thick section delamination recorded with the high-speed camera are given in Figure 2.29. The crack at the lower interface of the dropped sub-laminate initiates earlier than the one on the upper interface. The two parallel cracks propagate towards the taps of the specimen while maintaining the initial distance between them. The main reason for the initiation time difference between the two crack tips is the asymmetry of the dropped ply specimens.

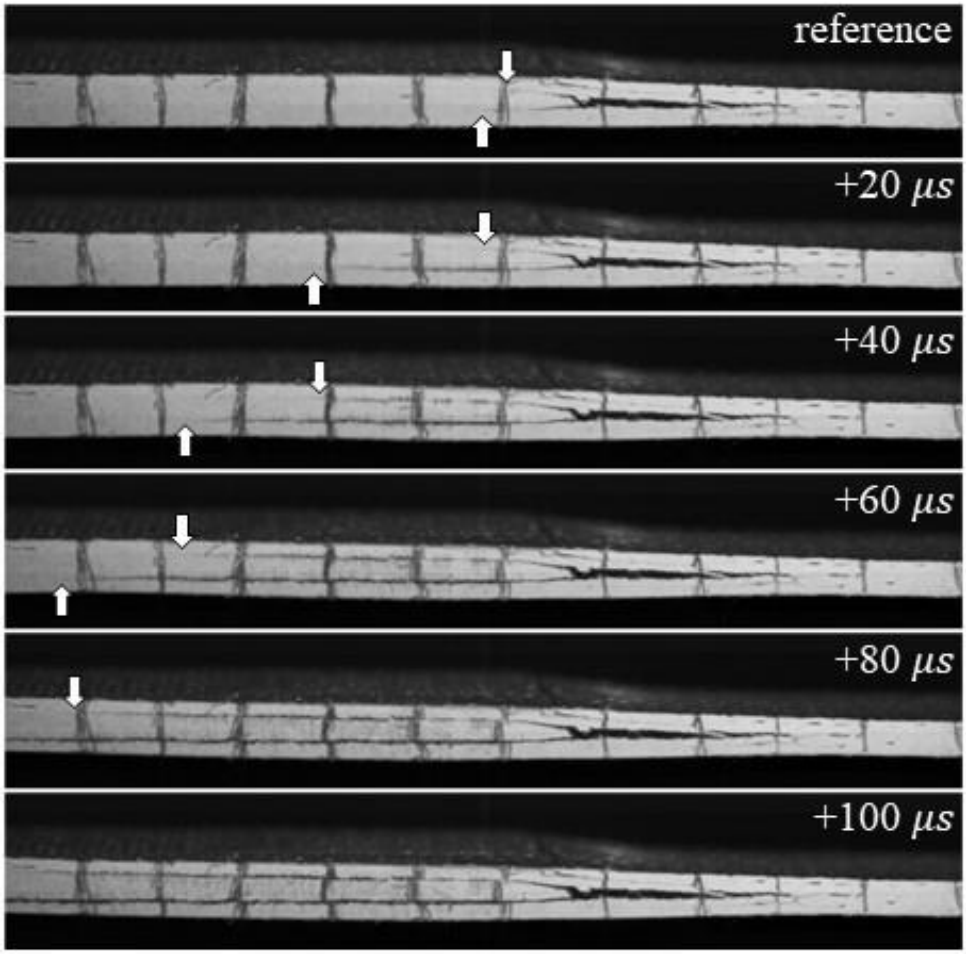

Figure 2.29. Thick section delamination progress for specimen 1 at 30.7 kN

Thin Section Delamination

The thin section delamination is observed in all five specimens prior to fiber fracture and before the thick section delamination. Thin section delamination onset loads and stages for all specimens are shown in Figure 2.30. The average thin section delamination onset load for five dropped ply specimens is calculated as 24.01 kN with a coefficient of variation of 10.7%. Since the thin section delamination does not significantly degrade the stiffness of the laminate, either no load drop or small load drop is observed at the onset of thin section delamination for all specimens. Therefore, it is necessary to take snapshots of the specimen at certain intervals to capture the stage corresponding to the thin-section delamination onset.

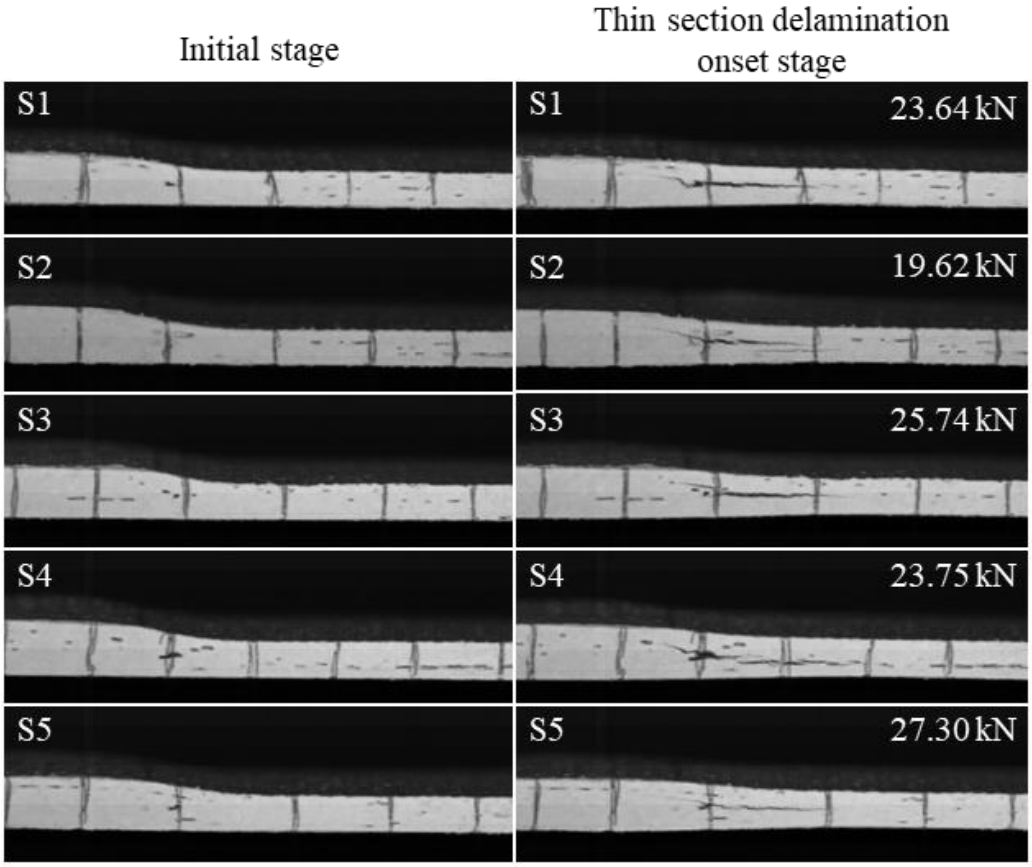

Figure 2.30. Thin section delamination stages and thin section delamination onset loads for all dropped ply specimens.

Thick Section Delamination

After the initiation of thin-section delamination, the specimens are loaded further, and thick-section delamination is observed. The thick section delamination onset stages and loads for all specimens are shown in Figure 2.31. Owing to the high stiffness degradation after the separation of the dropped sub-laminate from the core and the belt sub-laminate, the thick section delamination creates a significant load drop in the load-displacement response. Even though the thick section delamination is the second failure mode observed in the majority of the specimens tested in this study, fiber fracture is also observed before the thick section delamination in some specimens. For example, although double-thick section cracks are visible on the front face of specimen 2, fiber fracture occurred at the back face of the specimen.

Additionally, a visible belt ply fracture occurred at the front face of specimen 3, and this failure triggered a single thick section crack at the lower interface of the dropped plies. This single crack suddenly propagated towards the taps at the thick section. Therefore, for specimens 2 and 3, thick section delamination onset load cannot be considered. However, in specimens 1, 4, and 5, the thick section delamination occurred following the thin section delamination and before the fiber fracture. The average thick section delamination onset load is calculated as 30.14 kN with a 6.0% coefficient of variation by considering only specimens 1, 4, and 5.

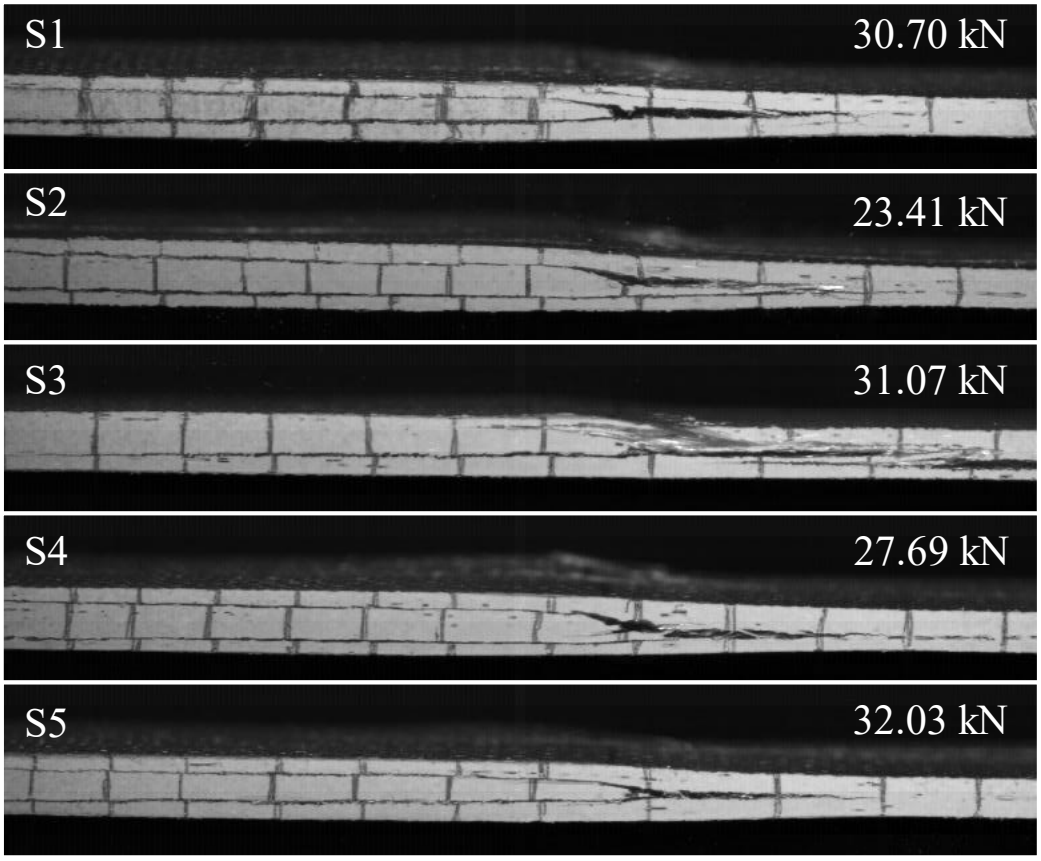

Figure 2.31. Stages after the thick section delamination and load levels corresponding to the onset of thick section delamination for all dropped ply specimens.

2.6 Chapter Conclusion

In this chapter, the material characterization of Interglass 92145/CR80 composite material and CR80/CH80-6 epoxy/hardener resin system are performed. The manufacturing process of pure resin tension and fracture toughness specimens by using the resin casting method is presented. A practical approach to creating a natural crack in single-edge notched beam specimens is proposed. Standard tension, ILSS, DCB, and ENF tests are performed to obtain elastic and interlaminar properties of the composite material. An experimental investigation study of dropped ply specimens is also performed under tensile loading with high-speed photography to understand the failure mechanism and corresponding load levels in specimens with internal ply terminations.

- The proposed method to create controlled pre-cracking for SENB specimens by applying a transverse compression load showed promising results in creating the desired crack length without compromising a substantial number of specimens during the preparation phase.

- The experiments with tapered specimens revealed the different characteristics of thin section and thick section delaminations. Notably, thin section cracks exhibited slow propagation without causing significant softening in the load-displacement response. In contrast, thick section delamination showed abrupt propagation, leading to a noteworthy loss of stiffness in the investigated specimens within the scope of this study.

The experimental study conducted in this chapter provided essential material properties that can be used in the numerical analysis of laminates with ply drop-off regions. Furthermore, the documented onset loads for thin-section and thick-section delamination in this chapter will serve as valuable data for the verification study of the finite element models.

CHAPTER 3

NUMERICAL INVESTIGATION OF COMPOSITE LAMINATE WITH A SINGLE-STAGE PLY DROP-OFF

3.1 Introduction

In this chapter, the development of the finite element model for predicting the delamination in laminates with ply drop-offs and simulation of dropped ply experiments documented in Chapter 2 are performed. The effects of taper angle and material properties on delamination initiation and location are also investigated.

3.2 Numerical Method

Since the use of high-fidelity finite element models for the delamination prediction showed good alignment with the experimental results [2,30,46], detailed finite element models are developed in this section to predict the delamination onset load in tapered laminates.

3.2.1 Interface Damage Model

Due to the combination of weak bonding between layers and high interlaminar stresses arising around the ply drop-off regions, delamination becomes the main failure mode in tapered laminates. There are both strength-based and fracture mechanics based approaches to predict the delamination onset in ply termination regions. While strength-based approaches can give conservative results, fracture based approaches require the initial crack position to be known. Besides, both delamination initiation and propagation is considered with the cohesive zone

modeling technique which brings the strength based and fracture based approaches together. Therefore, the cohesive zone modeling technique is used in the current study for delamination prediction.

3.2.1.1 Cohesive Zone Modeling

The cohesive zone modeling technique is widely used in delamination analysis in laminated composite structures, especially when weak interlaminar bonding between layers forms predetermined crack paths. The constitutive formulation of the cohesive elements establishes a relationship between interlaminar tractions and relative displacement, also called the separation, of the nodes connected with these cohesive elements.

Cohesive elements provided in ABAQUS are utilized in delamination analysis in this study, and their detailed formulation is given in Ref. [47]. Constitutive responses of the elements are defined by a bi-linear traction separation relation, as depicted in Figure 3.1. While τ_k indicates traction in k direction, τ_k^0 represents the interlaminar strength, and k takes the value of n, s, and st for normal, first shear, and second shear directions, respectively. Current separation, final separation, and the separation corresponding to maximum traction are denoted as δ_k, δ_k^f, and δ_k^0, respectively. The area beneath the traction separation curve corresponds to the fracture toughness of the interface, denoted as G_{ic}. i takes the values of I, II, and III depending on the fracture mode.

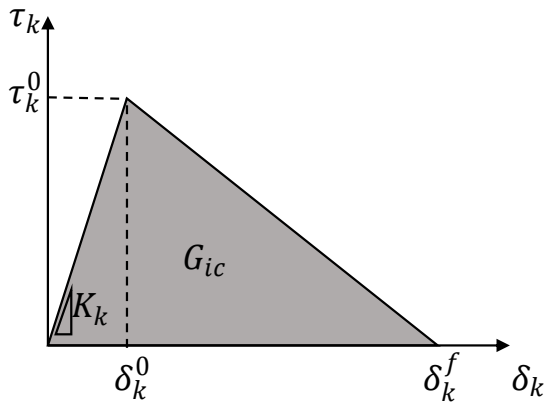

Figure 3.1. Bilinear traction separation based constitutive response of cohesive elements.

The initial slope of the traction separation curve, denoted as K_k, is defined as the penalty stiffness. Once the current separation reaches the separation corresponding to the interlaminar strength of the material, damage initiation occurs. The displacements corresponding to the maximum traction can be calculated by using the penalty stiffness values as follows:

$$\delta_k^0 = \tau_k^0 / K_k \text{ for } k = n, s, st \tag{3.1}$$

The traction on the element before and after damage initiation is then determined as follows:

$$\tau_k = \begin{cases} \delta_k K_k & for\ d_k = 0 \\ \delta_k K_k (1 - d_k) & for\ d_k > 0 \end{cases} \quad k = n, s, st \tag{3.2}$$

where d_k represents the damage parameter and is calculated as:

$$d_k = \frac{\delta_k^f (\delta_k - \delta_k^0)}{\delta_k \left(\delta_k^f - \delta_k^0\right)} \tag{3.3}$$

The value of the damage parameter, d_k, is initially 0 prior to the initiation of damage and becomes 1 when the current separation, δ_k, reaches the final separation, δ_k^f. The

final separation where traction on the element becomes zero can be calculated by using the critical strain energy release rates of the laminate:

$$\begin{aligned} \delta_n^f &= 2G_{Ic}/\tau_n^0 \\ \delta_s^f &= 2G_{IIc}/\tau_s^0 \\ \delta_{st}^f &= 2G_{IIIc}/\tau_{st}^0 \end{aligned} \tag{3.4}$$

Since the traction–relative displacement response is defined, energy release rates in all three directions can be computed by integrating the traction separation curve until the current displacement as shown in Equations (3.5) :

$$\begin{aligned} G_I &= \int_0^{\delta_n} \tau_n d\delta_n \\ G_{II} &= \int_0^{\delta_s} \tau_s d\delta_s \\ G_{III} &= \int_0^{\delta_{st}} \tau_{st} d\delta_{st} \end{aligned} \tag{3.5}$$

Mixed-Mode Loading Condition

In numerous applications, delamination occurs under combined loading scenarios rather than a pure mode condition. Therefore, the interaction of the loading modes must be taken into account in the formulation of the cohesive zone method. In the context of mixed mode analysis, effective traction (τ_{ef}) – effective separation (δ_{ef}) is used in order to define the mixed mode constitutive response of the cohesive elements, as depicted in Figure 3.2(a). The effective separation is defined as $\delta_{ef} = \sqrt{\delta_n^2 + \delta_{shear}^2}$ where $\delta_{shear} = \sqrt{\delta_s^2 + \delta_{st}^2}$ is the combined shear separation. The area under the effective traction – effective separation curve gives the total critical energy release rate, G_{Tc}, and total energy release rate is defined as $G_T = G_I + G_{II} + G_{III}$. The relation between mixed mode bilinear traction separation curve with shear and opening traction separation curves is illustrated in Figure 3.2(b).

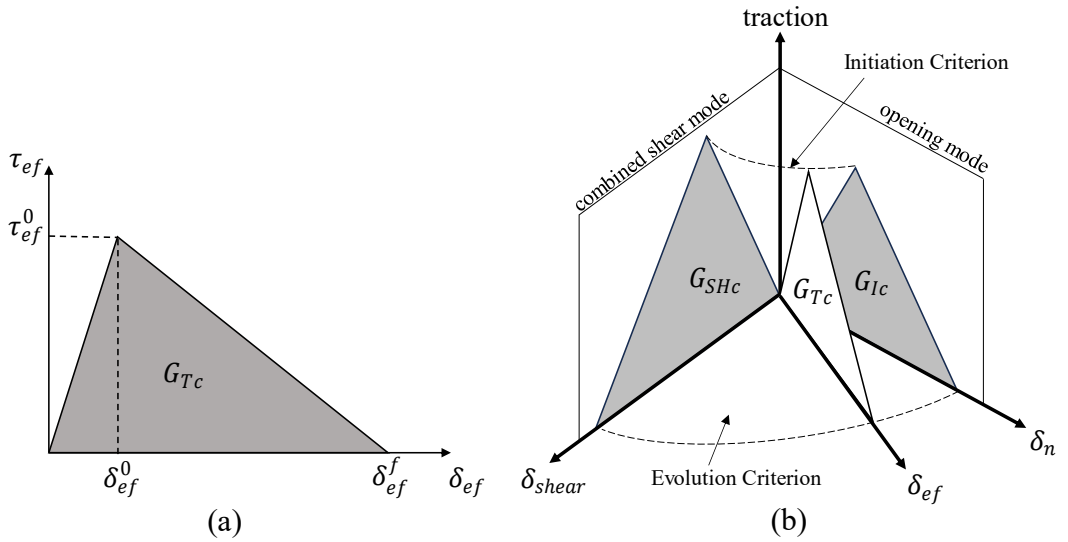

Figure 3.2. (a) Effective traction – effective separation curve used for mixed-mode response of cohesive elements, (b) Mixed mode traction separation response illustration of cohesive elements with mixed mode initiation and propagation criteria.

To obtain the effective displacement corresponding to the damage initiation in mixed mode loading condition, the following stress based quadratic damage initiation criteria, proposed by Brewer and Lagace [48], is employed.

$$\left\{\frac{\langle\tau_n\rangle}{\tau_n^0}\right\}^2 + \left\{\frac{\tau_s}{\tau_s^0}\right\}^2 + \left\{\frac{\tau_{st}}{\tau_{st}^0}\right\}^2 = 1 \tag{3.6}$$

Macaulay operator is applied to τ_n since compressive stress does not induce interface damage. The stress-based initiation criterion given in Equation (3.6) is converted into displacement-based criteria by substituting Equation (3.1) and (3.2) into Equation (3.6). As a result, the displacement corresponding to the initiation of mixed mode damage, δ_{ef}^0, can be computed. After the initiation of damage, softening starts, and effective traction becomes zero when the effective separation reaches the final effective separation, δ_{ef}^f. Effective final separation can be calculated by using the area under the traction separation curve as follows:

$$\delta_{ef}^{f} = 2G_{Tc}/\tau_{ef}^{0} \tag{3.7}$$

To calculate the mixed mode critical energy release rate, G_{Tc}, the energy-based mixed mode criterion, as presented in Equation (3.8), is employed in this study. This criterion is proposed by Benzeggagh and Kenane to take the mode mixity in delamination evolution into account [49].

$$G_{Tc} = G_{Ic} + (G_{SHc} - G_{Ic})\left(\frac{G_{SH}}{G_T}\right)^{\eta} \tag{3.8}$$

In Equation (3.8), G_{SH} represents the summation of energy release rates in the first and the second shear directions ($G_{II} + G_{III}$). G_{Tc}, G_{Ic}, and G_{SHc} are critical total, critical opening, and critical combined shear energy release rates, respectively. The parameter η is an empirical mixed mode parameter that depends on the material. After δ_{ef}^{0} is reached, the mixed mode damage in the elements is defined as:

$$d = \frac{\delta_{ef}^{f}\left(\delta_{ef} - \delta_{ef}^{0}\right)}{\delta_{ef}\left(\delta_{ef}^{f} - \delta_{ef}^{0}\right)} \tag{3.9}$$

3.2.1.2 Enhancement of interface properties

Several experimental studies demonstrated that shear strength and mode II fracture toughness of laminated composite materials increase in the presence of compressive stresses [31–35]. This phenomenon becomes particularly critical in the analysis of ply drop-offs due to the combined shear and compressive stresses at the end of the dropped plies. Neglecting the enhancement effect can lead to a conservative prediction of the delamination initiation load. However, cohesive elements provided by ABAQUS do not incorporate the enhancement of the interface properties with compressive stress. In other words, compression does not affect the response of the cohesive elements.

The improvement effect of interlaminar shear strength and mode II fracture toughness of the laminates is taken into account through the utilization of custom interface elements in Ref. [37]. These specialized interface elements exhibit a modified traction separation response depending on the compressive stress state of the elements, as illustrated in Figure 3.3.

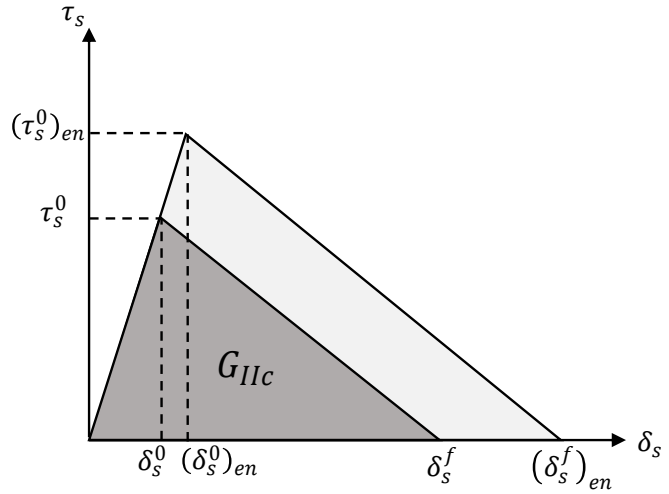

Figure 3.3. Illustration of the enhancement of the shear strength and mode II fracture toughness of the interface elements with the presence of compression.

Parameters in the figure with subscript "en" indicate the enhanced properties due to compression. Various enhancement relations are investigated in Ref. [37] on diverse specimens in which delamination initiation interfaces are subjected to combined shear and compressive stresses. These specimens include a dropped ply, a single lap shear, and cut ply specimens. The findings of the study revealed that the best enhancement relation is achieved for all investigated specimen configurations when the enhanced softening curve of the traction separation response aligns in parallel with the softening curve of the original traction separation response. The enhancement relations employed by Li et al. [37] to consider the shear strength and mode II fracture toughness due to compression are provided in Equations (3.10) and (3.11).

$$(\tau_s^0)_{en} = \tau_s^0 + \eta_f \langle -\tau_n \rangle \tag{3.10}$$

$$(G_{IIc})_{en} = G_{IIc}\left(\frac{(\tau_s^0)_{en}}{\tau_s^0}\right)^2 \tag{3.11}$$

where τ_s^0 is the interlaminar shear strength, and τ_n is the traction in the normal direction. The coefficient η_f is the enhancement factor analogous to the internal friction and depends on the material. The value of $\langle -\tau_n \rangle$ in Equation (3.10) becomes positive and nonzero only in the presence of compressive stress on the interface. In that case, shear strength and mode II fracture toughness increase. Otherwise, no enhancement occurs in the absence of compression. That is, $(\tau_s^0)_{en} = \tau_s^0$ and $(G_{IIc})_{en} = G_{IIc}$.

Utilization of custom cohesive elements has challenges in terms of time requirement and complexity during development, whereas built-in cohesive elements are readily available for use. Therefore, enhancement of the interface properties due to compression is taken into account by using the user-defined field variable subroutine (USDFLD) of ABAQUS/Standard in this study. The subroutine enables users to modify the material properties of the elements based on the specified field variables, such as temperature, strain, or stress components. Therefore, depending on the compressive stress on the cohesive elements, fracture toughness, and interlaminar shear strength values can be updated during the simulation.

The procedure is straightforward in comparison to the development of custom interface elements. Interlaminar shear strength and fracture toughness values are computed by using Equations (3.10) and (3.11) for different values of compressive stresses. The list of interface properties for various values of compression are tabulated in the material property section, with compressive stress defined as a field variable. The material property tables are shown in Table 3.1 and Table 3.2.

Table 3.1. Cohesive strength values depending on compressive stress.

Normal Strength	Shear Strength First direction	Shear Strength Second direction	Field Variable $\boldsymbol{\tau_n}(\mathbf{MPa})$
$\boldsymbol{\tau_n^0}$	$\boldsymbol{\tau_s^0}$	$\boldsymbol{\tau_{st}^0}$	0.0
$\boldsymbol{\tau_n^0}$	$(\boldsymbol{\tau_s^0})_{en}$	$(\boldsymbol{\tau_{st}^0})_{en}$	-1.0
...	...	...	...
$\boldsymbol{\tau_n^0}$	$(\boldsymbol{\tau_s^0})_{en}$	$(\boldsymbol{\tau_{st}^0})_{en}$	-300.0

Table 3.2. Cohesive fracture toughness values depending on compressive stress.

Normal Mode Fracture Energy	Shear Mode Fracture Energy First direction	Shear Mode Fracture Energy Second direction	Field Variable $\boldsymbol{\tau_n}(\mathbf{MPa})$
$\boldsymbol{G_{Ic}}$	$\boldsymbol{G_{IIc}}$	$\boldsymbol{G_{IIIc}}$	0.0
$\boldsymbol{G_{Ic}}$	$(\boldsymbol{G_{IIc}})_{en}$	$(\boldsymbol{G_{IIIc}})_{en}$	-1.0
...	...	...	...
$\boldsymbol{G_{Ic}}$	$(\boldsymbol{G_{IIc}})_{en}$	$(\boldsymbol{G_{IIIc}})_{en}$	-300.0

The only operation performed in the USDFLD subroutine is that the stress tensor from the previous time increment in cohesive elements is retrieved using the GETVRM subroutine, and the normal component of the stress tensor is defined as the field variable. ABAQUS then performs interpolation of the material properties between tabulated ones based on the value of the field variable, which, in this case, is the compressive stress. The interpolation of the material properties between tabulated values for fracture toughness is illustrated in Figure 3.4. It is important to note that ABAQUS does not perform extrapolation of the material properties. In other words, when the normal stress at a material point becomes positive, tabulated material properties corresponding to zero compressive stress are used by the solver. This implies that no enhancement occurs when the normal stress is tensile. Moreover, enhanced shear strength and Mode II fracture toughness of the elements are kept constant after the damage occurs in the elements to prevent the change of constitutive response of the cohesive elements in the softening region as stated in Ref. [35].

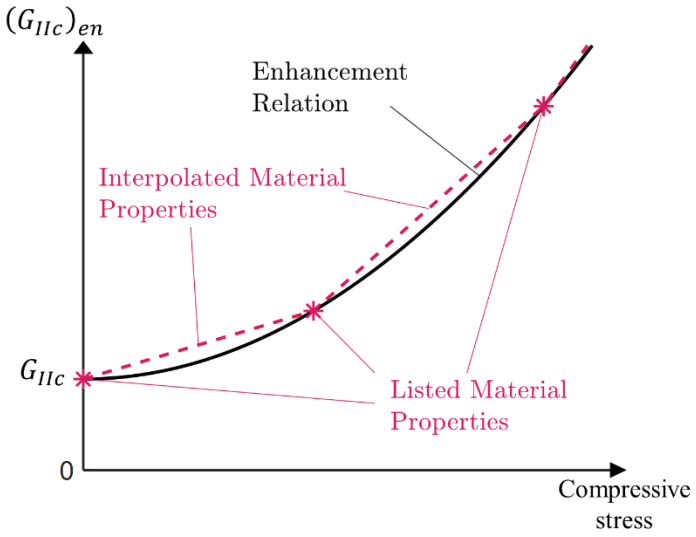

Figure 3.4. Interpolation of the fracture toughness properties.

Contact Clearance Definition

Cohesive elements with either finite thickness or zero thickness can be implemented into the delamination surfaces in a model. However, the implementation of cohesive elements with a finite thickness becomes challenging for complex geometries, especially in cases where more than one delamination surface intersects at a single point, such as the corner points of the triangle resin pocket in dropped ply models. Therefore, it is more suitable to utilize zero-thickness cohesive elements in the analysis of tapered laminates with dropped plies. However, when considering the enhancement of interlaminar properties due to compression, the contact algorithm used to prevent the penetration of crack surfaces into each other can lead to a problem. Both cohesive elements and the contact algorithm prevent the penetration of the adjacent solid elements when the interface is subjected to compression. In such cases, compressive load is distributed between cohesive elements and contact stiffness. This is illustrated in Figure 3.5(a) with a spring analogy. The decomposition of the interface load between cohesive elements and the contact algorithm causes cohesive elements to experience a lower magnitude of compressive stress compared to the actual compressive stress on the interface. In most cases, this does not cause a problem in delamination analysis with cohesive elements because the compressive stress experienced by the cohesive elements does not influence the

damage initiation and propagation calculations. However, since the enhancement of the interlaminar properties in Equations (3.10) and (3.11) is calculated according to the compressive stress on the cohesive elements, defining normal contact with zero-thickness cohesive elements becomes problematic in the analysis of tapered laminates when compression-induced enhancement is taken into account. To overcome this problem, a clearance is defined in the contact algorithm, as depicted in Figure 3.5(b), to allow cohesive elements to solely carry the compressive load until they fail completely.

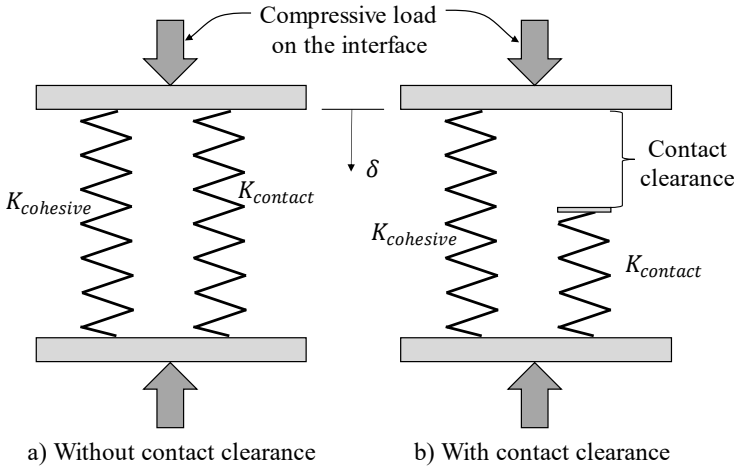

Figure 3.5. Spring analogy for the interface a) without contact clearance and b) with contact clearance.

However, selecting the suitable clearance value for the analysis is critical. A small contact clearance might not allow sufficient room for the interface elements to deform, whereas a large value could fail to accurately simulate the actual interaction of the crack surfaces after delamination. Therefore, a reasonable value for the contact clearance can be decided by considering the maximum compressive stress observed in cohesive elements during the simulation. This stress value can be used to calculate the required deformation for the elements to reach that stress level. As a result, this deformation value can be used as the minimum contact clearance required in the simulation. Equation (3.12) can be used for the calculation of the minimum required contact clearance,

$$\delta_{min} = \frac{\sigma_{c_{max}}}{K_n} \tag{3.12}$$

where K_n is stiffness of the cohesive elements in the normal direction, $\sigma_{c_{max}}$ is the magnitude of the maximum compressive stress that exists in the interface, and δ_{min} is the minimum required deformation of the cohesive element in normal direction under compression to experience $\sigma_{c_{max}}$. Hence, the contact clearance must be larger than δ_{min} to accurately take into account the compression-induced enhancement of the interlaminar properties of the laminate with zero thickness cohesive elements.

3.2.1.3 Verification of the Interface Damage Model

In this study, the constitutive response of the built-in cohesive elements in ABAQUS is manipulated by using the user-defined subroutine (USDFLD) to take into account the improvement of the interlaminar strength and toughness properties under compression. Therefore, the verification study for the subroutine must be performed. In the subsequent section, the traction-separation response of a single cohesive element under different compressive loads is investigated. Furthermore, a more complex experimental setup in the literature is simulated to demonstrate how USDFLD aligns with the behavior of a custom interface element, developed in VUEL subroutine.

Verification Study on a Single Cohesive Element

Verification of the user subroutine is performed on a two-dimensional cohesive element (COH2D4) with an element size of 0.1mm x 0.1 mm. Boundary conditions and analysis steps are illustrated in Figure 3.6. The displacements of the bottom nodes in the y direction are constrained, and to fix the model in space, one of the bottom nodes is also constrained in x direction.

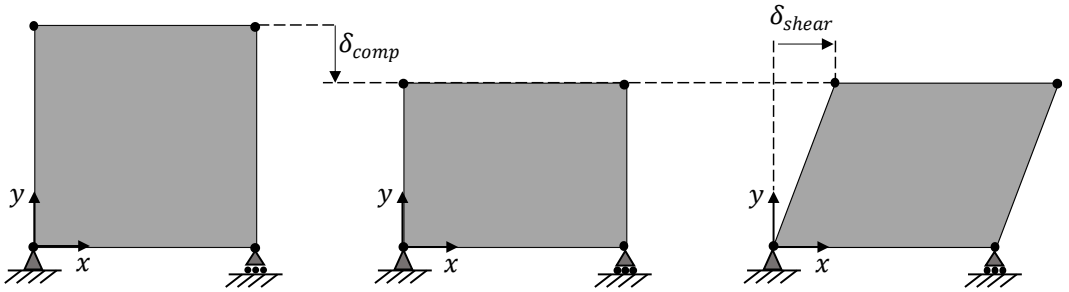

a) Initial condition b) The first step c) The second step

Figure 3.6. Boundary conditions of the finite element model and analysis steps for verification of the subroutine on a single cohesive element in ABAQUS.

In order to induce a desired compressive stress, $(\tau_n)_{desired}$, on the element to test the shear response under different compressive stresses, a compressive displacement, denoted as δ_{comp}, is applied to the upper nodes in the negative y direction. The magnitude of displacement is determined based on the stiffness of the cohesive element in the normal direction as shown in Equation (3.13).

$$\delta_{comp} = \frac{-(\tau_n)_{desired}}{K_n} \tag{3.13}$$

In the second step of the simulation, shear displacement in the x direction is applied until the cohesive element fails completely meanwhile the compressive displacement applied in the first step is kept at the same value. In this way, the traction separation response of the cohesive element in the shear direction can be examined under varying levels of compressive stress. The cohesive element properties used in the verification studies are taken from Ref. [33] and listed in Table 3.3.

Table 3.3. Cohesive element properties used in the verification study [33].

G_{Ic} (N/mm)	$G_{IIc} = G_{IIIc}$ (N/mm)	τ_n^0 (MPa)	$\tau_s^0 = \tau_{st}^0$ (MPa)	K_n (N/mm^3)	$K_s = K_{st}$ (N/mm^3)	η_f
0.2	1.0	60	82.6	4.67e5	1.67e5	0.3

The parameter η_f in Table 3.3 is the enhancement coefficient explained in the previous section and the value of 0.3 is also taken from Ref. [33] for the same interface properties. The shear traction response of the cohesive element with user subroutine for varying values of the compressive stress state is given in Figure 3.7. The only parameter changed in these simulations is the magnitude of compressive displacement applied to the upper nodes of the cohesive element at the first analysis step. The observed increase in both the maximum shear traction and area under the traction separation curve with increasing compressive stress indicates the enhancement of the interface properties. These results demonstrate the successful functioning of the user subroutine developed in this study.

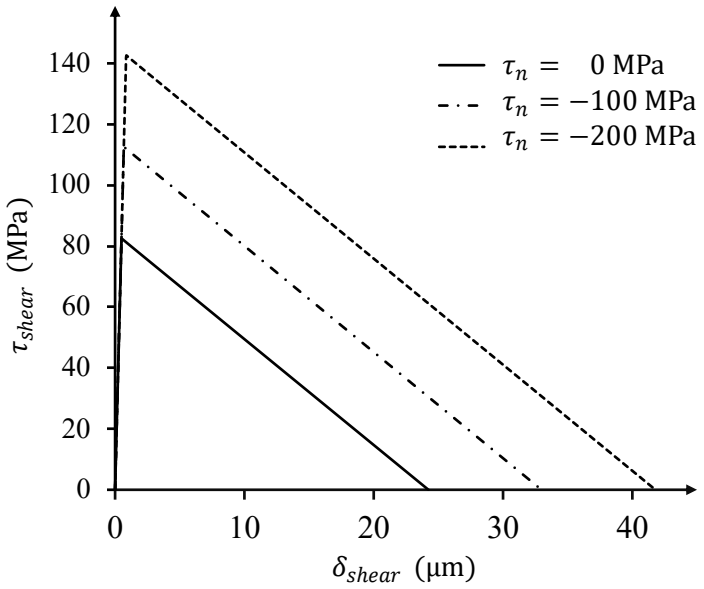

Figure 3.7. Traction-separation response of single cohesive element in shear direction with the user subroutine under different compressive stress values.

Symmetric Double-Notched Specimen Simulation

The subroutine developed in this study is verified on a single cohesive element with a finite thickness in the previous section. In this section, verification of the subroutine for zero-thickness cohesive elements in a composite specimen is performed. Gan et al.[33] proposed a symmetrical double-notch specimen (DNS) to measure the enhancement of the shear strength of a composite laminate under transverse

compression. The test setup and specimen dimensions are illustrated in Figure 3.8. The specimens are manufactured from IM/8552 carbon epoxy unidirectional pre-preg material. Even though two different configurations are tested in the reference study, only configuration A having $[(0/90)_5/0_3/(0/90)_5]_s$ layup is considered in this study. Each ply has a thickness of 0.125 mm. The notch depth is equal to a quarter of the total specimen thickness, 1.4375 mm. The test is conducted using a biaxial testing machine. Initially, a transverse compressive load P is applied to the specimen with steel indenters. Once the compressive load reaches its equilibrium state, the specimen is pulled with displacement control until the final failure along the two shear planes occurs. Response of the user-defined zero-thickness interface elements developed in VUEL subroutine is compared with the experimental results in Ref. [33]. The purpose of this section is to compare the response of the cohesive elements with the subroutine (USDFLD), developed in this study, with a more complex subroutine (VUEL), used in the reference study.

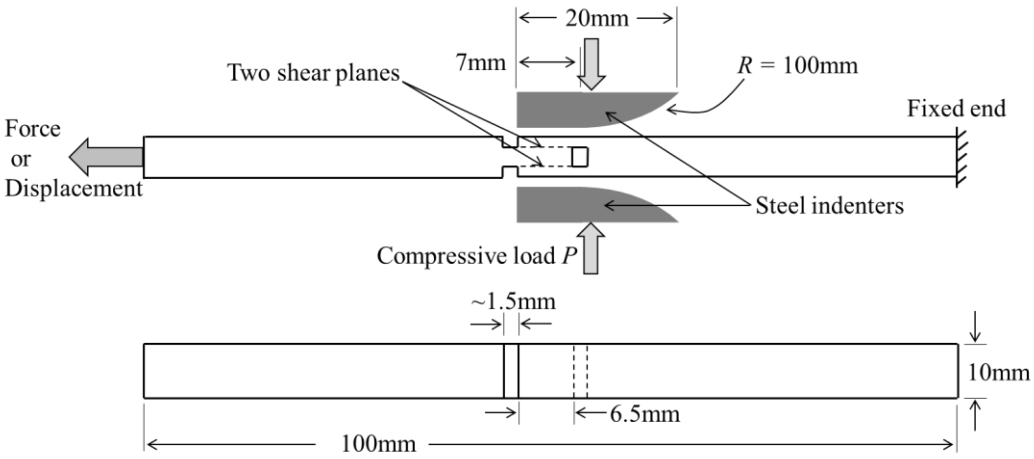

Figure 3.8: Symmetrical double notch shear specimen test setup from Ref. [33].

Finite element model of the specimen, depicted in Figure 3.8, is created in ABAQUS with Dynamic Implicit solver as shown in Figure 3.9. For computational efficiency, only the upper half of the specimen is modeled, considering the symmetry of the test setup. Symmetry boundary condition is applied at the midplane of the specimen, as shown in Figure 3.9. 2D plane strain elements are employed since the variation of the stress in the width direction is negligible for this particular problem. Steel

indenter is modeled as an isotropic material with properties of Poisson's ratio of $\nu = 0.3$ and Young's modulus of $E = 210$ GPa. The movement of the indenter is constrained only in the horizontal direction, and load is applied at the top surface of the indenter. Frictionless contact is defined between the composite specimen and the steel indenter. The right-hand side of the specimen is fixed. In the first analysis step, a compressive load is applied to the steel indenter. This compressive load on the indenter is maintained constant throughout the simulation. Then, in the second analysis step, a prescribed displacement is applied to the left-hand side of the composite specimen until failure occurs.

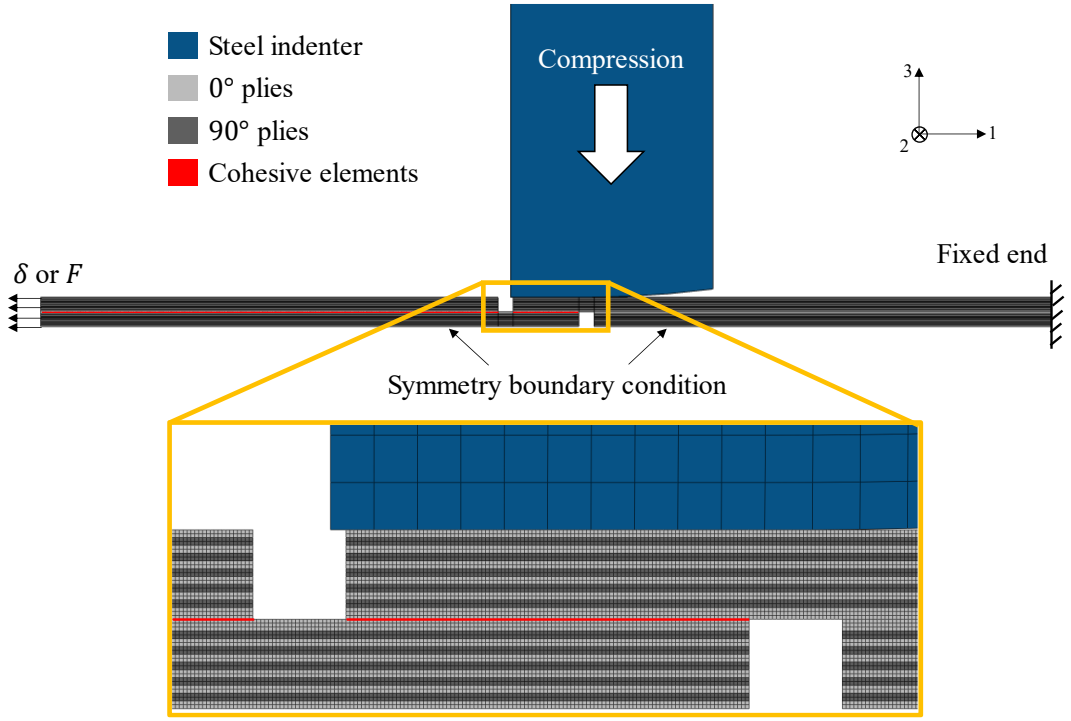

Figure 3.9. The finite element model of the symmetric DNS used in the verification study.

Zero-thickness built-in cohesive elements are inserted in regions as shown in Figure 3.9. USDLFD subroutine is utilized to take the enhancement into account. Cohesive element properties in Table 3.3 are employed, and material properties of IM/8552 carbon epoxy unidirectional pre-preg, given in Table 3.4, are used. Considering the mesh study performed by Zou and Lee [38] on the same symmetric double-notch experiment model, an element size of 0.0625 mm x 0.0625 mm is used for the

composite material, and 0.0625mm is utilized for cohesive elements. The value of the contact clearance is taken as $\delta_{\text{clearance}} = 7.5 \text{ x } 10^{-7}\text{m}$.

Table 3.4. Mechanical properties of the IM/8552 unidirectional pre-preg unidirectional tape [33].

E_1 (GPa)	$E_2 = E_3$ (GPa)	$G_{12} = G_{13}$ (GPa)	G_{23} (GPa)	$v_{12} = v_{13}$	v_{23}
135.2	9	5	3.3	0.3	0.5

The interlaminar strength and fracture toughness values with respect to the compressive stress listed in the material property section in ABAQUS for enhancement calculation are given in Table 3.5 and Table 3.6 for an enhancement coefficient of $\eta_f = 0.3$, which is used for the same material in Ref. [33].

Table 3.5. Cohesive strength values used in SDNS verification study depending on the compressive stress .

Normal Strength (MPa)	Shear Strength First direction (MPa)	Shear Strength Second direction (MPa)	Field Variable $\boldsymbol{\tau_n}(\mathbf{MPa})$
60	82.6	82.6	0.0
60	82.9	82.9	-1.0
…	…	…	…
60	172.6	172.6	-300.0

Table 3.6. Cohesive fracture toughness values used in SDNS verification study depending on the compressive stress.

Normal Mode Fracture Energy (N/mm)	Shear Mode Fracture Energy First direction (N/mm)	Shear Mode Fracture Energy Second direction (N/mm)	Field Variable $\boldsymbol{\tau_n}(\mathbf{MPa})$
200	1000	1000	0.0
200	1007	1007	-1.0
…	…	…	…
200	4366	4366	-300.0

The effect of considering the enhancement of interface properties for layup A with 10 kN transverse compression is shown in Figure 3.10. When the enhancement is not considered in the simulation, shear failure occurs in the gage section of the specimen, corresponding to a sudden drop in the load-displacement curve. However, consideration of the enhancement of the interface properties results in much higher final shear failure load, again at the gage section, which proves the compression-induced enhancement on the shear strength of the laminate. Moreover, before the final failure is observed, a crack initiates outside of the gage section, at external notches. This crack propagates toward the end of the specimen, creating a softening region in the load-displacement curve.

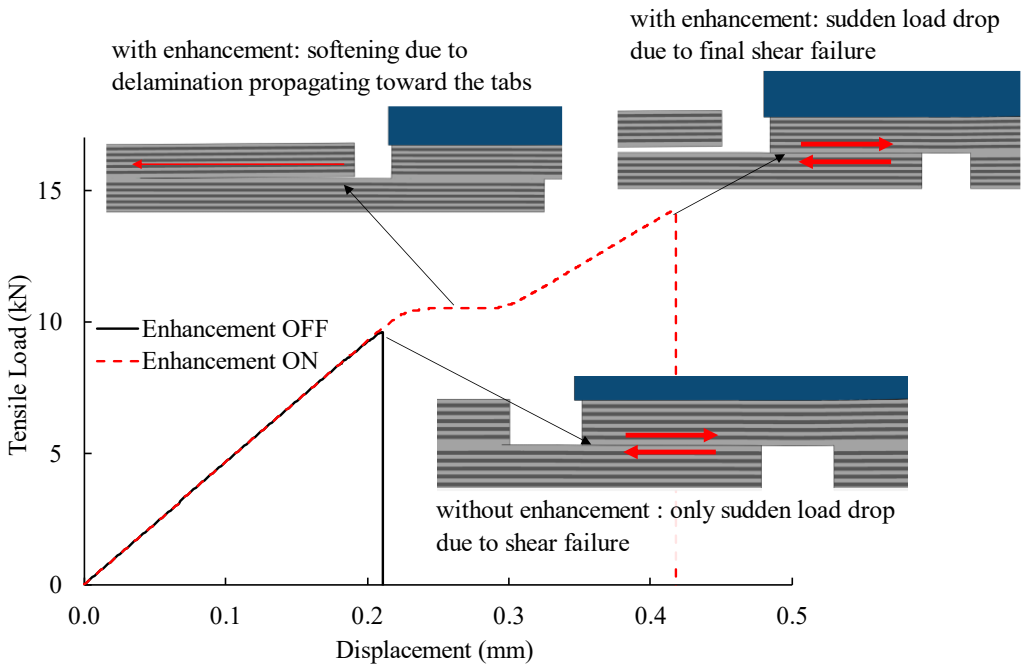

Figure 3.10. Difference in failure mechanism of the symmetrical DNS with and without considering enhancement for layup A with 10 kN transverse load.

Experimental and numerical results for the 10 kN and 20 kN through-thickness load cases obtained from Ref. [33] are compared with the current study in Figure 3.11. In the reference study, the numerical displacements obtained through the finite element analysis were proportionally adjusted to align with the initial elastic slope observed in the experimental data in Ref. [33]. Therefore, to be consistent the same scaling to the numerical data is applied in this study as well. For both 10 kN and 20 kN

transverse loading conditions, built-in cohesive elements modified by the USDFLD subroutine demonstrated almost identical results with the custom interface elements developed in VUEL subroutine in Ref. [33]. The increase of the final failure load as the compressive load is increased from 10 kN to 20 kN is an indication of enhancement of the shear strength under compressive load. Although the final failure load of the experiment for the 20 kN transverse loading condition is underestimated by both VUEL (in Ref. [33]) and USDFLD (in this study), the purpose of the current study is to replicate the results by using available cohesive elements in ABAQUS with a practical subroutine instead of developing a custom interface element from scratch. In that sense, overlapping results for USDFLD and VUEL for different through-thickness compression values in Figure 3.11 demonstrate that the subroutine developed in this study is adequate to represent the compression-induced enhancement of the interlaminar shear properties.

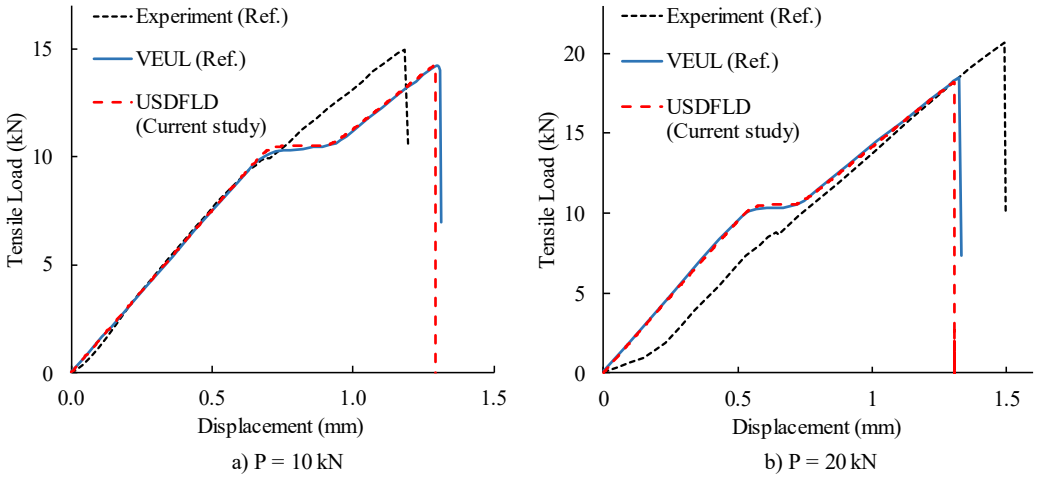

Figure 3.11. Comparison of the load-displacement response of experimental and numerical results from Ref. [33] with the current study with $\delta_{clearance} = 7.5 \times 10^{-7}$m for through-thickness compressive load values of (a) 10 kN and (b) 20 kN.

A final comment about the symmetric DNS simulation is the amount of contact clearance defined in the analysis. Figure 3.12 illustrates the variation of final failure load with respect to contact clearance for laminate A with the 20 kN transverse

compressive load. When there is no clearance in the contact algorithm, cohesive elements and contact stiffness share the compressive load in the interface between each other. Given that the enhancement of the shear strength with USDFLD is calculated according to the compressive stress on the cohesive elements, the final failure load becomes lower than expected when the contact clearance is not sufficient. Hence, the enhancement does not occur properly. However, with an increase in contact clearance, the final failure load demonstrates an upward trend and eventually stabilizes after a certain value. This is the point where the contact algorithm does not carry any compressive load, the compressive load is solely carried by the cohesive elements. Therefore, it is important to define the contact clearance when the enhancement of the interface properties is computed by using compressive stress values on the elements, and simultaneously contact is defined in the simulation to prevent the penetration of the crack surfaces after delamination.

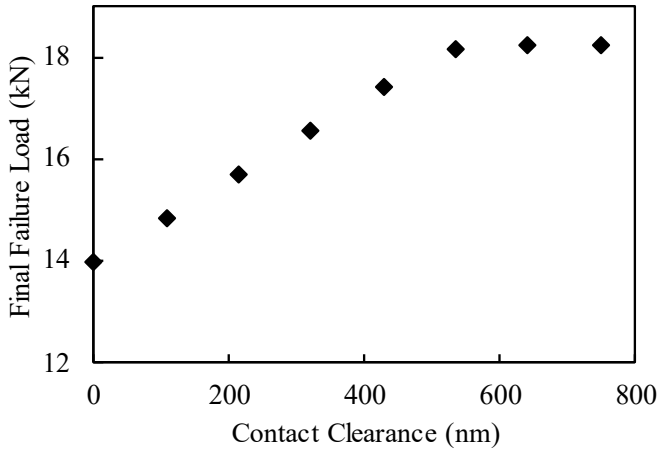

Figure 3.12: Final failure load vs contact clearance for laminate A with P=20kN.

3.2.2 Finite Element Model of a Single-Stage Ply Drop-Off Region

In this section, a finite element model of a single-stage asymmetrical ply drop-off region is created. The selection of material properties, cohesive zone parameters, and mesh size are reported. The results are compared with the experimental study conducted with dropped ply specimens in Chapter 2. Effects of enhancement of the

shear properties due to compression, fracture toughness around the resin pocket, and voids in the resin pocket on delamination onset loads are investigated. Finally, the effect of taper angle on delamination onset load and location is investigated through a parametric taper angle study to identify the critical delamination mode in highly tapered laminates.

3.2.2.1 Material Properties

The mechanical and interface properties for Interglass 92145/CR80 glass fiber composite material and CR80 resin system, obtained in the material characterization study in Chapter 2, are given in Table 3.7. The nominal ply thickness of Interglass 92145/CR80 unidirectional glass fiber composite material is calculated as 0.165mm.

Table 3.7. Mechanical properties of Interglass 92145/CR80 composite material and pure CR80 resin obtained from the material characterization tests.

Mechanical properties of Interglass 92145/CR80 unidirectional composite material

$E_1\ (GPa)$	$E_2\ (GPa)$	$G_{12}\ (GPa)$	v_{12}
38.88	12.16	4.60	0.266

Interlaminar properties of Interglass 92145/CR80 unidirectional composite material

$\tau_s^0\ (MPa)$	$G_{Ic}\ (N/mm)$	$G_{Ic}\ (N/mm)$
45.8	0.886	1.207

Elastic properties of CR80/CH80-6 resin

$E\ (GPa)$	v
3.22	0.385

In order to model an orthotropic material, nine engineering constants are required, which are E_1, E_2, E_3, G_{12}, G_{13}, G_{23}, v_{12}, v_{13}, and v_{23}. However, if the variation of the material properties in the transverse directions is neglected; that is, the material is transversely isotropic, the number of the required material properties is reduced to five, E_1, E_2, G_{12}, v_{12}, v_{23}. The only missing property is the transverse Poisson's ratio, v_{23}. The experimental measurement of v_{23} is a challenging procedure; however, Kuo et al. [50] derived a relation for v_{23} by using wave equations for

transversely isotropic materials. As a result, the transverse Poisson's ratio can be calculated by using Equation (3.14)

$$v_{23} = \frac{-E_2[E_1(1/2 - v_{12}) + 2G_{12}v_{12}^2] + \Lambda}{2E_1G_{12}} \tag{3.14}$$

where:

$$\Lambda = \sqrt{E_2^2\left[E_1\left(\frac{1}{2} - v_{12}\right) + 2G_{12}v_{12}^2\right]^2 - 4E_1G_{12}\left[E_1E_2\left(\frac{1}{2} - v_{12}\right) - G_{12}(E_1 - 2E_2v_{12}^2)\right]} \tag{3.15}$$

After the calculation of v_{23}, Equation (3.16) is used for a transversely isotropic material to calculate G_{23}.

$$G_{23} = \frac{E_2}{2(1 + v_{23})} \tag{3.16}$$

By substituting the material properties given in Table 3.7 for Interglass 92145/CR80 composite material into Equations (3.15), (3.14), and (3.16), transverse Poisson's ratio and transverse shear modulus can be calculated as 0.337 and 4.55 GPa, respectively. Consequently, the mechanical properties of both the glass fiber composite material and the resin system utilized for the finite element models in this study are acquired, as presented in Table 3.8. The mixed mode parameter, η, used in the BK criteria is calculated as 2.6 for glass fiber composite material in Ref. [49]. Since the interlaminar normal strength of the laminate is not measured in the experimental study, a reasonable value of 40 MPa is assumed.

Table 3.8. Mechanical properties of Interglass 92145/CR80 composite materials and pure CR80 resin used in the finite element models.

Elastic properties of Interglass 92145/CR80 unidirectional composite material

E_1 (GPa)	$E_2 = E_3$ (GPa)	$G_{12} = G_{13}$ (GPa)	G_{23} (GPa)	$v_{12} = v_{13}$	v_{23}
38.88	12.16	4.60	4.55	0.266	0.337

Interlaminar properties of Interglass 92145/CR80 unidirectional composite material

τ_n^0 (MPa)	$\tau_s^0 = \tau_{st}^0$ (MPa)	G_{Ic} (N/mm)	$G_{IIc} = G_{IIIc}$ (N/mm)	η
40.0	45.8	0.886	1.207	2.6

Mechanical properties of CR80 resin

$E\ (GPa)$	v
3.22	0.385

3.2.2.2 Model Details

The 2D finite element model of the laminate with a single-stage ply drop-off that is generated is shown in Figure 3.13. ABAQUS Dynamic Implicit solver is utilized. The model is 140mm long, and ply termination occurs in the middle of the specimen. The model is fixed at the beginning of the thick section, and the displacement boundary condition is given at the end of the thin section in the horizontal tensile direction. The movement of the nodes in the vertical direction is also constrained at the boundary at which the displacement is applied. In the tapered laminate, dropped, belt, and core sub-laminates have six plies, all of which have 0° orientation. The nominal ply thickness is taken as 0.165 mm. Therefore, the dropped ply specimen with a thickness transition from 2.97 mm to 1.98 mm is investigated.

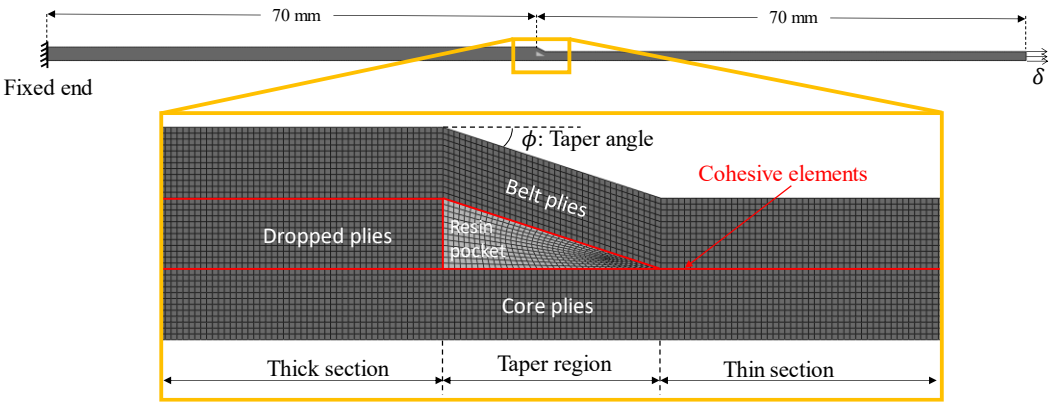

Figure 3.13. Finite element model of a laminate with a single-stage ply drop-off.

Four-node bilinear quadrilateral plane strain elements (CPE4) are used for the ply material, and four-node two-dimensional cohesive elements (COH2D4) available in ABAQUS are utilized to predict delamination. The constitutive response of the cohesive elements is manipulated by using the USDFLD subroutine as explained previously to take enhancement of the shear strength and mode II fracture toughness due to the presence of compression into account. Enhancement coefficient, η_f, employed in Equations (3.10) and (3.11) is calculated as 0.65 for a similar material in Ref. [37] for the dropped ply, single shear, and cut ply specimens. Therefore, the value of $\eta_f = 0.65$ used in this study. Zero-thickness cohesive elements are inserted between sub-laminates and around the resin pocket, illustrated in Figure 3.13. No cohesive element is inserted within the core, dropped, and belt sub-laminates. For the ply material, Interglass92145/CR80 unidirectional composite material is used, and linear elastic isotropic material properties of the CR80 resin system are utilized for the resin pocket. The mechanical properties of the materials used in this study are listed in Table 3.8.

Selection of the penalty stiffness values for cohesive elements is critical since a high value of penalty stiffness may result in spurious oscillations of tractions [51] whereas a low value of penalty stiffness may cause undesired compliance to the model. Turon et al. [52] suggested the following relation to determine the penalty stiffness of the interface elements in the normal direction.

$$K_n = \frac{\alpha E_3}{t} \tag{3.17}$$

In Equation (3.17), E_3 is the elastic modulus of the adjacent material in through the thickness direction, t is the sublaminate thickness and parameter α is larger than 1. The value of α larger than 50 resulted in reasonably accurate solutions [52]. Therefore, the value of 50 is selected for α in this study. For the penalty stiffness in the shear direction, Equation (3.18) is suggested [53].

$$K_s = K_n \frac{G_{Ic}}{G_{IIc}} \left(\frac{\tau_{sh}^0}{\tau_n^0} \right) \tag{3.18}$$

As a result, the penalty stiffness values for the cohesive elements are calculated by using Equations (3.17) and (3.18), and the results are listed in Table 3.9.

Table 3.9. Penalty stiffness values for cohesive elements.

K_n (N/mm^3)	K_s (N/mm^3)	K_{st} (N/mm^3)
6.1e5	5.9e5	5.9e5

3.2.2.3 Element Size Selection and Penalty Stiffness Check

The selection of appropriate element size becomes challenging when the cohesive zone modeling technique is used in delamination prediction because a sufficient number of elements must be placed in the cohesive zone in front of the crack tip [54]. Determination of the maximum allowable element size requires the prediction of the cohesive zone length ahead of a crack tip. Different relations are suggested for the prediction of the cohesive zone length. For example, the following relations are suggested for the cohesive length prediction for an orthotropic material under mode I and mode II loading conditions [55,56].

$$l_{ch,I} = E_I' \frac{G_{IC}}{(\tau_n^0)^2} \tag{3.19}$$

$$l_{ch,II} = E_{II}' \frac{G_{IIC}}{(\tau_s^0)^2} \tag{3.20}$$

In Equations (3.19) and (3.20), E_I' and E_{II}' are equivalent elastic modulus for an orthotropic material. A modified version of the cohesive zone length equation is developed by Yang and Cox [55] for slender laminates. Their modified formulation is given as follows:

$$l_{ch,slender,I} = \left(E_I' \frac{G_{IC}}{(\tau_n^0)^2} \right)^{\frac{1}{4}} h^{\frac{3}{4}} \tag{3.21}$$

$$l_{ch,slender,II} = \sqrt{\left(E_{II,slender}' \frac{G_{IIC}}{(\tau_s^0)^2} \right) h} \tag{3.22}$$

Harper and Hallet [54] suggested a strategy for the determination of the maximum allowed element size that can be used in the cohesive zone modeling technique.

i) First, the minimum cohesive zone length is calculated by

$$L_{CZ,min} = 0.5 \min \{Equations\ (3.19), (3.20), (3.21), (3.22)\} \tag{3.23}$$

ii) Then, the minimum cohesive zone length is divided by the minimum number of elements that must be placed in the cohesive zone, $N_{el,min}$.

$$L_{el,max} = \frac{L_{CZ,min}}{N_{el,min}} \tag{3.24}$$

As a result, the maximum allowed element length, $L_{el,max}$, can be calculated. By applying the procedure presented above, the maximum allowed cohesive element length is calculated as 0.161 mm for the current material, which is slightly lower than the nominal ply thickness value of the material, 0.165mm.

For the mesh study of the model, ply-dropping configurations having 10° and 20° taper angles are investigated under uniaxial tensile loading and enhancement of interface properties is not considered. Thin section delamination, which is the separation of belt plies and core plies at the beginning of the thin section due to straightening of the belt plies under tensile loading, is observed in 20° taper angle configuration whereas thick section delamination, sliding of the dropped plies between core and belt plies, occurs in 10° taper angle configuration. Thin and thick section delamination modes in the current ply drop-off configuration are shown in Figure 3.14.

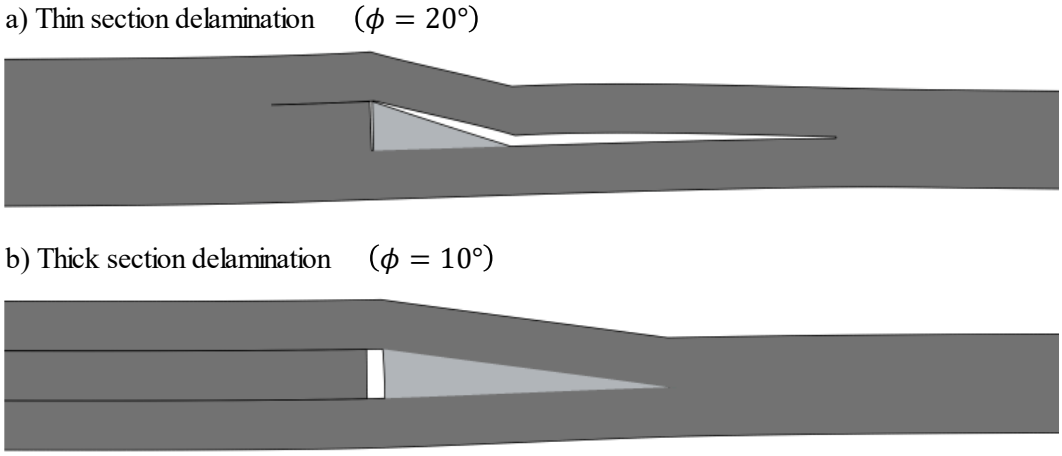

Figure 3.14. Thin and thick section delamination modes in single-stage ply drop configurations.

In the mesh study, the investigated element sizes are 0.1650 mm, 0.0825 mm, 0.055 mm, and 0.04125 mm, corresponding to 1, 2, 3 and 4 elements per ply thickness, respectively. The aspect ratio of the elements is kept at one. The cohesive element size is equal to the composite element size. The effects of element size on the delamination onset load at the thin and the thick sections are shown in Figure 3.15. The results indicate that both the onset loads for thin section and thick section delamination do not exhibit significant variations with the reduction in element size for the specified mesh sizes. Even one element per ply thickness seems accurate enough to predict the delamination onset with the current models. However, considering that the maximum allowed element size for the cohesive element length

is found to be 0.161 mm, element size of 0.0825 mm x 0.0825 mm for solid elements and 0.0825 mm for cohesive elements are used in the remaining part of this chapter.

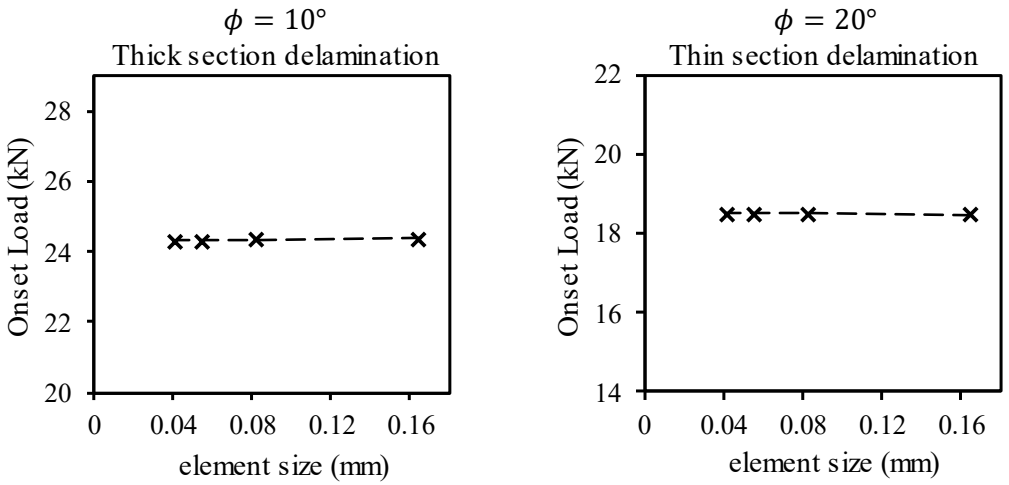

(a) (b)

Figure 3.15. Variation of delamination initiation loads in thick and thin sections depending on the element size.

The penalty stiffness value defined in the cohesive law must not introduce additional compliance to the model. In order to check the effect of cohesive stiffness on the global stiffness of the model, finite element models of the dropped ply specimens with and without cohesive elements are generated for $\phi = 10°$ and $\phi = 20°$. The load-displacement response for the models is compared in Figure 3.16. The overlapping of initial slopes of the load-displacement curve for models with and without cohesive elements indicates that no artificial compliance is introduced to the models. Hence, the penalty stiffness values used in the cohesive law are sufficiently high. The discrepancy in the load-displacement curves starts to emerge with the occurrence of delamination in the models with cohesive elements because the delamination event introduces non-linearity to the finite element models.

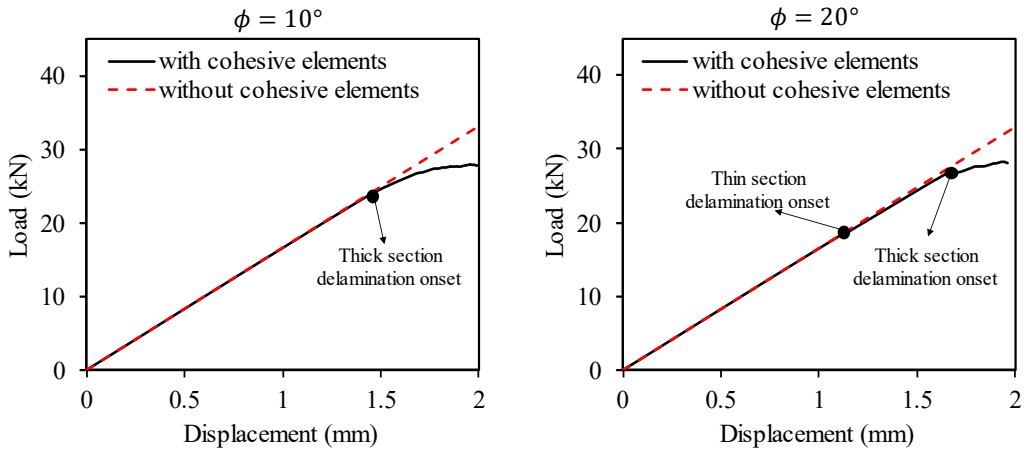

(a) (b)

Figure 3.16. Comparison of the load displacement response of the finite element models of dropped ply specimens with and without cohesive elements inserted in the models for (a) $\phi = 10°$ and (b) $\phi = 20°$.

3.3 Comparison of the Numerical Results with the Dropped Ply Experiment

In this section, a comparison of the experimental results obtained from dropped ply specimen tests and finite element simulations is performed. Since the average taper angle of the dropped ply specimens is measured as 16.2°, finite element models of the dropped ply specimen with $\phi = 16.2°$ are created. First effect of modeling details are investigated such as fracture toughness around the resin pocket, voids in the resin pocket, and effect of through-thickness compressive enhancement (TTCE) on shear properties. Following the refinement of the finite element model through the identification of necessary modeling details, a comparison is made between experimental and numerical failure sequences, as well as load-displacement responses.

3.3.1 Effect of Resin Toughness and Voids on Delamination Onset

In this section, the effect of different finite element modeling techniques for the resin pocket of the dropped ply specimen, as depicted in Figure 3.17, is investigated. In

the conventional modeling technique, cohesive elements are placed between the sub-laminates and around the resin pocket region, and the resin pocket is modeled as a linear elastic isotropic material [2,11,46]. The interlaminar strength and toughness properties of the laminate are also used for the cohesive elements around the resin pocket in the conventional modeling technique. However, the strength and the fracture toughness properties around the resin pocket may not be equal to the interlaminar properties of the composite. Therefore, a finite element model of the same dropped ply configuration with resin interface properties around the resin pocket is also created, which is illustrated in Figure 3.17(b). Moreover, to see the effect of void formation in the resin pocket during the manufacturing process, the finite element model without a resin pocket is also created as shown in Figure 3.17(c). For this section, the effect of through-thickness compression enhancement is not included in the models.

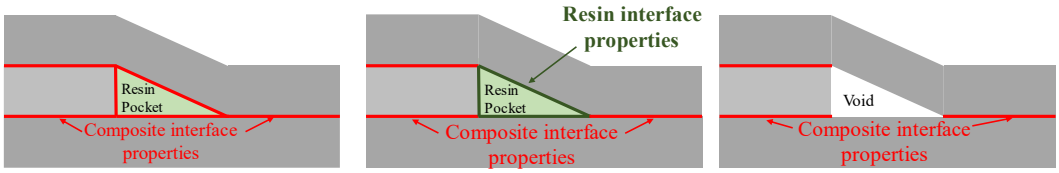

a) Conventional FEM

b) FEM with resin interface properties around the resin pocket

c) FEM without resin pocket (Void)

Figure 3.17. (a) Conventional dropped ply specimen modeling technique, (b) Finite element model with resin interface properties used around the resin pocket, (c) Finite element model without resin pocket at the end of the dropped sub-laminate.

Resin and composite material interface properties used in the finite element models are given in Table 3.10. For both composite and the resin, the BK parameter is selected as 2.6 from Ref.[49] for GFRP, and the same value is also used for the resin interface properties in this study. The tensile strength of the resin obtained in Chapter 2 is used as the interface strength of the resin, with equality assumptions made for interface strengths in all directions. Likewise, the fracture toughness of the resin obtained from the SENB test is used for all fracture modes.

Table 3.10. Interface properties of Interglass 92145/CR80 composite material and pure CR80 resin used in the finite element models.

Interface properties of Interglass 92145/CR80 composite

τ_n^0 (MPa)	$\tau_s^0 = \tau_{st}^0$ (MPa)	G_{Ic} (N/mm)	$G_{IIc} = G_{IIIc}$ (N/mm)
40.0	45.8	0.886	1.207

Interface properties of CR80 resin

$\tau_n^0 = \tau_s^0 = \tau_{st}^0$ (MPa)	$G_{Ic} = G_{IIc} = G_{IIIc}$ (N/mm)
77.8	0.131

The delamination onset loads for the thin section and the thick section obtained from the experiments and different finite element modeling techniques are compared in Figure 3.18. The onset of the thick section delamination does not show any dependency on the interface properties used around the resin pocket or the existence of the resin pocket. On the other hand, employing the resin fracture toughness and strength around the resin pocket results in a lower thin section delamination onset load compared to the conventional modeling technique. A similar result for the thin section delamination is obtained when the resin pocket is modeled as a void. It appears that the resin pocket acts as a resistance to the initiation of thin section delamination. Consequently, when the fracture toughness and strength around the resin pocket are reduced or the resin pocket is eliminated entirely, the onset load for thin section delamination decreases. This study shows that conventional modeling technique yields the closest results to the experimental thin section delamination onset load. Therefore, the conventional modeling technique is followed in the remainder of the study.

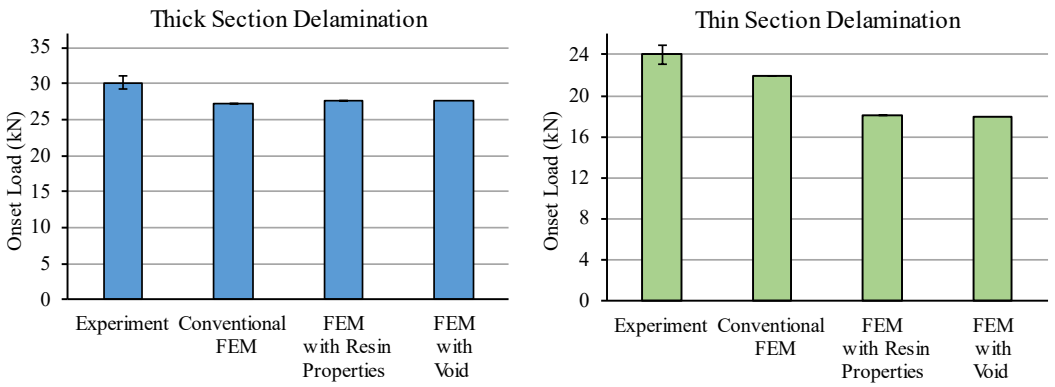

(a) (b)

Figure 3.18. (a) Thick section delamination onset loads from experiments and different finite element modeling techniques, (b) Thin section delamination onset loads from experiments and different finite element modeling techniques.

3.3.2 Effect of the Through-Thickness Compression Enhancement

The effect of the through-thickness compression enhancement (TTCE) on the interlaminar shear strength and fracture toughness is taken into account with USDFLD subroutine as explained previously. The initiation of the thin section and the thick section delamination onset loads obtained with and without TTCE are compared with the experimental delamination onset loads in Figure 3.19. Taking TTCE into account increases the predicted thick section delamination onset load and makes it closer to the experimentally measured thick section delamination onset load. However, TTCE has no noticeable effect on the delamination onset load at the beginning of the thin section of the laminate as shown in Figure 3.19(b). To explain this behavior, the interlaminar normal and shear stresses around the ply termination for the current configuration are given in Figure 3.20. The presence of the compressive stress at the end of the dropped sub-laminate increases the shear strength and mode II fracture toughness when TTCE is considered with the USDFLD subroutine. Consequently, by including TTCE in the finite element model, the thick section delamination onset load increases and gets closer to the experimental value. On the other hand, the normal stresses at the beginning of the thin section are tensile as shown in Figure 3.20; therefore, taking TTCE into account does not influence the

predicted delamination onset loads in the thin section. Given that the incorporation of TTCE aligns with the experimentally observed thick section delamination onset load, TTCE is included in the remainder of the analysis conducted in this study.

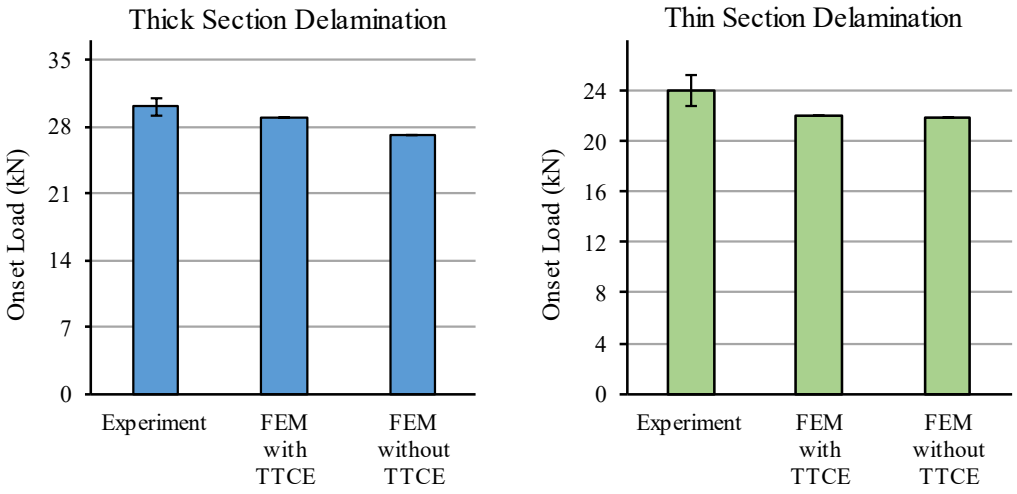

(a) (b)

Figure 3.19. Comparison of the experimental delamination onset loads at (a) the thick section and (b) at the thin section with delamination onset loads predicted by FEM model with and without through the thickness compression enhancement (TTCE) effect for the 16.2° taper angle.

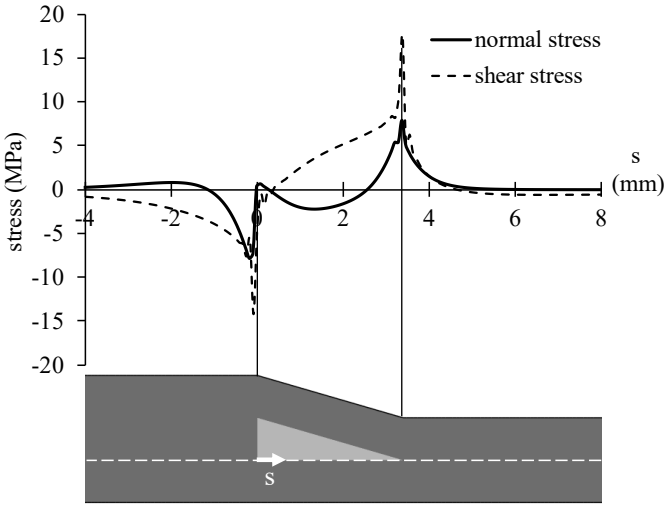

Figure 3.20. Interlaminar normal and shear stress distribution for the dropped ply specimen with 16.2° taper angle under tensile loading before the initiation of damage on any cohesive elements.

3.3.3 Failure Sequences and Load-Displacement Responses

In this section, experimental and numerical failure sequences, corresponding load levels, and load-displacement responses for the single stage dropped ply configuration are compared. Conventional resin pocket modeling technique is used in the finite element model, and TTCE is taken into account. Delamination modes and their corresponding onset loads from both experiments and finite element simulations are presented in Figure 3.21. While the failure sequence is illustrated for only specimen 1 in the figure, the average delamination onset loads for all specimens are provided along with coefficients of variation. The predicted delamination modes and their sequence with the finite element model are consistent with the experimental observations. Initially, in the simulation, thin-section delamination occurs, followed by the observation of thick-section delamination as the specimen is further loaded. The same behavior is witnessed during the experiments. In the context of the initiation loads for delamination, the finite element model exhibits a marginal underestimation of the average experimental delamination onset loads; nevertheless, the results fall within the range of experimental variation.

In Figure 3.21, the load-displacement responses from the dropped ply specimen 1 and finite element model are given. The thin section delamination, which is the first observed delamination mode, can be identified with a small load drop in the load-displacement curve for both the experiment and finite element models. However, it is important to remember that this tiny load drop corresponding to the thin section delamination was not visible for some dropped ply specimens as mentioned in the dropped ply experiments section in Chapter 2. As the load level is increased after the thin section delamination, the thick section delamination occurs. The thick section delamination creates a significant softening in the load-displacement response of the finite element simulation whereas it causes a sudden load drop in the experiments. The thick section delamination is followed by fiber fracture in the test; however, this behavior cannot be captured in the simulation since the fiber fracture is not taken into account in the finite element model.

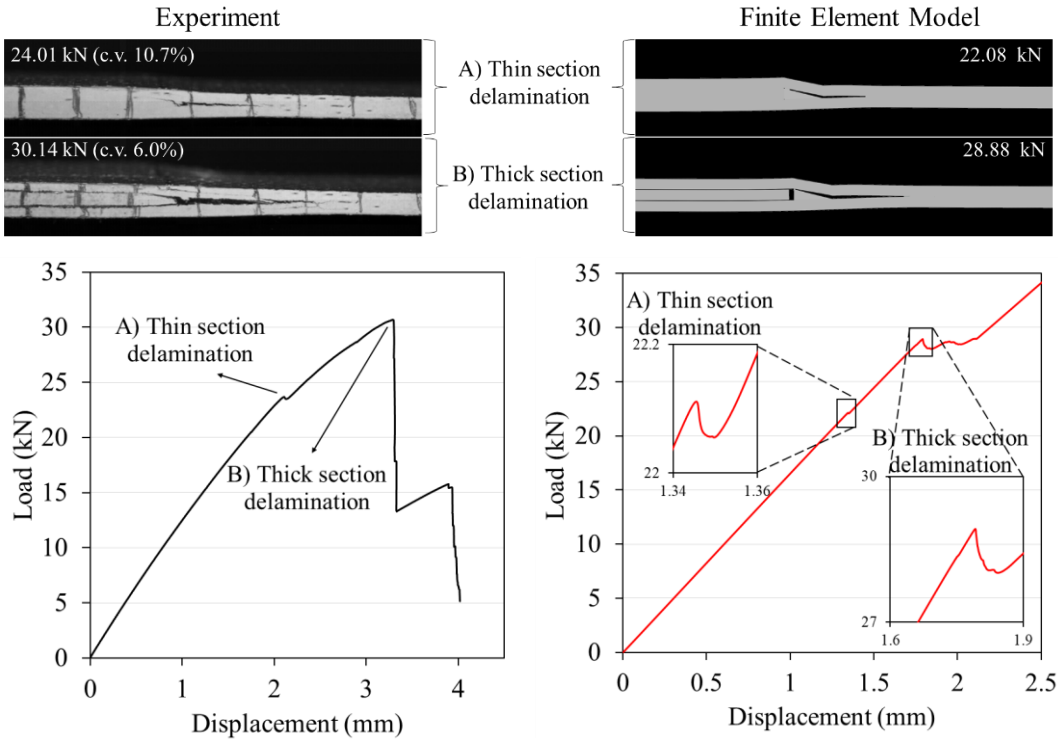

Figure 3.21. The experimentally observed and numerically predicted failure sequence and corresponding load levels for the single stage ply drop-off are compared on the upper side. Experimental (left) and numerical (right) load displacement curves are compared at the bottom side.

The reason why two delamination modes have different effects on the load-displacement response can be understood by looking at the stress field around the ply drop-off region after the thin and thick section delamination in the finite element model. In Figure 3.22, stress contour in the fiber direction, σ_{11}, is presented after the thin and thick delamination in the single stage dropped ply model with $\phi = 16.2°$. Even though there is a variation in the stress field around the ply drop-off region after the thin section delamination as shown in Figure 3.22(a), far-field stress distribution is uniform and undisturbed. Moreover, the thin section crack only propagates for a couple of millimeters and stops, hence the occurrence of the thin section delamination only creates a small load drop. However, the thick section cracks propagate all the way to the left boundary and make the dropped sub-laminate unable to carry any load as shown in the stress contour in Figure 3.22(b). This event results in a significant loss of stiffness for the laminate. As a result, a noticeable

softening in the load-displacement curve in the numerical simulation or significant load drop in the experiments is observed after the occurrence of thick section delamination observed in the drop ply specimen configuration investigated in this study.

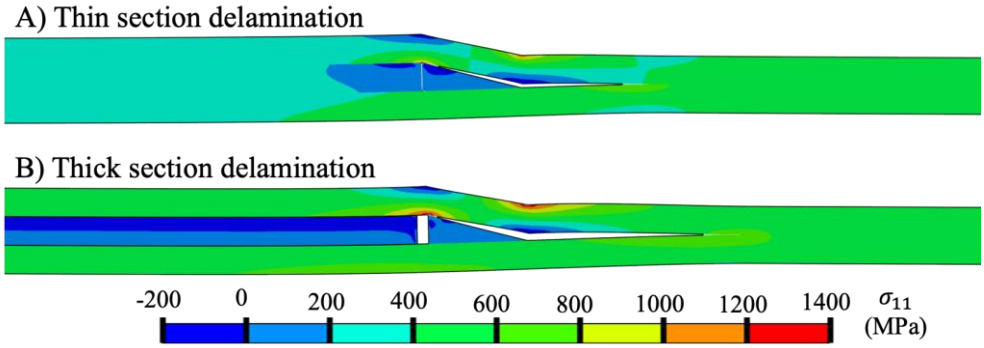

Figure 3.22. Stress distribution in the fiber direction around the ply drop-off region for the 16.2° taper angle under tensile loading after (a) the thin section and (b) the thick section delamination.

As a final comment about the load-displacement responses, the total specimen elongation obtained from the testing machine crosshead displacement and the one obtained from DIC measurements are compared with the finite element model in Figure 3.23. Since accurate measurements could not be obtained after the failure onset with DIC measurement, only initial load-displacement load-displacement responses are compared. The reason for the discrepancy between the initial slopes of the experiments with and without DIC is that the displacement of the crosshead also includes the compliance of the testing machine whereas the DIC system only calculates the deformations in the specimen. When the elongation in the test specimen is calculated using the DIC system, the load-displacement response perfectly aligns with the finite element model. This further validates the elastic properties of the material employed in the finite element model, particularly the elastic modulus in the fiber direction, E_1.

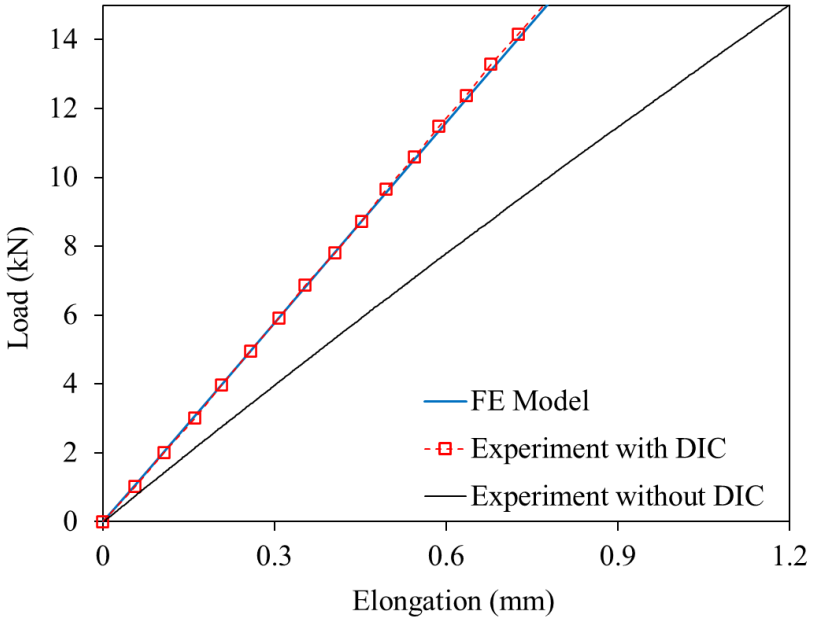

Figure 3.23. Comparisons of the initial load-displacement responses obtained from DIC measurement, crosshead displacement of the testing machine, and finite element model.

3.4 Parametric Taper Angle Study

In this section, the effects of the taper angle on delamination initiation loads in the thin and thick sections of the laminate are investigated. The finite element model of the ply-dropping configuration, defined in the previous section, is generated for taper angles ranging from 10° to 20°. The delamination onset loads with respect to the taper angle are shown in Figure 3.24. The thick section delamination is observed in the laminate at low taper angles, and the delamination onset load does not change when the taper angle is between 10°- 14°. As the taper angle is increased further, the first delamination mode becomes the thin section delamination, and the delamination onset load decreases drastically even with a small increment in the taper angle. When the simulation is continued, the thick section delamination is also observed after the onset of the thin section delamination. Initiation of the thin section delamination changes the stress distribution around the end of the dropped plies, and this effect delays the thick section delamination onset for taper angles between 14°-

20°. The occurrence of thick section delamination after the thin section delamination is the same failure sequence observed in the dropped ply experiments reported in Chapter 2. This indicates that dropped ply specimens tested in this study fall within high taper angle regions, where the thin section delamination is the first observed delamination mode. The average delamination onset loads from the experiments and corresponding locations are also given in Figure 3.24.

The dependency of the delamination location and onset loads on the taper angle can be understood more clearly when the interlaminar stress distributions around ply drop-off regions are investigated. Interlaminar normal and shear stress distributions for 10° and 20° taper angle ply drop-off configurations are shown in Figure 3.25. Interlaminar stresses are taken from the cohesive elements, shown with the dashed path in Figure 3.25, when the two laminates are subjected to the same load. Stresses are normalized with respect to their strength values and the distance in the taper region is scaled for illustrative purposes such that both laminates have the same taper length. Plots reveal that interlaminar normal tensile and shear stresses at the beginning of the thin section elevate as the taper angle is increased from 10° to 20°. This elucidates the observed shift in delamination initiation location from the thick section to the thin section and the decrease in onset load as the taper angle is increased. These results show that delamination initiates at the beginning of the thin section of the highly tapered laminates, and the delamination onset load becomes very sensitive to the taper geometry due to the change in the interlaminar stress distribution at the thin section.

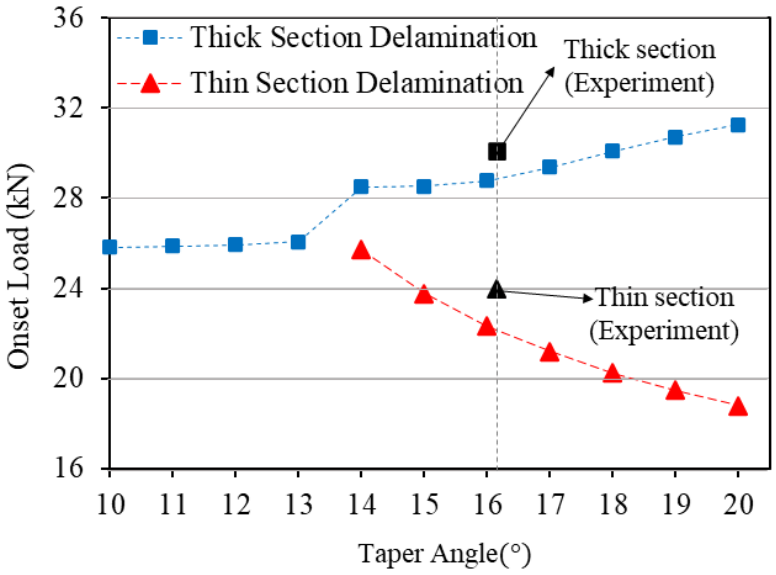

Figure 3.24. The delamination onset loads predicted with FE model of single-stage ply drop-off configuration for different taper angles, and comparison with the experimental average delamination onset loads and locations for $\phi = 16.2°$.

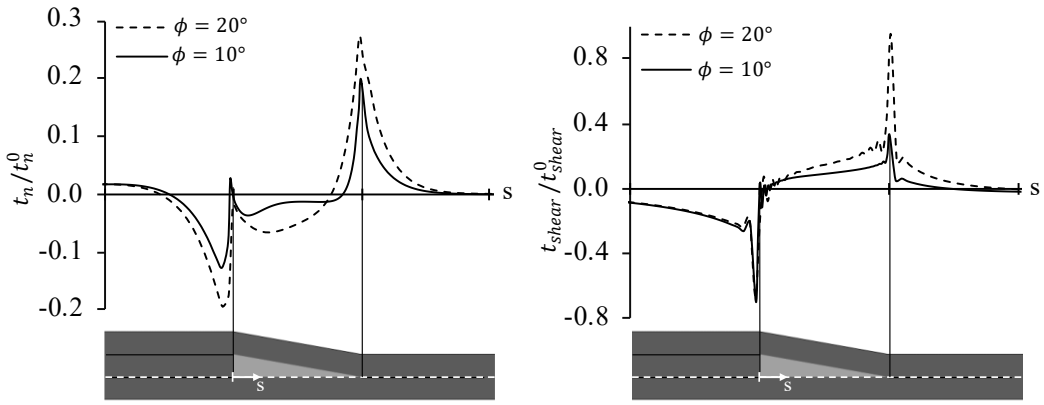

Figure 3.25. Comparison of interlaminar normalized normal (left) and shear (right) stress distributions obtained from FEM around the ply drop off region for 10° and 20° taper angles under tensile loading.

The effect of TTCE on the onset of thick-section and thin-section delamination loads for different taper angles is also investigated, and the results are shown in Figure 3.26. The TTCE has a clear effect on the thick section delamination due to the

presence of compression at the end of the dropped plies as shown in Figure 3.25. Moreover, as the taper angle increases, the thick section delamination onset load increases when TTCE is considered. The reason is that the rise in the taper angle also increases the compressive stresses at the end of the dropped plies as shown in Figure 3.25, and the higher the compressive stresses, the greater the shear strength and fracture toughness of the laminate at the end of the dropped plies. On the other hand, since there is no compressive stress field at the beginning of the thin section to enhance the interlaminar properties, the prediction of delamination initiation loads in the thin section with and without TTCE is identical. As a result, this study demonstrates that taking the TTCE effect into account is critical when delamination in the tapered laminate initiates at the thick section of the ply drop-off region.

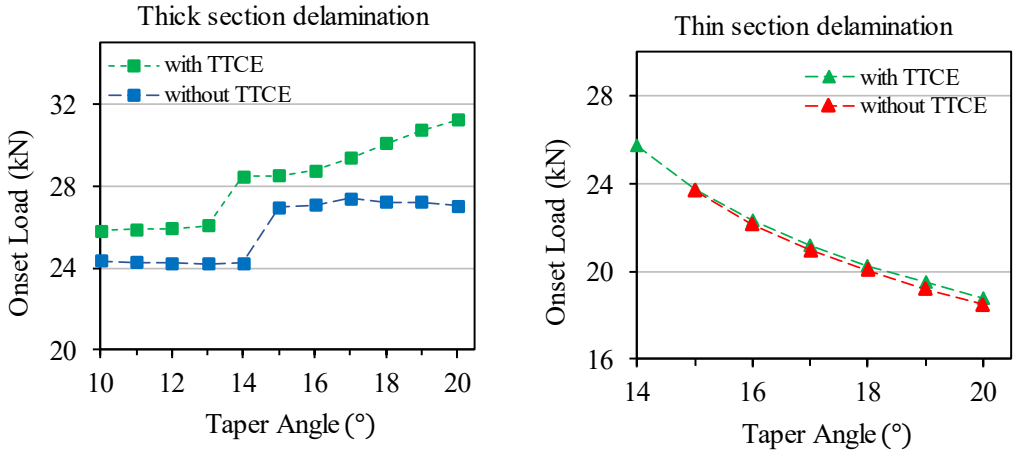

Figure 3.26. Delamination onset loads with respect to taper angle with and without TTCE for (a) thick section delamination and (b) thin section delamination.

3.5 Chapter Conclusion

In this chapter, finite element models of single-stage ply drop-off regions are created, and enhancement of the interface properties due to the presence of through-thickness compression in cohesive elements is taken into account with the USDFLD subroutine. Finite element results for the single-stage dropped ply model are compared with the experimental results. Effects of element size, taper angle, through-thickness compression enhancement, fracture toughness around the resin pocket, and voids in the resin pockets on delamination onset loads and location are investigated with numerical models.

- Verification studies with the USDFLD subroutine proved that enhancement of the interlaminar shear strength and mode II fracture toughness due to the presence of compression can be considered by utilizing built-in cohesive elements together with a simple subroutine (USDFLD) rather than developing custom cohesive elements from a scratch. However, it is important to define contact clearance in the contact algorithm to ensure accurate measurement of the compressive stresses on the cohesive elements for correct enhancement calculation.

- It is concluded that due to the presence of a compressive stress field together with the shear stresses at the end of the dropped plies, enhancement of the interface properties must be considered in order to accurately predict the delamination initiation load at the thick section of the laminate.

- The study with different finite modeling techniques of the resin pocket showed that while the thick section delamination onset load remained independent of the fracture toughness values used around the resin pocket or voids, the thin section delamination prediction load decreased significantly. It is concluded that the accurate prediction of thin section delamination onset

load is notably sensitive to the fracture toughness values applied around the ply drop-off region and the specific modeling choice regarding the representation of the resin pocket, whether as a void or not.

- The outcomes of a parametric taper angle study and analysis of interlaminar stress distributions reveal a noteworthy trend: as the taper angle increases, the initiation location of delamination shifts from the thick section to the thin section. Additionally, there is a substantial decrease in the delamination onset load. This underlines the sensitivity of the delamination onset load in highly tapered laminates to taper geometry, particularly when the delamination initiates in the thin section.

CHAPTER 4

A DELAMINATION SUPPRESSION CONCEPT IN HIGHLY TAPERED LAMINATES

4.1 Introduction

Experimental and numerical studies are performed in Chapter 2 and Chapter 3 of this study to understand the failure mechanics in ply drop-off regions. It is concluded that as the taper angle increases, the thin section delamination becomes the dominant failure mode in a single-stage ply drop-off region. Since this study focuses on improving the load-carrying capacity of highly tapered laminates, suppressing the delamination onset in the thin section of the tapered laminates becomes critical. It is also demonstrated in Chapter 3 that interlaminar stresses in the thin section increase as the taper angle is increased, which is the main reason why an increase in the taper angle decreases the delamination onset load in the thin section of the laminate. Therefore, it is necessary to reduce the stress concentrations at the beginning of the thin section of the ply drop-off region to delay delamination onset in highly tapered laminates. However, there is not enough study focusing on reducing the stress concentration in the thin section of tapered structures as reviewed in Chapter 1. Therefore, the variable taper angle concept is proposed in this study to suppress the delamination emanating from the thin section of highly tapered laminates. The advantages of the concept are investigated through a series of finite element analyses.

4.2 Variable Taper Angle Concept

In the variable taper angle design concept, each individual taper angle or stagger distance in the laminate can be different from one another rather than having a constant taper angle throughout the tapered region, as widely adopted in the industry due to its simplicity in design and manufacturing stages. Although changing each taper angle brings complexity to the design, significant improvement can be obtained by reducing the stress concentrations in the thin section of highly tapered laminates by optimizing the taper geometry. Hence, in this study, the variable taper angle design concept is investigated in detail and proposed as an alternative design concept.

In the variable taper angle concept, changing taper angles independently in ply drop-off regions results in too many design options if the permutations of all taper angles are taken as potential design variables. Considering that even a 2D finite element analysis of delamination for simple tapered laminate takes a couple of hours, determining the best taper geometry with a variable taper angle design concept would be unfeasible if all design alternatives were analyzed. However, since the main aim is to reduce the stress concentration in the tapered zone of the laminate, one can foresee that the best taper geometry would be the one that provides a gradual transition of the taper angle from the thin section to the thick section. Hence taper angles near the thin section should be small to reduce interlaminar stresses, whereas taper angles close to the thick section should be high enough to provide the thickness transition in a short distance. An illustration of the constant taper angle design and variable taper angle design concept in which the taper angle is gradually increased from the thin section to the thick section is depicted in Figure 4.1 where tapered laminates with six ply drop-off regions are shown with individual taper angles being denoted as ϕ_i, and global taper angle is ϕ_G. It should be noted that the global taper angle is equal to the individual taper angles in the conventional constant taper angle design. In order to reduce the number of design options in the variable taper angle design, each taper angle, ϕ_{i+1}, is calculated by adding the same taper angle

increment, $\Delta\phi$, to the previous taper angle, ϕ_i, as shown in Equation (4.1) where i varies from 1 to 5 for the configuration investigated in this study.

$$\phi_{i+1} = \phi_i + \Delta\phi \tag{4.1}$$

For the variable taper angle design, the first taper angle is adjusted such that transition lengths of the constant taper angle design and variable taper angle design are the same when the global taper angle and total ply drop height are the same for both configurations. When $\Delta\phi$ in Equation (4.1) is increased for the same transition length, the tapering curvature increases. The effect of different values of $\Delta\phi$ on the taper curvature is illustrated in Figure 4.1(b).

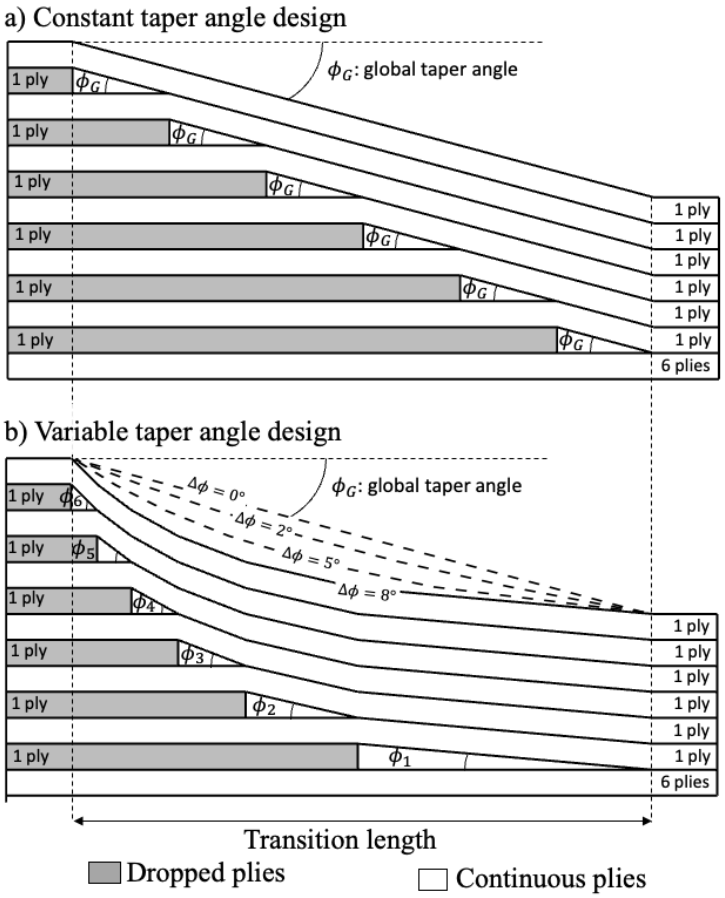

Figure 4.1. (a) Schematic of a conventional constant taper angle design in which all individual taper angles are the same and equal to the global taper angle, (b) illustration of variable taper angle design concept where consecutive taper angles are increased gradually from the thin section to the thick section.

While $\Delta\phi = 0°$ corresponds to the constant taper angle design in Figure 4.1(b), higher values of $\Delta\phi$ result in significantly non-linear taper geometry. Hence, taper transition geometry can be defined with a single parameter, $\Delta\phi$, regardless of how many plies are terminated in the taper region. This approach is the key point to make the investigation of the variable taper angle design concept feasible.

4.3 Finite Element Model of the Variable Taper Angle Concept

The finite element model of the tapered laminate with 6 consecutive ply drop-offs used in the investigation of the variable taper angle concept is shown in Figure 4.2. The model is 140 mm long and the taper section starts at the middle of the specimen. Displacement is applied at the thin section, and the model is fixed at the beginning of the thick section. Regular plane strain elements (CPE4) are used for the composite material and the resin material, and four-node 2D zero-thickness cohesive elements (COH2D4) are used for delamination prediction. Cohesive elements are inserted at all possible delamination paths except the interfaces within the core sub-laminate as shown in Figure 4.2. Unidirectional tape T300/914c for the composite material and 914c resin system for resin pockets are used. The material properties together with the cohesive interface properties are given in Table 4.1. The nominal ply thickness of the material is taken as 0.159 mm. Enhancement of the interface properties is taken into account with USDFLD subroutine as explained in Chapter 3. The enhancement coefficient, η_f, is calculated as 0.74 for a similar carbon fiber composite material in Ref. [37] for the dropped ply, single shear, and cut ply specimens. Therefore, the value of $\eta_f = 0.74$ is used in this chapter. Element size selection study is performed with the element sizes corresponding to 1, 2, 3, and 4 elements per ply thickness. Variation in the delamination onset loads predicted by the model after refining the elements size of 0.08mm, corresponding to 2 elements per ply thickness, was insignificant. Therefore, element sizes of 0.08mm x 0.08mm for solid parts and 0.08mm for cohesive elements are used.

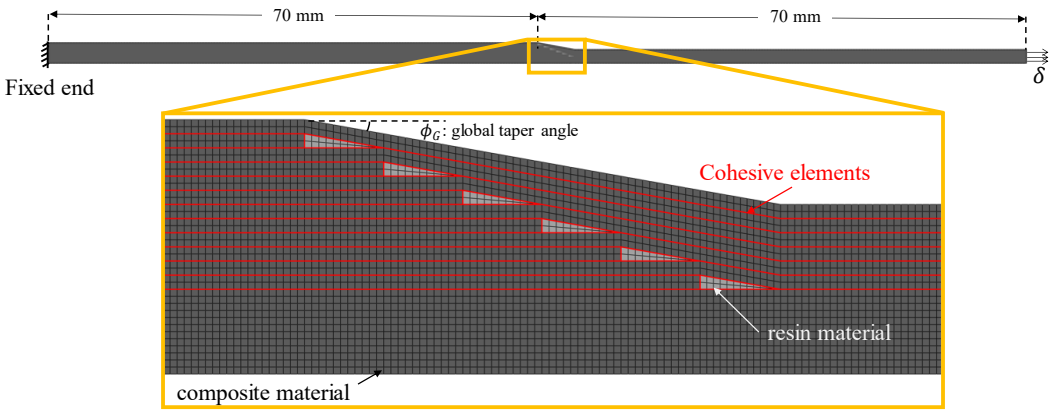

Figure 4.2. FE model of the tapered laminate containing six ply drop-offs.

Table 4.1. Mechanical properties of T300/914c unidirectional tape and 914c resin.

Cohesive interface properties of the T300/914c unidirectional tape [11,57]

G_{Ic} (N/mm)	$G_{IIc} = G_{IIIc}$ (N/mm)	σ_{Imax} (MPa)	$\sigma_{IImax} = \sigma_{IIImax}$ (MPa)	K_I (N/mm^3)	$K_{II} = K_{III}$ (N/mm^3)
0.17	0.494	75	80	4.0e6	1.5e6

Mechanical properties of the T300/914c unidirectional tape [29]

E_1 (GPa)	$E_2 = E_3$ (GPa)	$G_{12} = G_{13}$ (GPa)	G_{23} (GPa)	$v_{12} = v_{13}$	v_{23}
135.2	9	5	3.3	0.3	0.5

Mechanical properties of 914c resin [11]

E (GPa)	G (GPa)	v
4	1.481	0.35

4.4 Numerical Results

In this section, to understand the delamination mode transition angle in the tapered laminate with the conventional constant taper angle design, a parametric taper angle study is performed by only changing the global taper angle. Later, the effect of variable taper angle design on the delamination onset load is investigated.

4.4.1 Constant Taper Angle Design

In this section, all individual taper angles are equal to the global taper angle; that is, conventional constant taper angle design is investigated. Delamination modes for tapered configurations for the 3° and 10° global taper angles are shown in Figure 4.3. In thin section delamination, continuous plies between the dropped plies straighten out due to tensile loading, and multiple cracks initiate at the tip of the resin pockets. Delamination initiated at the tip of resin pockets then propagates toward the thin section of the laminate as shown for a global taper angle of 10° in Figure 4.3.

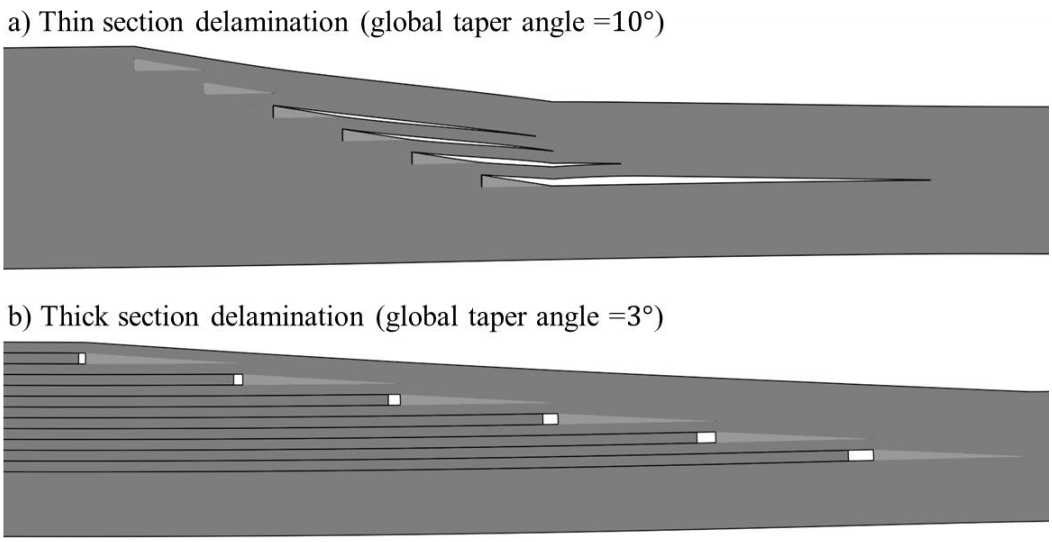

Figure 4.3. Delamination modes observed in the tapered laminate with multiple ply termination regions.

In the thick section delamination, as shown in Figure 4.3, when the global taper angle is 3°, dropped plies slide between the continuous plies and delamination propagates toward the thick section of the laminate. The load-displacement responses of constant taper angle design configurations with a global taper angle 3° and 10° are presented in Figure 4.4. The results indicate that increasing the global taper angle from 3° to 10° not only reduces the thin section delamination onset but also reduces the thick section delamination onset load as well.

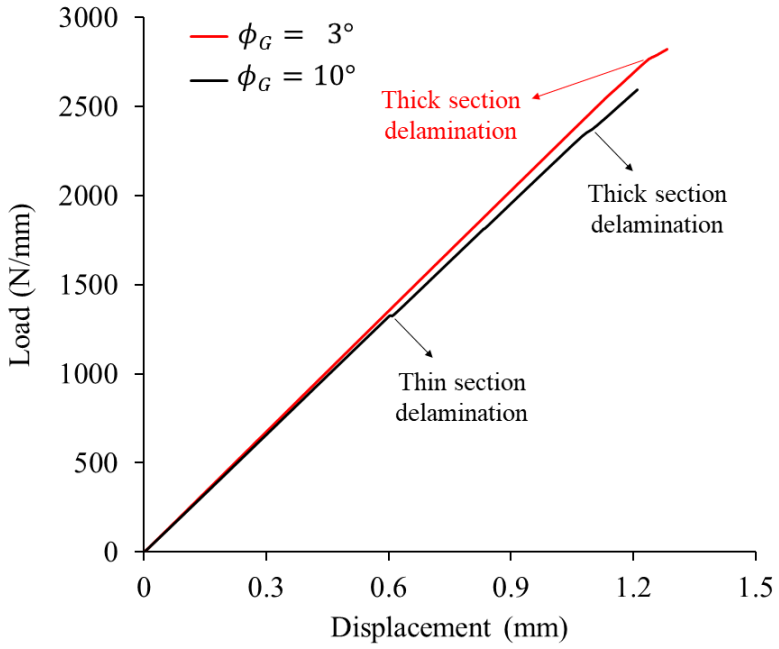

Figure 4.4. Comparison of the load-displacement responses obtained from finite element models for six-stage ply drop-off configuration having constant taper angle designs with $\phi_G = 3°$ and $\phi_G = 10°$.

In order to investigate how the delamination onset loads in the thin and thick sections of the laminate change with respect to the taper angle when multiple plies are dropped in constant taper angle design, a parametric taper angle study is conducted such that the global taper angle varies between $3° - 10°$. Onset loads of the first delamination with respect to the taper angle and their locations are shown in Figure 4.5. Similar to the parametric taper angle study for single-stage ply drop-off performed in Chapter 3, thick section delamination is observed at low taper angles and the delamination onset load does not change when the delamination initiates in the thick section first. However, after the global taper angle is increased above a certain value, the thin section delamination becomes the dominant failure mode in the laminate, and load carrying capacity of the laminate decreases significantly even with a small increase in the taper angle. In fact, when the global taper angle is 10°, almost 50% of the load-carrying capacity of the laminate without any delamination is lost compared to the configuration with 4° global taper angle. Hence, it is concluded that it is important to find a technique to suppress delamination in

laminates with high taper angles in which the thin section delamination mode occurs first.

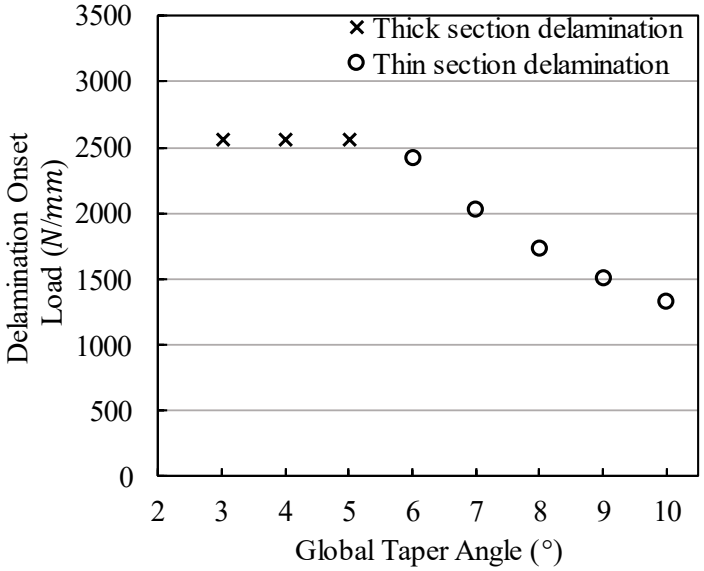

Figure 4.5. Delamination onset loads and location with respect to the global taper angle for the laminate with six ply drop-offs with constant taper angle.

4.4.2 Variable Taper Angle Design

In this section variable taper angle design concept is investigated with different values of taper angle increments, $\Delta\phi$, between the consecutive ply drop-offs, and results are compared with the constant taper angle design. To investigate the relative improvement of the delamination onset load in variable taper angle design concept with respect to constant taper angle design, normalized delamination onset load coefficient is introduced and given in Equation (4.2).

$$f_{onset} = \frac{F_{variable}}{F_{constant}} \tag{4.2}$$

In Equation (4.2), $F_{constant}$ is the delamination onset load in constant taper angle design, and $F_{variable}$ is the delamination onset load in variable taper angle design concept for the same global taper angle with the constant taper angle design. The

normalized delamination onset load with respect to the taper angle increment for a global taper angle of 10° is shown in Figure 4.6. $\Delta\phi = 0$ means that all the taper angles in the laminate are the same; therefore, it is the constant taper angle design, and as $\Delta\phi$ is increased, the taper geometry becomes nonlinear, and the curvature of the taper region increases. The delamination onset loads are normalized with respect to the delamination onset load in the constant taper angle design for the same global taper angle.

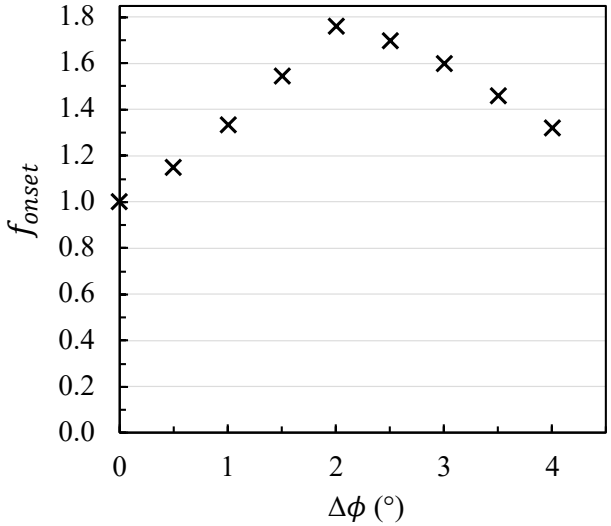

Figure 4.6. Normalized delamination onset load, f_{onset}, versus the taper angle increment, $\Delta\phi$, when $\phi_G = 10°$.

Results in Figure 4.6 reveal an important advantage of the variable taper angle design. As the difference between the consecutive taper angles increases, the delamination onset load increases significantly compared to the constant taper angle design for the same ϕ_G. In fact, almost 80% improvement in the delamination onset load is achieved when $\Delta\phi = 2°$, which is a promising result to suppress delamination in highly tapered laminates. As $\Delta\phi$ is increased further, the delamination onset load starts to decrease indicating the existence of an optimum taper geometry, which maximizes the delamination onset load in the thin section of the laminate for a given configuration studied.

The reason why gradually increasing the taper angle from the thin section to the thick section increases the delamination onset load can be inferred by examining the interlaminar stresses at delamination initiation locations. For this, quadratic damage initiation index, defined in Equation (4.3) is calculated by extracting interlaminar stresses from the critical cohesive elements at each ply drop-off for constant and varying taper angle designs. Ply drop-off IDs and the location of the critical cohesive elements that experience the maximum tractions at the interface where the thin section delamination initiates are shown in Figure 4.7(a), a comparison of the damage initiation index for constant and varying taper angle designs is given in Figure 4.7(b).

$$damage\ initation\ index = \left\{\frac{\langle t_n \rangle}{t_n^0}\right\}^2 + \left\{\frac{t_s}{t_s^0}\right\}^2 \tag{4.3}$$

It should be noted that damage indexes are extracted at the same loading condition before the damage occurs in the constant taper angle design. Damage initiation index distribution for the constant taper angle design shows that there is a considerable stress concentration at the ply drop-off regions near the thinnest section of the laminate, whereas critical cohesive elements near the thicker side of the tapered region do not experience significant interlaminar stresses. However, when we look at the damage index distribution for variable taper angle design with $\Delta\phi = 2°$, which is the optimum variable taper angle configuration for the tapered laminate with six ply drop-off regions examined in this study, stress concentrations at the first and second ply drop-offs near the thinner side of the tapered region are reduced significantly. Compared to the constant taper angle design, an increase in the damage index of the critical cohesive elements near the thicker side of the tapered region is observed. This is a clear indication that varying the taper angles reduces the maximum stress concentration and provides a more uniform distribution of interlaminar stresses among the ply drop-offs. Hence, the variable taper angle design concept can suppress the delamination initiating at the thin section of the highly tapered laminates. Moreover, it is possible to observe an extended fatigue life of the

tapered composite parts by providing a smooth transition from the thin section to the thick section of the highly tapered laminates with variable taper angle design concept due to reduced stress concentrations in critical regions.

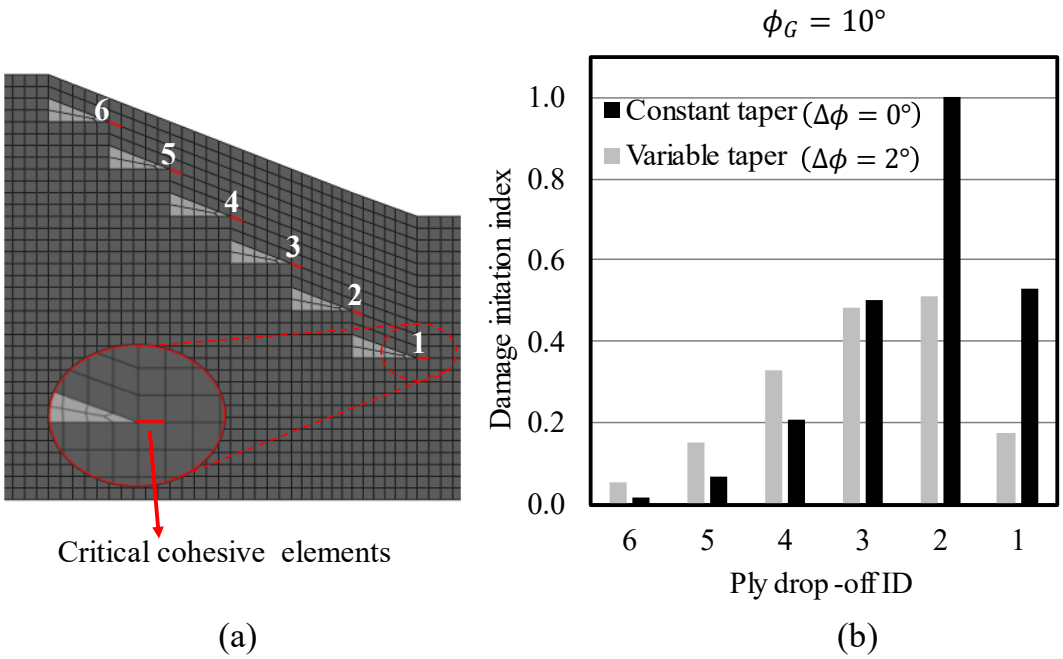

Figure 4.7. (a) Drop off ID numbers and critical cohesive elements which experience maximum interlaminar stresses before the damage initiates, (b) damage initiation index at each critical cohesive elements for constant ($\Delta\phi = 0°$) and variable ($\Delta\phi = 2°$) taper angle design with $\phi_G = 10°$.

It should be noted that although the variable taper angle concept is very effective in suppressing delamination in the thin section, for laminates with lower global taper angles, for which predominantly thick section delamination occurs, improvement in the delamination onset loads is less compared to the thin section delamination. To demonstrate this, the variable taper angle design concept is applied to the six-stage ply drop-off configuration with a global taper angle $\phi_G = 7°$ which is very close to the delamination mode transition angle for the constant taper angle case given in Figure 4.5. Normalized first delamination onset load with respect to the taper angle increment is given in Figure 4.8. which shows that an initial increment in the taper angle difference improves the load-carrying capacity of the laminate up to some point where thin section delamination is suppressed and thick section delamination becomes the first observed delamination mode. Further increment in the taper angle

increment does not increase the delamination onset load in the laminate because the variable taper angle design concept is considerably more effective in reducing the stress concentrations at the thin section which is responsible for the thin section delamination. For the tapered laminate with six ply drop-off regions and a global taper angle $\phi_G = 7°$, in Figure 4.8, we observe a maximum 25% increase in the delamination onset load for the taper angle increment $\Delta\phi = 1°$.

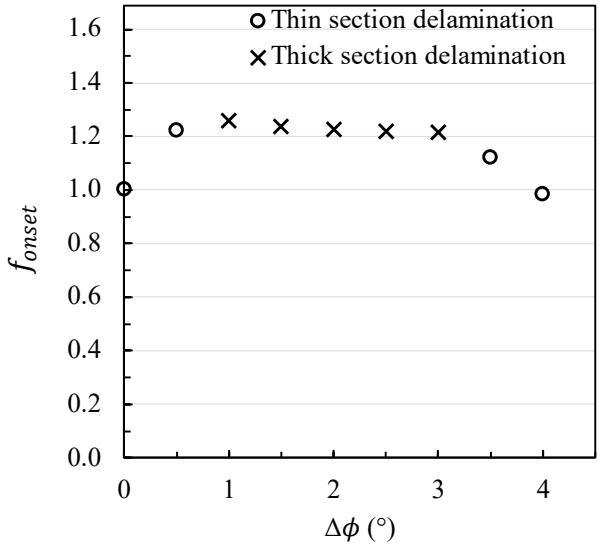

Figure 4.8. Normalized delamination onset load, f_{onset}, and location with respect to the taper angle increment, $\Delta\phi$, for $\phi_G = 7°$.

The present study shows that the variable taper angle design concept is very effective in suppressing delamination in highly tapered laminates where thin section delamination mode is the first delamination mode and when there is a notable margin between thin section delamination onset load and thick section delamination onset load.

4.5 Chapter Conclusion

In this chapter, the variable taper angle design concept is proposed in order to suppress the thin section delamination in highly tapered laminates. To reduce the number of design options, variable taper angles are defined using a taper angle increment parameter. This parameter represents the angular difference between consecutive taper angles and defines the taper curvature. The incorporation of a taper angle increment allows for the examination of the variable taper angle concept using a singular parameter.

For a certain taper geometry with variable taper angle design concept, a notable improvement of nearly 80% in the delamination onset load is observed in comparison to the conventional constant taper angle design, particularly when the global taper angle of the laminate is significantly high. Comparing the interlaminar damage distribution in front of each resin pocket, it is evident that the variable taper angle design effectively diminishes peak interlaminar stresses and achieves a more uniform stress distribution among the ply drop-off regions when compared with the conventional constant taper angle design concept.

In the study performed with a laminate with a moderate taper angle, the application of variable taper angle design increased the delamination onset load of the laminate until the thin section delamination is effectively suppressed, resulting in the transition of the first failure mode to thick section delamination. Further increasing the taper curvature did not improve the delamination onset load in the laminate because the variable taper angle design concept is only effective in reducing the stress concentration at the beginning of the thin section of the laminate. Hence, the application of the variable taper angle design concept is recommended when the initial observation of delamination in the laminate occurs in the thin section, coupled with a significant margin between the onset loads of thin section and thick section delamination.

CHAPTER 5

CONCLUDING REMARKS

5.1 Summary of the Study

The main motivation of the study is to identify the failure mechanisms in laminates with a ply drop-off and developed a numerical model to predict delamination onset in tapered laminates. The models that have been developed are employed to investigate the delamination suppression technique in highly tapered laminates. In Chapter 2, experimental investigations are conducted to examine the failure mechanism in specimens with dropped plies. Additionally, material characterization tests are performed for both glass fiber composite material and pure resin. Chapter 3 is dedicated to the development of essential numerical tools for predicting the onset load and location of delamination in dropped ply specimens. The chapter also includes an investigation of the effects of various parameters on the initiation of delamination. In Chapter 4, based on the knowledge obtained in previous sections, a delamination suppression technique for highly tapered laminates is proposed. The subsequent paragraphs include a detailed summary of the chapters of the study.

In Chapter 2, composite material and pure resin characterization tests are performed in order to provide the necessary material properties to the finite element models. Pure resin tension and fracture toughness specimens are manufactured with the resin casting method, and a technique to create the desired natural crack length in single-edge notch beam specimens is proposed. Standard tension, ILSS, ENF, and DCB tests are performed to obtain the mechanical properties of the composite material. Dropped ply specimens are tested under tensile loading, and thin-section and thick-

section delamination onset sequences and corresponding load levels are captured successfully by using a high-speed camera.

In Chapter 3, finite element models of single-stage ply drop-off regions are created, and enhancement of the interface properties due to the presence of through-thickness compression is taken into account with the USDFLD subroutine. Finite element results for the single-stage dropped ply model are compared with the experimental results, and a good agreement between the numerical and experimental results is obtained. Effects of element size, taper angle, through-thickness compression enhancement, fracture toughness around the resin pocket, and voids in the resin pockets on delamination onset loads and location are investigated with numerical models.

In Chapter 4, an alternative delamination suppression technique for highly tapered laminates is proposed. Consecutive taper angles in multi-stage ply drop-off configuration are defined with a single taper angle increment parameter to reduce the number of design options significantly. Reducing the stress concentrations in the highly tapered laminates to suppress delamination is intended with the proposed design by increasing the taper angles gradually from the thin section towards the thick section. The advantages and limitations of the concept are demonstrated via a series of finite element models.

5.2 Conclusion of the Study

- The proposed method to create controlled pre-cracking for SENB specimens showed promising results in creating the desired crack length without compromising a substantial number of specimens during the preparation phase.

- The experiments with tapered specimens revealed the different characteristics of the thin section and thick section delaminations. Notably, thin section cracks exhibited slow propagation without causing significant softening in the load-displacement response. In contrast, thick section delamination showed abrupt propagation, leading to a noteworthy loss of stiffness in the investigated specimens within the scope of this study.

- Verification studies with the USDFLD subroutine proved that enhancement of the interlaminar shear strength and mode II fracture toughness due to the presence of compression can be considered by utilizing built-in cohesive elements together with a simple subroutine (USDFLD) rather than developing custom cohesive elements from a scratch. However, it is important to define contact clearance in the contact algorithm to ensure accurate measurement of the compressive stresses on the cohesive elements for correct enhancement calculation.

- It is concluded that due to the presence of a compressive stress field together with the shear stresses at the end of the dropped plies, enhancement of the interface properties must be considered in order to accurately predict the delamination initiation load at the thick section of the laminate.

- The study with different finite modeling techniques of the resin pocket showed that while the thick section delamination onset load remained

independent of the fracture toughness values used around the resin pocket or voids, the thin section delamination prediction load decreased significantly. It is concluded that the accurate prediction of thin section delamination onset load is notably sensitive to the fracture toughness values applied around the ply drop-off region and the specific modeling choice regarding the representation of the resin pocket, whether as a void or not.

- The outcomes of a parametric taper angle study and analysis of interlaminar stress distributions reveal a noteworthy trend: as the taper angle increases, the initiation location of delamination shifts from the thick section to the thin section. Additionally, there is a substantial decrease in the delamination onset load. This underlines the sensitivity of the delamination onset load in highly tapered laminates to taper geometry, particularly when the delamination initiates in the thin section.

- The proposed variable taper angle design for highly tapered in Chapter 4 demonstrated that with the proper selection of the taper geometry, thin section delamination can be suppressed in highly tapered laminates. Indeed, this study illustrates a remarkable improvement, with nearly an 80% increase in the delamination onset load observed for a specific highly tapered laminate configuration. Nevertheless, it is important to note that when the global taper angle of the laminate is low, the improvement of the delamination onset load may not be as substantial as observed in highly tapered laminates.

5.3 Future Work

This study investigates the composite material and tapered laminates from manufacturing, testing, numerical modeling, and design perspectives. Therefore, there are multiple topics that can be suggested for future study.

- The pre-cracking method proposed in Chapter 2 for SENB specimens requires a more quantitative approach to apply transverse compressive load for the repeatability of the method. The reason why transverse compression prevents crack propagation also requires detailed investigations.

- The numerical models developed in Chapter 3 are only capable of predicting the delamination onset load and location in tapered laminates. However, to predict the ultimate strength of the laminate, the development of a numerical model taking the fiber fracture into account in tapered laminates is necessary.

- The variable taper angle design concept proposed in Chapter 4 is investigated by using finite element models. However, it is necessary to investigate the manufacturability of the design and perform experimental validation tests to be able to use the proposed design in real-world structures.

REFERENCES

[1] Fishs JC, Lee SW. Delamination of Tapered Composite Structures. Engineering Fracture Mechanics 1989;34:43–54. https://doi.org/10.1016/0013-7944(89)90241-5.

[2] Zhang B, Kawashita LF, Jones MI, Lander JK, Hallett SR. An experimental and numerical investigation into damage mechanisms in tapered laminates under tensile loading. Composites Part A: Applied Science and Manufacturing 2020;133:105862. https://doi.org/10.1016/j.compositesa.2020.105862.

[3] Wisnom MR, Dixon R, Hill G. Delamination in asymmetrically tapered composites loaded in tension. Composite Structures 1996;35:309–22. https://doi.org/10.1016/0263-8223(96)00044-X.

[4] Anderson TL. Fracture Mechanics: Fundamentals and Applications, Third Edition. CRC Press; 2005.

[5] Wisnom M. Delamination in tapered unidirectional glass fibre-epoxy under static tension loading. 32nd Structures, Structural Dynamics, and Materials Conference, Baltimore,MD,U.S.A.: American Institute of Aeronautics and Astronautics; 1991. https://doi.org/10.2514/6.1991-1142.

[6] Mukherjee A, Varughese B. Design guidelines for ply drop-off in laminated composite structures. Composites Part B: Engineering 2001;32:153–64. https://doi.org/10.1016/S1359-8368(00)00038-X.

[7] James M. Curry ERJ, James H. Starnes Jr. Effect of Dropped Plies on the Strength of Graphite-Epoxy Laminates. AIAA JOURNALS 1992;55:158–61. https://doi.org/10.1080/00357529.1980.11764651.

[8] Petrossian Z, Wisnom MR. Parametric study of delamination in composites with discontinuous plies using an analytical solution based on fracture mechanics. Composites Part A: Applied Science and Manufacturing 1998;29:403–14. https://doi.org/10.1016/S1359-835X(97)00102-4.

[9] Shim D-J, Lagace PA. Mechanisms and Structural Parameters Affecting the Interlaminar Stress Field in Laminates with Ply Drop-offs. Journal of Composite Materials 2006;40:345–69. https://doi.org/10.1177/0021998305055192.

[10] Cui W, Wisnom MR, Jones M. Effect of step spacing on delamination of tapered laminates. Composites Science and Technology 1994;52:39–46. https://doi.org/10.1016/0266-3538(94)90006-X.

[11] Gan KW, Allegri G, Hallett SR. A simplified layered beam approach for predicting ply drop delamination in thick composite laminates. Materials & Design 2016;108:570–80. https://doi.org/10.1016/j.matdes.2016.06.105.

[12] Rhee SY, Cho M, Kim HS. Layup optimization with GA for tapered laminates with internal plydrops. International Journal of Solids and Structures 2006;43:4757–76. https://doi.org/10.1016/j.ijsolstr.2005.07.015.

[13] Irisarri F-X, Lasseigne A, Leroy F-H, Le Riche R. Optimal design of laminated composite structures with ply drops using stacking sequence tables. Composite

Structures 2014;107:559–69. https://doi.org/10.1016/j.compstruct.2013.08.030.
[14] Celik O, Parnas L. Maximization of Ultimate Strength of Unidirectional Tapered Composite Structures Considering Different Failure Modes. 58th AIAA/ASCE/AHS/ASC Structures, Structural Dynamics, and Materials Conference, Grapevine, Texas: American Institute of Aeronautics and Astronautics; 2017. https://doi.org/10.2514/6.2017-0893.
[15] Llanos AS, Vizzini AJ. The Effect of Film Adhesive on the Delamination Strength of Tapered Composites. Journal of Composite Materials 1992;26:1968–83. https://doi.org/10.1177/002199839202601306.
[16] Worboys RC. Suppressing Delamination Through Vertically Aligned Carbon Nanotube (VACNT) Interleaves n.d.
[17] Gouldstone C, Degtiarov D, Williams RD. Reinforcing Ply Drop Interfaces Using Vertically-Aligned Carbon Nanotube Forests n.d.
[18] Helmy S, Hoa SV. Tensile fatigue behavior of tapered glass fiber reinforced epoxy composites containing nanoclay. Composites Science and Technology 2014;102:10–9. https://doi.org/10.1016/j.compscitech.2014.05.038.
[19] Minakuchi S, Takeda N. Ply Curving Termination to Suppress Delamination in Composite Ply Drop-Off. In: Niepokolczycki A, Komorowski J, editors. ICAF 2019 – Structural Integrity in the Age of Additive Manufacturing, Cham: Springer International Publishing; 2020, p. 124–32. https://doi.org/10.1007/978-3-030-21503-3_10.
[20] Salpekar SA, Raju IS, O'Brien TK. Strain-Energy-Release Rate Analysis of Delamination in a Tapered Laminate Subjected to Tension Load. Journal of Composite Materials 1991;25.
[21] Gordon T, Xu X, Wisnom MR, Kim BC. Novel tape termination method for automated fibre placement: Cutting characteristics and delamination suppression. Composites Part A: Applied Science and Manufacturing 2020;137:106023. https://doi.org/10.1016/j.compositesa.2020.106023.
[22] Gordon T, Xu X, Kawashita L, Wisnom MR, Hallett SR, Kim BC. Delamination suppression in tapered unidirectional laminates with multiple ply drops using a tape scarfing technique. Composites Part A: Applied Science and Manufacturing 2021;150:106627. https://doi.org/10.1016/j.compositesa.2021.106627.
[23] Armanios E, Parnas L. Delamination Analysis of Tapered Laminated Composites Under Tensile Loading. In: O'Brien T, editor. Composite Materials: Fatigue and Fracture (Third Volume), 100 Barr Harbor Drive, PO Box C700, West Conshohocken, PA 19428-2959: ASTM International; 1991, p. 340-340–19. https://doi.org/10.1520/STP17726S.
[24] Vizzini AJ. Shear-Lag Analysis about an Internally-Dropped Ply. Journal of Reinforced Plastics and Composites 1997;16:73–85. https://doi.org/10.1177/073168449701600106.
[25] He K, Ganesan R, Hoa SV. Modified shear-lag model for analysis of a composite laminate with drop-off plies. Composites Science and Technology 2003;63:1453–62. https://doi.org/10.1016/S0266-3538(03)00166-0.

[26] Tsai SW, Wu EM. A General Theory of Strength for Anisotropic Materials. Journal of Composite Materials 1971;5:58–80. https://doi.org/10.1177/002199837100500106.
[27] Hashin Z. Failure Criteria for Unidirectional Fiber Composites. Journal of Applied Mechanics 1980;47:329–34. https://doi.org/10.1115/1.3153664.
[28] Allegri G, Wisnom MR, Hallett SR. A simplified approach to the damage tolerance design of asymmetric tapered laminates. Part I: Methodology development. Composites Part A: Applied Science and Manufacturing 2010;41:1388–94. https://doi.org/10.1016/j.compositesa.2010.05.009.
[29] Allegri G, Wisnom MR, Hallett SR. A simplified approach to the damage tolerance design of asymmetric tapered laminates. Part II: Methodology validation. Composites Part A: Applied Science and Manufacturing 2010;41:1395–402. https://doi.org/10.1016/j.compositesa.2010.05.019.
[30] Kawashita LF, Jones M, Giannis S, Hallett SR, Wisnom MR. HIGH FIDELITY MODELLING OF TAPERED LAMINATES WITH INTERNAL PLY TERMINATIONS n.d.
[31] DeTeresa SJ, Freeman DC, Groves SE. The Effects of Through-thickness Compression on the Interlaminar Shear Response of Laminated Fiber Composites. Journal of Composite Materials 2004;38:681–97. https://doi.org/10.1177/0021998304042401.
[32] Cartié D, Davies P, Peleau M, Partridge IK. The influence of hydrostatic pressure on the interlaminar fracture toughness of carbon/epoxy composites. Composites Part B: Engineering 2006;37:292–300. https://doi.org/10.1016/j.compositesb.2005.12.002.
[33] Gan KW, Hallett SR, Wisnom MR. Measurement and modelling of interlaminar shear strength enhancement under moderate through-thickness compression. Composites Part A: Applied Science and Manufacturing 2013;49:18–25. https://doi.org/10.1016/j.compositesa.2013.02.004.
[34] Xu X, Wisnom MR, Sun X, Rev T, Hallett SR. Experimental determination of Through-Thickness Compression (TTC) enhancement factor for Mode II fracture energy. Composites Science and Technology 2018;165:66–73. https://doi.org/10.1016/j.compscitech.2018.06.012.
[35] Catalanotti G, Furtado C, Scalici T, Pitarresi G, Van Der Meer FP, Camanho PP. The effect of through-thickness compressive stress on mode II interlaminar fracture toughness. Composite Structures 2017;182:153–63. https://doi.org/10.1016/j.compstruct.2017.09.014.
[36] Cui W, Wisnom MR, Jones M. New model to predict static strength of tapered laminates. Composites 1995;26:141–6. https://doi.org/10.1016/0010-4361(95)90414-U.
[37] Li X, Hallett SR, Wisnom MR. Predicting the effect of through-thickness compressive stress on delamination using interface elements. Composites Part A: Applied Science and Manufacturing 2008;39:218–30. https://doi.org/10.1016/j.compositesa.2007.11.005.
[38] Zou Z, Lee H. A cohesive zone model taking account of the effect of through-thickness compression. Composites Part A: Applied Science and

Manufacturing 2017;98:90–8. https://doi.org/10.1016/j.compositesa.2017.03.015.
[39] Wang S, Li Z, Yuan R, Li G, Li D. A shear hardening model for cohesive element method and its application in modeling shear hydraulic fractures in fractured reservoirs. Journal of Natural Gas Science and Engineering 2020;83:103580. https://doi.org/10.1016/j.jngse.2020.103580.
[40] Interglass 92145 n.d. https://cristex.co.uk/wp-content/uploads/2022/08/92145-FK144-045.pdf (accessed December 25, 2023).
[41] SikaBiresin® CR80 n.d. https://industry.sika.com/en/home/advanced-resins/sports-and-leisure/composite-resin-systems/composite-systemsforvacuuminfusion/sikabiresin-cr80.html (accessed December 25, 2023).
[42] ODAK Kompozit Teknolojileri A.Ş n.d. https://www.odakkompozit.com.tr/ (accessed December 25, 2023).
[43] User's Manuel: Aramis 2013.
[44] Tamura K, Tamura S, Hashimoto A. Precrack Introducing Method in CT-Specimens for Measuring K Values of Brittle Materials. 15th International Conference on Experimental Mechanics 2012.
[45] Kuppusamy N, Tomlinson RA. Repeatable pre-cracking preparation for fracture testing of polymeric materials. Engineering Fracture Mechanics 2016;152:81–7. https://doi.org/10.1016/j.engfracmech.2015.12.007.
[46] Dashatan SH, Parnas L, Coker D, Bozkurt MO, Ozen EB. In-situ observation and numerical study of dynamic delamination in tapered composite laminates. Composite Structures 2023;312:116841. https://doi.org/10.1016/j.compstruct.2023.116841.
[47] Camanho P. Mixed-Mode Decohesion Finite Elements for the Simulation of Delamination in Composite Materials. Composite Materials 2002.
[48] Brewer JC, Lagace PA. Quadratic Stress Criterion for Initiation of Delamination. Journal of Composite Materials 1988;22:1141–55. https://doi.org/10.1177/002199838802201205.
[49] Benzeggagh ML, Kenane M. Measurement of mixed-mode delamination fracture toughness of unidirectional glass/epoxy composites with mixed-mode bending apparatus. Composites Science and Technology 1996;56:439–49. https://doi.org/10.1016/0266-3538(96)00005-X.
[50] Kuo Y-M, Lin H-J, Wang C-N, Liao C-I. Estimating the Elastic Modulus through the Thickness Direction of a Uni-direction Lamina which Possesses Transverse Isotropic Property. Journal of Reinforced Plastics and Composites 2007;26:1671–9. https://doi.org/10.1177/0731684407081450.
[51] Schellekens JCJ, De Borst R. On the numerical integration of interface elements. Numerical Meth Engineering 1993;36:43–66. https://doi.org/10.1002/nme.1620360104.
[52] Turon A, Dávila CG, Camanho PP, Costa J. An engineering solution for mesh size effects in the simulation of delamination using cohesive zone models. Engineering Fracture Mechanics 2007;74:1665–82. https://doi.org/10.1016/j.engfracmech.2006.08.025.

[53] Turon A, Camanho PP, Costa J, Renart J. Accurate simulation of delamination growth under mixed-mode loading using cohesive elements: Definition of interlaminar strengths and elastic stiffness. Composite Structures 2010;92:1857–64. https://doi.org/10.1016/j.compstruct.2010.01.012.
[54] Harper PW, Hallett SR. Cohesive zone length in numerical simulations of composite delamination. Engineering Fracture Mechanics 2008;75:4774–92. https://doi.org/10.1016/j.engfracmech.2008.06.004.
[55] Yang Q, Cox B. Cohesive models for damage evolution in laminated composites. Int J Fract 2005;133:107–37. https://doi.org/10.1007/s10704-005-4729-6.
[56] Yang QD, Cox BN, Nalla RK, Ritchie RO. Fracture length scales in human cortical bone: The necessity of nonlinear fracture models. Biomaterials 2006;27:2095–113. https://doi.org/10.1016/j.biomaterials.2005.09.040.
[57] König M, Krüger R, Kussmaul K, von Alberti M, Gädke M. Characterizing Static and Fatigue Interlaminar Fracture Behavior of a First Generation Graphite/Epoxy Composite. In: Hooper S, editor. Composite Materials: Testing and Design, Thirteenth Volume, 100 Barr Harbor Drive, PO Box C700, West Conshohocken, PA 19428-2959: ASTM International; 1997, p. 60-60–22. https://doi.org/10.1520/STP18270S.

APPENDICES

A. Material Characterization Test Results for All Specimens

Table A. 1. Test results for 0° tension specimens of Interglass 92145/CR80 glass fiber composite material. Tests are conducted according to ASTM D3039.

Property	Sp. 1	Sp. 2	Sp. 3	Sp. 4	Sp. 5	Average	C.V. (%)
E_1 (GPa)	38.54	37.68	40.19	38.69	39.32	38.88	2.41
v_{12}	0.249	0.266	0.278	0.269	0.266	0.266	3.96
X_T (MPa)	696.4	726	732.4	655.2	743.0	710.6	4.99

Table A. 2. Test results for 90° tension specimens of Interglass 92145/CR80 glass fiber composite material. Tests are conducted according to ASTM D3039.

Property	Sp. 1	Sp. 2	Sp. 3	Sp. 4	Sp. 5	Average	C.V. (%)
E_2 (GPa)	12.77	13.15	13.14	10.28	11.47	12.16	10.34
Y_T (MPa)	43.1	43.7	43.7	46.7	43.9	44.2	3.21

Table A. 3. Test results for $\pm 45°$ tension specimens of Interglass 92145/CR80 glass fiber composite material. Tests are conducted according to DIN EN 6031.

Property	Sp. 1	Sp. 2	Sp. 3	Sp. 4	Sp. 5	Average	C.V. (%)
G_{12} (GPa)	4.42	4.51	4.62	4.74	4.73	4.6	3.02
S_{12} (MPa)	98.7	108.9	105.8	107.4	105.2	105.2	3.71

Table A. 4. Test results for DCB specimens of Interglass 92145/CR80 glass fiber composite material. Tests are conducted according to DIN EN 6033.

Property	DCB 1	DCB 2	DCB 3	DCB 4	DCB 5	Average	C.V. (%)
G_{Ic} (N/mm)	0.789	1.142	0.988	0.829	0.684	0.886	20.28

Table A. 5. Test results for ENF specimens of Interglass 92145/CR80 glass fiber composite material. Tests are conducted according to DIN EN 6034.

Property	ENF 1	ENF 2	ENF 3	ENF 4	ENF 5	Average	C.V. (%)
G_{IIc} (N/mm)	1.219	1.196	1.388	1.213	1.019	1.207	10.82

Table A. 6. Test results for ILSS specimens of Interglass 92145/CR80 glass fiber composite material. Tests are conducted according to ASTM 2344.

Property	ILSS 1	ILSS 2	ILSS 3	ILSS 4	ILSS 5	ILSS 6	Average	C.V. (%)
τ_s^0 (MPa)	46.3	40.8	48.2	45.5	45.4	48.5	45.8	6.09

Table A. 7. Test results for dogbone tension specimens of CR80/CH80-6 resin system. Tests are conducted according to ASTM D638.

Property	Sp. 1	Sp. 2	Sp. 3	Sp. 4	Sp. 5	Sp. 6	Average	C.V. (%)
E_{resin} (GPa)	3.07	3.28	3.28	3.22	3.33	3.16	3.22	3.03
v_{resin}	0.376	0.389	0.399	0.376	0.402	0.368	0.385	3.56
$(\tau_s^0)_{resin}$ (MPa)	77.8	79.1	74.4	77.7	78.6	79.1	77.8	2.29

Table A. 8. Test results for SENB specimens of CR80/CH80-6 resin system. Tests are conducted according to ASTM D5045.

Property	SENB 1	SENB 2	SENB 3	SENB 4	SENB 5	Average	C.V. (%)
$(G_c)_{resin}$ (N/mm)	0.119	0.111	0.169	0.147	0.106	0.131	20.62